Nonlinear Absorption of Pump in Semiconductor and Organic Terahertz Generator Crystals

Ph.D. Thesis

Author:
Abhishek Gupta

Supervisor:
Dr. József András Fülöp
ELI ALPS Research Institute, Szeged, Hungary

Doctoral School of Physics
Institute of Physics
University of Szeged
Faculty of Natural Sciences
2026
Szeged

This thesis is dedicated to my parents, my wife Monika, and my daughter Anaisha.

Contents

Abbreviations

2PA two-photon absorption

3PA three-photon absorption

BNA N-benzyl-2-methyl-4-nitroaniline

CG contact-grating

cLN congruent lithium niobate ($LiNbO_3$)

CT cryogenic temperature

CW continuous-wave

DFG difference-frequency generation

EOS electro-optic sampling

FCA free-carrier absorption

FL Fourier limit, Fourier limited

FWHM full width at half maximum

GVD group velocity dispersion

LN lithium niobate ($LiNbO_3$)

MNA 2-methyl-4-nitroaniline

NMBA 4-nitro-4'-methylbenzylidene aniline

OPA optical parametric amplification

OPCPA optical parametric chirped-pulse amplification

OR optical rectification

PCA photoconductive antenna

PFT pulse-front tilt

RT room temperature

SFG sum-frequency generation

SHG second-harmonic generation

sLN stoichiometric lithium niobate ($LiNbO_3$)

THz terahertz

TPFP tilted-pulse-front pumping

Chapter 1

Introduction

Terahertz (THz) radiation refers to a specific range of electromagnetic radiation located between microwaves and infrared radiation. The first THz measurements were related to thermal radiation in the 1890s which played an important role in the discovery of quantum theory. These pioneering experiments were primarily performed by Heinrich Rubens and F. Kurlbaum [1]. As Max Plank expressed: "Without Rubens's work, the quantum theory would have taken longer to develop and it may not even have been found by German scientists at all" [2]. Inspite of the fact that there has been scientific interest (for example in spectroscopy [3–5], imaging [6, 7], astrophysics [8, 9] etc.) in this frequency range since the early 1920s, this term is relatively new and encompasses the high-frequency portions of the microwave and far-infrared radiation ranges [10]. Its frequency ranges from 0.1 to 10 THz (or wavelengths from 3 mm to 30 μm). Specifically, a frequency of 1 THz corresponds to a wavelength of 300 μm, a wavenumber of 33.3 cm^{-1}, and a photon energy of 4.14 meV [11]. THz radiation is often referred to as the 'sub-millimeter wave' or 'far infrared' region of the electromagnetic spectrum as illustrated in Figure 1.1.

For an extended period, the THz band remained largely unexamined due to the absence of effective sources and detectors [13, 14]. As a result, this spectral range was commonly referred

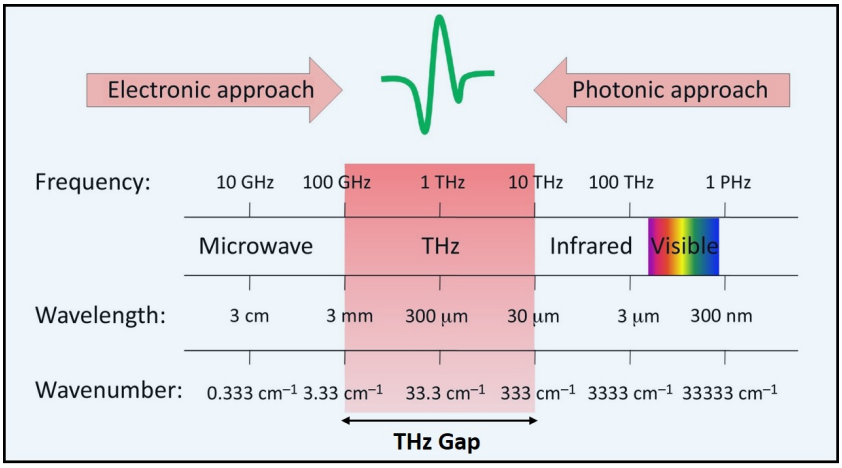

Figure 1.1: THz band in the electromagnetic spectrum [12].

to as the THz gap, reflecting the historical challenges of generating and detecting this type of radiation. Since the 1970s, improvements in electronics and photonics have introduced new materials and devices that have started to close this gap, leading to significant advancements in both fundamental research and practical applications. THz radiation has become increasingly accessible over the past few decades, enabling extensive research and applications across industry, security, medicine, and materials science. Many non-metallic materials, including paper, plastics, fabrics, ceramics, and organic compounds are transparent to THz radiation, enabling noninvasive imaging for inspection and quality control. [15–19]. It is used to detect contaminants in food, including glass, metal, and organic matter [17, 20, 21], to identify hidden materials through spectral fingerprints [22], and to locate concealed weapons or explosives in security screening [23]. In medicine, its nonionizing nature enables safe imaging of skin cancers and tissue hydration [24–26]. High-energy THz pulses have been applied in tomography and proposed for hadron therapy [27–29]. THz radiation also supports studies of molecular alignment [30], ultrafast carrier dynamics [31, 32], nonlinear processes [33], and semiconductor responses [34–36] while powerful THz fields enable particle acceleration, bunch compression, and charged-particle control in strong-field physics [37–43].

THz science depends on advances in source technology, motivating the development of accessible emitters with precise control. Continuous-wave (CW) systems [44–46] provide narrowband output for high resolution spectroscopy [47], telecommunications [48], and non-destructive testing [49]. Pulsed systems use picosecond or femtosecond lasers to generate broadband radiation for spectroscopy [3, 50] and ultrafast studies. The emergence of femtosecond lasers has greatly expanded THz generation and detection capabilities. The maximum documented THz pulse energy in a photoconductive antenna (PCA) is 8.3 μJ, with a peak electric field of 331 kV/cm and optical-to-THz conversion efficiency of 0.15%, produced by interdigitated ZnSe with a 12.2 cm^2 aperture, excited by a 400 nm pump laser delivering multi-mJ energies at a 10 Hz repetition rate [51]. But they have a technical limitation due to large capacitance, which limits the peak THz field by distorting the high-voltage bias pulse and promoting early air breakdown. The laser-driven plasma method, conversely, permits the application of high intensities for terahertz geneartion, leading to the creation of ultrabroadband THz pulses with energy levels reaching up to multi-μJ (0.1-80 μJ) [52] in the range of 1-100 THz [53] reaching field strengths >8 MV/cm [54]. Nonetheless, the conversion efficiency for terahertz generation from this method remains quite low (0.01%) at shorter wavelengths [55], unless longer wavelengths are used [52] where it goes up to 2.6%. But increasing to higher THz energies is challenging because of plasma instabilities [56, 57]. Furthermore, THz sources that utilize electron accelerators produce THz pulses in the μJ to mJ range with high field strengths exceeding 100 MV/cm [58], but this source is constrained by the inaccessibility of large-scale facilities.

Up to now, the combination of optical rectification (OR) and tilted-pulse-front (TPF) technique in nonlinear crystal like lithium niobate (LN) has yielded a THz pulse energy of 13.9 mJ [59], a peak electric field reaching 7.5 MV/cm^{-1} [59], and a reported conversion efficiency of 1.3% [60]. However, in addition to restricted bandwidth (up to 3 THz), due to material absorption, phase-matching constraints, and pump-laser properties [61, 62], this technique has limitations due to the large ($\sim 63°$) pulse-front tilt angle [61, 63, 64].

Recently, semiconductors, such as ZnTe [65], GaP [66], GaAs [67], and GaSe [68], have emerged as promising alternative sources of intense THz fields. In semiconductors, low-order multiphoton pump absorption increases free-carrier absorption in the THz range and limits the THz generation efficiency. A sufficiently long pump wavelength, combined with the tilted-pulse-front technique, can eliminate this effect. The required pulse-front tilt angles are relatively small, typically below 30° [65]. A contact-grating (CG) THz source demonstrated the advantage of this approach, with a monolithic collinear geometry and a high conversion efficiency in ZnTe [69]. The development of powerful mid infrared (MIR) femtosecond sources based on optical parametric chirped pulse amplification (OPCPA) [70–72] has further expanded the potential of semiconductor THz sources. They are ideally suited as efficient drivers of semiconductor CG THz sources, which are free from detrimental low order multiphoton pump absorption. *The development of intense pulsed THz source using semiconductor is one of the main subject of the present work. The aim was to demonstrate a compact source of intense THz pulses pumped at a mid-infrared wavelength of about 4 μm and to investigate some of the effects limiting THz generation. Novel THz source based on GaP CG semiconductor was investigated both by experimental studies and numerical simulations*.

Organic, nonlinear optical crystals, are another very attractive THz sources for the efficient generation of strong-field THz pulses by optical rectification of femtosecond laser pulses [73, 74]. They have exceptionally large second-order nonlinear optical coefficients, broad bandwidth (>5 THz) [75], and can reach high THz-generation efficiency in a collinear scheme. A high energy of 0.9 mJ [76], a high electric field of 8.3 MV/cm [77] and an average power of 68 mW and a record THz conversion efficiency of 6% [78] has been reported using these crystals. Typically, pump wavelengths longer than 1.2 μm are required, but in organic crystals like BNA, NMBA, and MNA, Ti:sapphire or Yb lasers can pump THz generation directly, without conversion to longer wavelengths. However, linear and multiphoton absorption of the pump laser, can increase the crystal temperature above the melting point [79, 80], or cause other degradation making them susceptible to optical damage. Bonding the crystal to a substrate with high thermal conductivity, such as sapphire, increases the damage threshold [79]. Besides heating, multiphoton absorption can produce free carriers, which absorb the generated THz radiation, thereby reducing the efficiency of THz generation [79]. The nonlinear transmission in a BNA crystal [79] was measured, though, without giving values for multiphoton absorption coefficients. *Another aim of this work was to determine the values of multiphoton absorption coefficients for the organic THz generator crystals BNA, NMBA, and MNA which can help designing efficient and robust THz sources with organic crystals*.

This dissertation is structured as follows. Chapter 2 discusses the theory and background of THz generation based on nonlinear optical processes, THz sources based on optical rectification, and THz pulse characterization. It also gives a brief introduction to nonlinear absorption and application of intense THz pulses. Chapter 3 sets the scientific goals. Chapter 4 discuss the results of the work in two topics. First, the expected performance of contact grating based semiconductor THz source was investigated by experiments and simulation. Second, experimental demonstration of nonlinear absorption and its saturation in organic THz sources, and quantification of two-photon coefficient through numerical modeling. Chapter 5 gives the thesis points.

Chapter 2

Background

2.1 Nonlinear optical processes

In most instances of light-matter interactions, the primary engagement takes place between electromagnetic waves and electrons. The electromagnetic waves compel electrons to move, and this accelerated electron motion generates electromagnetic radiation. During these induced movements, the distribution of electrons shifts, leading to charge separation within the atoms and molecules, resulting in the polarization of the material. An adequately strong optical field can alter the optical characteristics of a material system [81]. In such instances, the way a material system responds to the applied optical field is influenced in a nonlinear fashion by the intensity of the optical field [82]. The identification of second-harmonic generation (SHG) by Franken and colleagues in 1961, shortly after the introduction of the first operational laser, signified the advent of nonlinear optics [83]. Generally, only laser light possesses the required intensity to considerably change the optical properties of materials. At low intensities, the relationship between the induced polarization $\mathbf{P}(\mathbf{E})$ in a material is directly proportional to the strength of the driving electric field $\mathbf{E}$ and can be expressed as:

$$\mathbf{P}(\mathbf{E}) = \epsilon_0 \chi^{(1)} \mathbf{E} = \mathbf{P^{(1)}}. \tag{2.1}$$

where ϵ_0 is the permittivity of free space and $\chi^{(1)}$ is the linear susceptibility (second-rank tensor and it can be frequency dependent). For higher field strengths, the material response to the applied field may become nonlinear, Equation 2.1 can be described by a Taylor-series expansion:

$$\begin{aligned} \mathbf{P}(\mathbf{E}) &= \varepsilon_0 \left(\chi^{(1)}\mathbf{E} + \chi^{(2)}\mathbf{E}\mathbf{E} + \chi^{(3)}\mathbf{E}\mathbf{E}\mathbf{E} + \ldots \right) \\ &= \mathbf{P}^{(1)} + \mathbf{P}^{(2)} + \mathbf{P}^{(3)} + \ldots \\ &= \mathbf{P}^{(1)} + \mathbf{P}^{\mathrm{NL}}. \end{aligned} \tag{2.2}$$

where $\chi^{(n)}$ and $\mathbf{P}^{\mathrm{NL}}$ are the n^{th}-order nonlinear susceptibility and nonlinear polarization respectively for n>1. In condensed matter physics, the typical value for linear susceptibility $\chi^{(1)}$ is around one, while the nonlinear susceptibilities of second order $\chi^{(2)}$ and third order $\chi^{(3)}$

are approximately $\sim 10^{-12}$ m/V and $\sim 10^{-24}$ m^2/V^2, respectively [82]. Equation 2.2 indicates that the linear term dominates at low field strengths; however, as the field strength increases, the higher-order terms become significant and give rise to various nonlinear phenomena. The wave equation governing electromagnetic radiation propagation in the nonlinear optical medium is of the form:

$$\nabla^2 E - \frac{n}{c^2}\frac{\partial^2 E}{\partial t^2} = \frac{1}{c^2\epsilon_0}\frac{\partial^2 P^{\mathrm{NL}}}{\partial t^2}, \tag{2.3}$$

where n is the linear refractive index of the material.

2.1.1 Second-order nonlinear processes

During propagation of a light beam in a material with nonlinear response, new frequency components can be generated which were not contained in the input [82]. Let us consider a nonlinear material with second-order nonlinear susceptibility $\chi^{(2)}$ and an optical field $E(t)$ consisting of two oscillating frequencies, ω_1 and ω_2 is incident on a nonlinear material. This optical field can be expressed as:

$$E(t) = \frac{1}{2}E_1 e^{i\omega_1 t} + \frac{1}{2}E_2 e^{i\omega_2 t} + \text{c.c.} \tag{2.4}$$

The second-order nonlinear response is given as follows:

$$\begin{aligned} P^{(2)}(t) &= \epsilon_0\chi^{(2)}EE \\ &= \frac{1}{4}\epsilon_0\chi^{(2)}[E_1^2 e^{i2\omega_1 t} + E_2^2 e^{i2\omega_2 t} + 2E_1E_2e^{i(\omega_1+\omega_2)t} \\ &+ 2E_1E_2^* e^{i(\omega_1-\omega_2)t} + 2E_1E_1^*] + \text{c.c.} \end{aligned} \tag{2.5}$$

Equation 2.5 consists of several frequency components of the nonlinear polarization, which can be expressed as [82],

$$P^{(2)}(2\omega_1) = \frac{1}{4}\epsilon_0\chi^{(2)}E_1^2 e^{i2\omega_1 t} \qquad (SHG), \tag{2.6}$$

$$P^{(2)}(2\omega_2) = \frac{1}{4}\epsilon_0\chi^{(2)}E_2^2 e^{i2\omega_2 t} \qquad (SHG), \tag{2.7}$$

$$P^{(2)}(\omega_1+\omega_2) = \frac{1}{2}\epsilon_0\chi^{(2)}E_1E_2 e^{i(\omega_1+\omega_2)t} \qquad (SFG), \tag{2.8}$$

$$P^{(2)}(\omega_1-\omega_2) = \frac{1}{2}\epsilon_0\chi^{(2)}E_1E_2^* e^{i(\omega_1-\omega_2)t} \qquad (DFG), \tag{2.9}$$

$$P^{(2)}(0) = \frac{1}{2}\epsilon_0\chi^{(2)}E_1E_1^* \qquad (OR). \tag{2.10}$$

Here E is the spectral amplitude of the electric field of the optical pump pulse at different frequencies, E^* is the complex conjugate of the electric field. Based on Equations 2.6 - 2.10,

the second-order nonlinear polarization exhibits four unique, nonzero frequency components. These components encompass frequency upconversion processes like second harmonic generation (SHG) and sum frequency generation (SFG), as well as frequency downconversion processes such as difference frequency generation (DFG). Additionally, there is optical rectification (OR), which results in a steady state polarization of zero frequency. This can be regarded as a special case of DFG, where the two interacting frequencies are identical [82]. The optical rectification plays a crucial role in generating terahertz pulses in nonlinear media.

2.1.2 Optical rectification

Short electromagnetic pulses have multiple frequency components and optical rectification (OR) can take place between any pair of these components. OR is a second-order nonlinear optical process which, in this case, can be viewed as a specific instance of DFG, where the interaction takes place among the frequency components within the short pulse bandwidth of a spectrally broad electromagnetic pulse [82]. DFG can create a new spectral component with the angular frequency Ω by combining spectral components from the optical pulse with angular frequencies ω and $\omega + \Omega$. In contrast to inter-pulse DFG with two input pulses (which may have different carrier frequencies), OR can therefore be characterized as intra-pulse DFG. It results in the production of a DC or low frequency polarization. Optical rectification (OR) was employed to produce electromagnetic (microwave) pulses from picosecond laser pulses. In fact, in 1962, [84] showcased the first DC optical rectification using 694 nm continuous wave (CW) in potassium dihydrogen phosphate and potassium deuterium phosphate. OR like any other second-order nonlinear optical process can only occur in noncentrosymmetric crystals [82, 85].

The second order nonlinear polarization induced by the pump pulse can be calculated as [86]

$$P^{\mathrm{NL}}(\Omega) = \epsilon_0 \chi^{(2)} \int_0^{\infty} E(\omega + \Omega) E^*(\omega) d\omega, \tag{2.11}$$

where ϵ_0 is the vacuum permittivity, ω is the optical frequency, and Ω is the difference frequency.

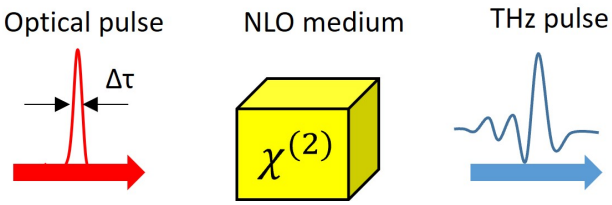

Figure 2.1: Optical rectification process in a nonlinear medium.

The femtosecond pump pulses of pulse width $\Delta\tau$ induces a transient polarization, $P(t)$, in the nonlinear optical (NLO) medium , which in turn emits a THz-bandwidth pulse, as shown in Figure 2.1. The second time derivative of the transient polarization determines the time evolution of the THz pulse. This is expressed as [87];

$$E(t) \propto \frac{\partial^2 P(t)}{\partial t^2}. \tag{2.12}$$

2.1.3 Nonlinear absorption

Nonlinear absorption refers to the physical process where a material's ability to absorb light changes as a function of the incident light's intensity, rather than just material properties, causing transparency to increase (saturable absorption) or decrease (two-photon/multiphoton absorption) at high light levels. Key mechanisms include two-photon absorption (TPA), excited-state absorption (ESA), and free-carrier absorption (FCA), where the absorption coefficient changes with input intensity [88]. It plays a decisive role in limiting THz generation, because the same intense fields required to produce strong THz pulses also drive materials into regimes where their absorption no longer remains linear. At high pump intensities, nonlinear absorption mechanisms such as free carrier absorption, multiphoton absorption, and field induced carrier heating increase the effective loss inside the generation medium. This reduces the fraction of pump energy that can be converted into THz radiation and shortens the interaction length, making it difficult to achieve high THz field strength [89].

A scheme of multiphoton absorption (MPA) processes of various orders is shown in Figure 2.2. Multiphoton absorption (MPA) can promote electrons across the semiconductor bandgap when the combined photon energy exceeds the gap. Once excited to the conduction band, these carriers interact with the incident radiation, giving rise to free-carrier absorption. Because the carrier density depends nonlinearly on the incident intensity and on the order of the MPA process, the resulting free-carrier absorption also grows nonlinearly. As the pump intensity increases, the rapidly rising free-carrier population enhances absorption at THz frequencies, ultimately limiting the pump levels usable for efficient THz generation and lowering conversion efficiency [90].

In semiconductors and plasmas, strong THz fields heat carriers within a single cycle, increasing scattering rates and dynamically modifying conductivity. This enhances intraband absorption and suppresses further THz buildup [91]. These effects also reshape the generated waveform i.e. the leading edge of the THz pulse often experiences stronger absorption than the trailing edge, producing asymmetric temporal profiles and reducing spectral bandwidth [92]. As THz sources push toward higher fields and broader bandwidths, understanding and managing nonlinear absorption becomes essential, not only to maximize conversion efficiency, but also to exploit the rich physics it reveals about ultrafast charge transport and strong field light–matter interaction [89, 91].

2.2 Terahertz generation by optical rectification

Various methods, such as photoconductive antennas, laser-plasma systems, as well as optical rectification and free electron lasers, have been investigated for terahertz radiation generation. Optical rectification is one of the most efficient methods for producing terahertz radiation in nonlinear crystals with femtosecond laser pulses. It enables the generation of terahertz pulses with high field strengths and a wide bandwidth. Optical rectification in nonlinear materials has

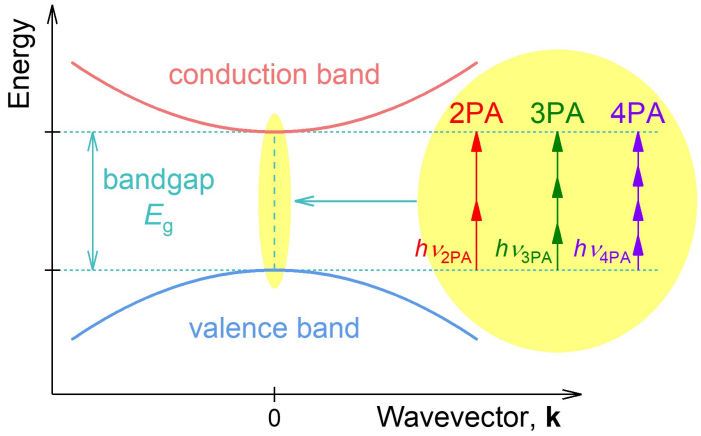

Figure 2.2: Schematic band structure of a direct-bandgap semiconductor (e.g., ZnTe), illustrating free-carrier generation through multiphoton absorption of different orders. 2PA: two-photon absorption, 3PA: three-photon absoprtion, 4PA: four-photon absorption, Adapted from Ref. [65].

led to the creation of innovative THz sources with energy reaching millijoules [37, 87, 93]. Optical rectification in nonlinear materials depends on the effective nonlinear coefficient (d_{eff}) of the nonlinear material [91]. The effective nonlinear coefficient is a parameter that characterizes how efficiently a material supports a nonlinear optical interaction. It reflects the strength of the nonlinear polarization induced by an applied optical field. The expression for the THz generation efficiency by long plane-wave pulses in case of phase matching (see Section 2.2.1 below) [94] can be described by the following equation:

$$\eta(\Omega) = \frac{2\Omega^2 d_{\text{eff}}^2 L^2 I}{\epsilon_0 c^3 n^2(\omega_0) n(\Omega)} \cdot e^{-\frac{1}{2}\alpha(\Omega)L} \cdot \frac{\sinh^2\left[\frac{1}{4}\alpha(\Omega)L\right]}{\left[\frac{1}{4}\alpha(\Omega)L\right]^2}. \tag{2.13}$$

Equation 2.13 is valid in the absence of pump absorption or depletion, and it takes into account THz absorption. Here, L is the material length and I is the pump intensity, ϵ_0 the vacuum permittivity, $n(\omega_0)$ and $n(\Omega)$ are the refractive indices at the optical pump central (carrier) frequency and the generated THz frequencies, $\alpha(\Omega)$ the absorption coefficient for the THz radiation, respectively. Obviously, a large effective nonlinear coefficient, d_{eff}, and a small THz absorption coefficient, $\alpha(\Omega)$, are advantageous for high efficiency. The scaling of the efficiency with the square of the THz frequency enables significantly higher efficiencies at higher THz frequencies and makes it challenging to achieve comparable values at low THz frequencies [95]. But in a realistic model of intense THz sources, in addition to OR, usually other effects need to be taken into account, such as linear absorption in the THz range, determined by the complex dielectric function of the material, absorption of pump light, especially multiphoton absorption, which can cause increased carrier concentration and absorption in the THz range [63, 96]. In case of very strong THz fields, the influence of the generated THz pulse on the optical pump pulse caused by their nonlinear interaction (sum and difference frequency

generation between optical and THz fields) must be taken into account [61, 97, 98]. At high pump intensities, other nonlinear effects, such as self-phase modulation, second and third-harmonic generation, or stimulated Raman scattering, may also occur. In non-collinear geometries, spatio-temporal coupling can lead to additional complexity [82]. Therefore, it's important to discuss the theoretical aspects of phase matching techniques, coherence length, nonlinear absorption process, which can affect the THz generation.

2.2.1 Velocity matching

Phase matching means maintaining a proper phase relationship between the interacting waves during propagation. When the difference between the wavevector of the generated nonlinear polarization and the wavevector of the produced light waves, Δk, is close to zero, coherent energy is constructively transferred among the waves and yields an effective nonlinear interaction [99]. It follows that the intensity of radiation, I^{NL}, generated by a second-order nonlinear optical process is proportional to a phase mismatch factor:

$$I^{\mathrm{NL}} \propto \mathrm{sinc}^2\left(\frac{\Delta k L}{2}\right). \tag{2.14}$$

A phase mismatch produces destructive interference between the THz field contributions generated at different propagation distances within the nonlinear crystal, resulting in low THz generating efficiency. The efficiency of OR is highest when the phase matching condition, Δk=0, is fulfilled [82, 86, 94],

$$\Delta k = k(\Omega) + k(\omega_0) - k(\omega_0 + \Omega) \approx k(\Omega) - \left.\frac{\partial k}{\partial \omega}\right|_{\omega_0} \cdot \Omega. \tag{2.15}$$

The second, approximate equation holds if $\Omega \ll \omega_0$, which is usually valid for THz generation by OR. In case of collinear phase matching, Equation 2.15 gives. $\Delta k = |\Delta \mathbf{k}| = [n(\Omega) - n_{\mathrm{g}}(\omega_0)] \cdot \Omega / c$. To meet the phase-matching criteria, the phase velocity of the generated terahertz pulses must match the optical group velocity of the femtosecond laser pulses. The phase matching criterion ensures that the generated THz pulses are in synchronization with the optical pulses [100]. Thus, in case of phase matching, the phase velocity of the generated THz radiation, $\nu(\Omega) = c/n(\Omega)$, equals the group velocity of the optical pump pulse, $\nu_{\mathrm{g}}(\omega_0) = c/n_{\mathrm{g}}(\omega_0)$, and the following velocity matching condition holds.

$$\nu(\Omega) = \nu_{\mathrm{g}}(\omega_0). \tag{2.16}$$

Other than the nonlinear polarization, OR is also influenced by the dispersion of the medium. If the simplest case of an instantaneously responding medium is considered, where there is no dispersion in the THz range, and phase matching is also perfect, the electric field of the THz pulse will shape as the time derivative of the optical pulse envelope. This means that single-cycle THz pulses can be generated for Gaussian-like pump pulse envelopes. In collinear phase-matching geometry, generated THz waves propagate in the same direction as the pump

beam. This results in not only on long interaction lengths but also in generation of THz pulses with excellent beam quality. This can be achieved by selecting an appropriate phase-matching wavelength or frequency [4]. Except of a few specific cases, velocity matching is not fulfilled in a collinear geometry, for example impossible in some THz sources when pumped at long infrared wavelengths [65, 67, 69]. The reason is that the THz refractive index $n(\Omega)$ is usually different from the group index $n_{\mathrm{g}}(\omega_0)$ [101], and the group velocity of the optical pulse does not match the phase velocity of the generated THz pulses. Hence, there is mismatch which affects THz generation and yield. In this case, phase-matching conditions can only be fulfilled via different techniques like tilted pulse front technique [100], birefringent phase matching [102, 103] and quasi-phase matching [104, 105].

Coherence length: The coherence length l_{c} for optical rectification, determines the maximum thickness of the crystal that can be used to enhance the generation and detection efficiency of THz radiation. It is defined as [106]:

$$l_{\mathrm{c}} = \frac{\pi}{\Delta k} = \frac{c}{2\nu(\Omega)|n(\Omega) - n_{\mathrm{g}}(\omega_0)|}. \tag{2.17}$$

According to Equation 2.17, the maximum coherence length occurs when the refractive index of THz radiation equals the group index of the laser pulses [107, 108]. For efficient THz generation from nonlinear crystals, and in order to avoid conversion cancellation due to phase mismatch between the optical laser pulse and THz pulse the thickness of the THz generator crystal should be shorter than the interaction length. Additionally, for effective THz pulse generation, a larger interaction of the laser pulse inside the crystal is essential. Birefringence has been utilized to attain extended coherence lengths [4, 82]. If velocity matching is provided for a specific pair of THz and optical frequencies, the velocity-matching bandwidth in OR is limited by the dispersion of the THz refractive index and/or by the dispersion of the optical group index.

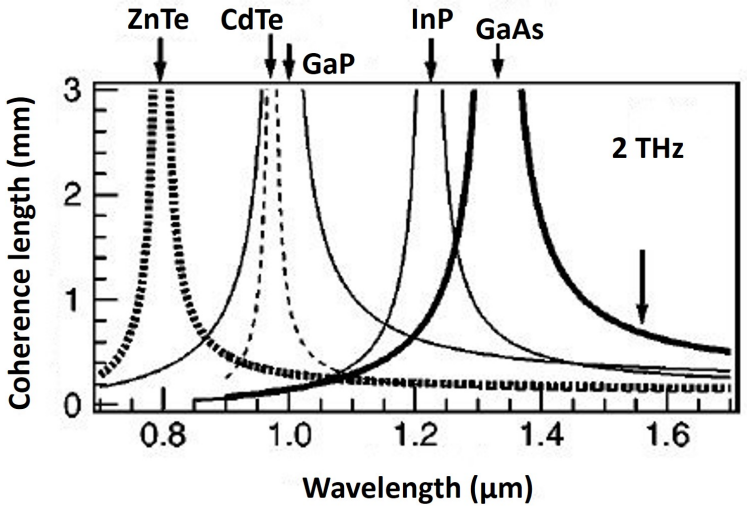

Figure 2.3: Coherence length as a function of optical wavelength for selected zincblende semiconductors at 2 THz phase-matching frequency [109].

Figure 2.3 shows the coherence length behavior of several zincblende semiconductors plotted as a function of the optical pump wavelength, illustrating how each material's phase-matching characteristics vary across the near-infrared region. ZnTe shows a pronounced increase in coherence length when pumped at 0.8 μm, making it the most effective zincblende electro-optic crystal for generating and detecting THz pulses with a 0.8 μm laser system [110]. As illustrated in Figure 2.3, this enhancement arises from favorable phase-matching conditions between the optical pump and the THz wave. Other zincblende semiconductors exhibit their optimal collinear phase-matching wavelengths at longer pump wavelengths for a 2 THz phase-matching frequency, with CdTe phase-matched at 0.97 μm, GaP at 1 μm, InP at 1.22 μm, and GaAs at 1.33 μm, as shown in Figure 2.3.

2.2.2 Velocity matching by tilting the pump pulse front

Phase matching, as introduced in Section 2.2, can be achieved, in certain nonlinear crystals, such as GaSe, by relying on the intrinsic birefringence. In contrast, many widely used semiconductor materials, ZnTe, GaP, and GaAs, are optically isotropic, which means they do not provide birefringence as a tuning mechanism. As a result, achieving collinear phase matching in these materials is only possible for very specific combinations of pump wavelength and THz output frequency. A commonly cited example is ZnTe driven with an 0.8 μm pump, which supports efficient generation of THz radiation near 1 THz [111]. At wavelengths or in materials where collinear phase matching fails, a noncollinear geometry known as tilted-pulse-front pumping (TPFP) can be used [100] for the cases where the THz refractive index is larger than the optical group index . TPFP compensates for strong refractive-index mismatch by tilting the pump pulse front so that the optical pump no longer outruns the generated THz wave. It enables the generation of high energy, single cycle THz pulses by compensating for the large mismatch between the optical group velocity and the much slower THz phase velocity. Hebling et al. [100] proposed tilting the intensity front of the pump pulse to achieve velocity matching in LN. The THz radiation, excited by the tilted pulse front, propagates perpendicular to it, with the angle between THz and pump pulse directions matching the tilt angle γ of the pulse front. Then, instead of Equation 2.16, the velocities satisfy the following [100]:

$$\nu(\Omega) = \nu_{\mathrm{g}}(\omega_0)\cos\gamma. \tag{2.18}$$

In terms of refractive index this can be expressed as:

$$n(\Omega)\cos\gamma = n_{\mathrm{g}}(\omega_0). \tag{2.19}$$

If $\nu_{\mathrm{g}}(\omega_0) \geq \nu(\Omega)$ $(n_{\mathrm{g}}(\omega_0) \leq n(\Omega))$, then this modified velocity-matching condition can be fulfilled by an appropriate choice of the angle γ. Pulse-front tilting of a light beam necessarily leads to angular dispersion. The expression linking the PFT angle γ of the excited THz pulses and the angular dispersion introduced by the dispersive element is given by [112]:

$$\tan\gamma = -\frac{n}{n_g}\lambda\frac{d\varepsilon}{d\lambda}. \tag{2.20}$$

Here, n is the optical refractive index, n_g is the group refractive index at wavelength λ, and $d\varepsilon/d\lambda$ is the angular dispersion introduced by the grating, where:

$$n_g = n - \lambda\frac{dn}{d\lambda}. \tag{2.21}$$

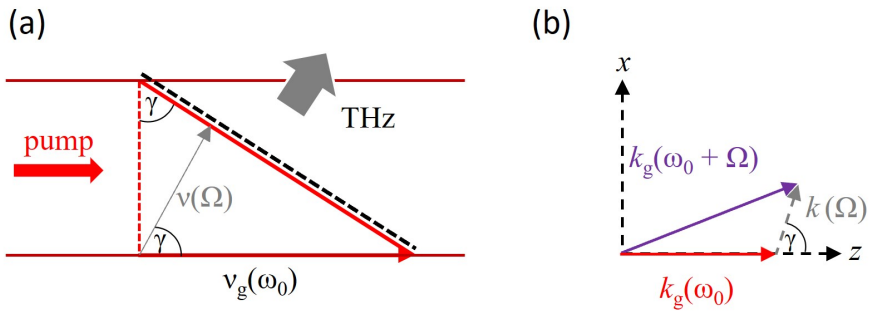

Figure 2.4: (a) Illustration of velocity matching using tilted-pulse-front with pump pulse front and THz phase front (thick black dashed line) [90, 91] (b) Noncollinear phase matching in TPFP for the wavevectors [100].

Figure 2.4(a) illustrates that THz pulses generated by the tilted pulse front propagate perpendicular to pump pulse front, satisfying the phase-matching criteria. Figure 2.4(b) shows the scheme of tilted pulse front pumping (TPFP) in terms of wavevectors. Different frequencies ω and $\omega+\Omega$ propagate in the nonlinear medium in different directions depending on the amount of angular dispersion introduced on the pump by the grating [113]. Tilted-pulse-front pumping (TPFP) has implemented as a reference technique which enables efficient THz generation in lithium niobate [100] by using angular dispersion to tilt the optical pulse front and match the THz phase velocity (see Figure 2.5). A diffraction grating introduces frequency-dependent angles, and an imaging system converts this angular dispersion into a uniform pulse-front tilt optimized for lithium niobate. Because the tilted front cannot be aligned with planar crystal surfaces while maintaining perpendicular pump incidence and THz outcoupling, a prism-shaped LN crystal with a wedge angle equal to the pulse-front tilt (63 °) is used. This geometry preserves velocity matching inside the crystal while minimizing reflection losses and preventing THz angular dispersion, forming the core of the TPFP scheme.

The angular dispersion contributes to the group-velocity dispersion (GVD) [114], which causes chirping, and broadening of the pulse duration. The GVD parameter can be written as [112, 115]:

$$\mathrm{GVD} = \frac{d\left(v_g^{-1}\right)}{d\lambda} = \frac{\lambda}{c}\left[n\left(\frac{d\varepsilon}{d\lambda}\right)^2 - \frac{d^2n}{d\lambda^2}\right], \tag{2.22}$$

where the first and second terms originate from angular dispersion and material dispersion,

respectively. For a large pulse-front-tilt angle, the former can dominate over the latter, thus significantly improving the variation of the pump pulse duration with the propagation distance [116].

The introduction of the tilted pulse front pumping (TPFP) technique [100] significantly enhanced THz pulse generation efficiency and THz pulse energy by several orders of magnitude [117, 118], achieving pulse energies of 10 μJ [119], 30 μJ [120], and 50 μJ [121] with efficiencies around 1% [93, 121]. Peak electric fields of 2.1 MV/cm were recorded [122, 123] using pump pulses of about 100 fs. Using a 1030 nm Yb:YAG laser with a pulse duration of 1.3 ps, THz pulses of 125 μJ with 0.25% efficiency were achieved at room temperature [124]. Xu et al. reported generation of 0.2 mJ THz pulses with 0.3% efficiency at room temperature using a 0.8 μm Ti:Sapphire laser with a pulse duration of 50 fs [125]. Further improvements with a pump fluence of 186 mJ/cm^2 and pulse duration of 785 fs yielded over 0.4 mJ energy and 0.77% efficiency at room temperature [93]. The maximum reported THz pulse energy till now is 13.9 mJ, with a peak electric field of 7.5 MV/cm [59].

2.3 Materials for optical rectification

A wide range of materials can be used for optical rectification (OR), spanning several distinct classes. There are numerous materials suitable for OR, including lithium niobate (LN) and lithium tantalate ($LiTaO_3$), common choices in ferroelectric crystals, semiconductor materials including ZnTe, GaP, GaAs, GaSe, CdTe, and organic materials such as DAST, OH1, DSTMS, HMQ-TMS, BNA, MNA, NMBA, which offer exceptionally large nonlinear coefficients that make them attractive for efficient THz generation. Comprehensive comparisons of their performance and physical characteristics are available in the literature [63, 74, 80, 90, 91, 101, 126–130]. The figure of merit (FOM) for terahertz (THz) generator crystals quantifies how effectively a material can convert optical pump light into THz radiation, typically through optical rectification (OR) or difference-frequency generation (DFG). A high FOM indicates that the crystal can generate intense, broadband THz pulses with high conversion efficiency. Based on Equation 2.13, the figure of merit is given by [101]

$$\mathrm{FOM}_{\mathrm{THz}} = \frac{(d_{\mathrm{eff}})^2}{n(\omega_0)^2 \cdot n(\Omega) \cdot \alpha^2(\Omega)}, \tag{2.23}$$

where $d_{\mathrm{eff}} = \frac{1}{4} n(\omega_0)^4 \cdot r$ [131] is the nonlinear optical coefficient for optical rectification, $\alpha(\Omega)$ is the absorption coefficient for the THz radiation for strongly absorbing crystals, and r is the electro-optic coefficient of the NLO material. Several non-centrosymmetric crystals with high FOM have been investigated to generate THz pulses by optical rectification [91]. Selecting the right nonlinear material is one of the most decisive choices in designing an efficient THz source. The material fundamentally determines the achievable conversion efficiency, usable pump wavelengths, and the overall performance of the THz generation process. Several key properties must be evaluated carefully, including the effective nonlinear coefficient, the transparency range of the material, and the ability to achieve phase and velocity matching between the pump pulse and the generated THz field. Equally important are the material's THz

absorption characteristics, which directly limit the output bandwidth and efficiency, as well as its bandgap, which constrains the maximum pump intensity and helps avoid multi-photon absorption or optical damage. Table 2.1 list some of the nonlinear materials most suitable for optical rectification. The following section provides a concise overview of the key OR relevant properties of these material classes.

Table 2.1: Properties of materials most suitable for THz generation via optical rectification. THz refrective index, $n(\Omega)$ and the absorption coefficient, $\alpha(\Omega)$, are given for 1 THz.

Material	λ (nm)	$n_g(\omega)$	$n(\Omega)$	r (pm/V)	d_{eff} (pm/V)	$\alpha(\Omega)$ (cm^{-1})	Bandgap(eV)
ZnTe	800	3.2 [132]	3.17 [133]	4.04	68.5 [126]	1.3	2.26 [134]
GaP	800	3.57 [135]	3.34 [135]	0.97	24.8 [136]	0.2	2.79 [137]
$LiNbO_3$	800	2.23 [138]	5.16 [139]	30.9	168 [100]	17	3.7 [140]
BNA	800	2.03 [141]	2.0 [142]	85	234[141]	5.9	2.50[143]
NMBA	800	2.20 [144]	2.11 [145]	34	139 [144]	2.8	2.75 [143]
MNA	800	2.70 [146]	2.50 [147]	67	250 [148]	4.2	2.56 [143]
DAST	1535	2.26 [149]	2.4 [150]	47	242 [149]	50	2.19 [149]

2.3.1 Lithium niobate

Lithium niobate ($\mathrm{LiNbO_3}$, LN) is a critical nonlinear material utilized in intense pulsed THz sources, showcasing its versatility across various applications due to its electro-optic, piezo-electric, acousto-optic, photorefractive, pyro-electric, and photovoltaic properties. Developed at Bell Laboratories in the mid-1960s, LN is a colorless, water-insoluble solid transparent from 350 to 5200 nm, exhibiting a trigonal crystal system [151] with ferroelectricity and nonlinear optical polarizability. Its physical properties, including photorefraction and conductivity, can be controlled by its composition, significantly influenced by the growth method. LN displays negative uniaxial birefringence, slightly varying with crystal stoichiometry and temperature. There are two primary crystal types: congruent LN (cLN) with a Li to Nb ratio of 0.945, and stoichiometric LN (sLN) at 0.979 [152]. sLN possesses a lower optical damage threshold but a larger electro-optic coefficient [153]compared to cLN [154–156]. Controlling stoichiometry and doping, such as with magnesium oxide (MgO) (0.5-6$\%$), enhances resistance to photorefractive damage [157] and increase the damage threshold up to 100 GW/cm^2. Research indicates that 0.7 mol$\%$ Mg-doped sLN demonstrates optimal potential as a THz source due to its low THz absorption coefficient, a significant finding by Palfalvi et al [158]that relates to the temperature dependence of both refractive index and absorption. It is considered the optimal configuration for because it reaches the photorefractive threshold with minimal dopants, resulting in high laser-induced damage resistance and low absorption. This precise doping level removes antisite defects to minimize phonon damping, ensuring superior phase-matching efficiency and transparency compared to conventional crystals. The optical properties and parameters for cLN and sLN crystals can be found in references [159, 160].

It is a key material for high-intensity THz sources [63, 90, 91, 101, 126, 158, 161] with high figure of merit (18.2 pm^{2}cm^2/V^2), characterized by a high effective nonlinear coefficient ($d_{\text{eff}} = d_{33}$=168 pm/V) and large bandgap (3.8 eV). The earliest THz generation from LN

occurred in 1971 [162], though initial efficiencies were low due to phase matching challenges. Despite its optical anisotropy, birefringence cannot be used for phase matching below the transverse optical phonon frequency [158, 160, 163], as lattice vibration contributes strongly to its dielectric function [101]. Due to very different optical group and THz phase velocities a large phase matching angle of approximately 63° is needed. For optimal THz generation via optical rectification (OR), pump and THz fields must be polarized along the Z axis of LN. The THz absorption coefficient is significant (16 cm^{-1} at 1 THz at room temperature), but can be reduced below 5 cm^{-1} at cryogenic temperatures [139, 158, 163], limiting the usable THz range to about 4.5 THz due to phonon absorption. LN also allows for high-intensity pumping [163, 164] due to its high damage threshold, with multiphoton absorption (MPA) playing a minor role given its large bandgap (3.8 eV). The lowest order effective MPA is three-photon absorption (3PA) and four-photon absorption (4PA) at 800 nm and 1030 nm pump wavelength, respectively.

In lithium niobate (LN), for instance, optical pump group and THz phase velocities mismatch is so large that efficient THz generation would be impossible without additional engineering. By tilting the pulse front of the femtosecond pump, typically with a diffraction grating, an echelon, or similar optical elements, the component of the optical group velocity is reduced to match the THz phase velocity [100]. Achieving this velocity matching greatly enhances conversion efficiency, making it possible to generate mJ scale THz pulses with electric fields on the order of few megavolts per centimeter [59].

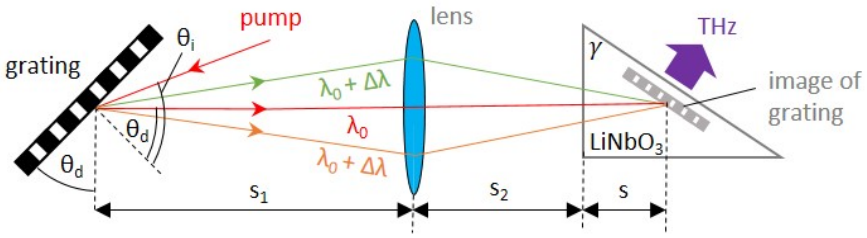

Figure 2.5: Scheme of a Tilted-pulse-front-pumping (TPFP) setup using a reflection grating for pulse front tilt, a imaging lens and a $LiNbO_3$ prism for THz generation. [63].

Figure 2.5 shows the pulse-front-tilting setup and its parameters for $LiNbO_3$ prism. The angles θ_i and θ_d denote the incidence and diffraction angles at the grating, respectively. The angle θ_d also defines the tilt angle of the grating. The distance s is measured between the image of the grating and the crystal input surface along the optical axis. The value of s is chosen such that the region of effective THz generation (the gray-shaded area in Figure 2.5) is not truncated [63].

Using longer pump pulses shifts the THz spectrum to lower frequencies, further reducing crystal absorption and extending the generation length [165]. However, pumping at 1 μm shows limitations due to frequency down-shifting and spectral broadening from angular dispersion [61]. Maximal diffraction efficiency typically occurs in Littrow geometry; thus, incidence angles near the Littrow angle, $\theta_{\text{Littrow}} = \sin^{-1}(\lambda_0/2p)$ are preferred. Here λ_0 is the design wavelength and p is the grating period. Attempting to increase THz energy through larger pump energies and sizes encounters issues, such as non-uniform pump propagation

length due to the wedge angle of the LN crystal. Conventional pulse-front-tilt setups employing diffraction gratings and imaging optics can distort the pump and THz beams, reducing THz yield [166]. The main issue with imaging is the curved image surface which becomes more significant with larger beam cross sections. This results in a separation of the pulse front and the image (location of shortest pulse duration and highest intensity) surfaces. The required PFT angle relates to angular dispersion and group velocity dispersion (GVD), where large angles necessary for phase matching correspond to significant GVD causing pulse duration broadening, inversely affecting pump intensity [165]. Moreover, tilting the pump pulsed beam complicates the focusing of generated THz due to distortion in the intensity profile [122]. To address these challenges, eliminating imaging optics by directly contacting the grating with the nonlinear crystal minimizes imaging errors. This configuration allows a more effective use of the larger pumped area and improves THz energy and beam quality [39, 167].

Various enhancements to the TPFP method have emerged, including a contact grating (CG) for distortion-free pulse front tilting [39], producing THz pulses with 0.41 μJ at a conversion efficiency of 1.5 $\times 10^{-4}$ using 2.7 mJ pump energy [168]; yet, the CG implementation in LN is difficult due to required large PFT angles. A contact grating (CG) is a technology used in terahertz (THz) generation to produce distortion-free pulse front tilting (PFT) by placing a transmission grating directly on the entrance face of a nonlinear crystal [167, 169]. This configuration, introduced to overcome the limitations of imaging and beam quality degradation. The main advantage of CG is the improved lateral scalability, allowing, in principle, larger beam sizes and larger pulse energies. Hybrid schemes combining TPFP with imaging optics face practical challenges due to varying interaction lengths, impacting THz beam focusability. Nevertheless, fabrication of contact gratings remains a challenge, leading to the development of hybrid THz pulse sources combining conventional and contact grating setups [170], with pulse-front-tilt produced in two steps. A new approach involving reflecting the pump beam on a stair-step echelon is explored. This arrangement creates a segmented tilted pulse front instead of a continuous one, while still requiring a prism-shaped LN crystal. A modified hybrid method has been proposed comprising diffraction optics coupled with a nonlinear LN slab featuring an echelon configuration. This innovative setup ensures uniform absorption and dispersion across the THz beam profile, as a segmented tilted pulse front forms within the LN slab, optimizing interaction lengths and reducing imaging errors, ultimately facilitating the realization of scalable THz pulse sources with superior beam quality. Additionally, employing plane-parallel LN with an echelon structure [171] has been successfully executed, resulting in THz pulse energies of 1 μJ and conversion efficiency of 5×10^{-4} [172]. This method allows for scaling in THz pulse energies by increasing pump spot size and energy.

2.3.2 Semiconductors

Semiconductors have become indispensable materials in modern terahertz (THz) science, serving both as efficient THz emitters and detectors across a wide range of experimental platforms. Their relevance stems from their dual functionality: they act as nonlinear optical media for optical rectification (OR) [96, 173], difference frequency generation (DFG) [174], and optical parametric amplification (OPA) [175], while also forming the photoconductive

substrates used in biased and unbiased antenna structures [176–182]. In THz time domain spectroscopy, semiconductor based photoconductive antennas remain the most common low energy THz sources, and large area antenna geometries have enabled pulse energies up to 3.6 μJ with peak electric fields of 143 kV/cm and spectral coverage from 0.05 to 1 THz [183–185]. Although such devices allow limited pulse shaping, scaling them to substantially higher energies remains challenging due to carrier screening and thermal constraints.

A broad class of III–V and II–VI semiconductors, including ZnTe, GaP, GaAs, CdTe, and InP, exhibit properties that make them attractive for THz generation via optical rectification. Their second order nonlinear coefficients typically fall in the range of 25–80 pm/V [63, 90, 91, 101, 126, 161], with representative values of d_{eff}=68.5 pm/V for ZnTe, 65.6 pm/V for GaAs, and 24.8 pm/V for GaP [90, 126]. Although these coefficients are modest compared to lithium niobate or organic crystals, many semiconductors compensate through their relatively low THz absorption (within 1 THz), typically between 0.5 and 3 cm^{-1} [90, 101, 133]. Their high transverse optical phonon frequencies, such as 11 THz in GaP, enable broadband THz emission extending well beyond 5 THz [101, 186]. Furthermore, many of these materials, allow simple collinear phase matching at specific pump wavelengths: ZnTe at 0.8 μm, GaP at 1 μm, and GaAs near 1.3–1.5 μm [14]. These wavelengths coincide with widely available Ti:sapphire, Yb doped, and Er doped femtosecond laser systems, making semiconductor based THz sources experimentally accessible.

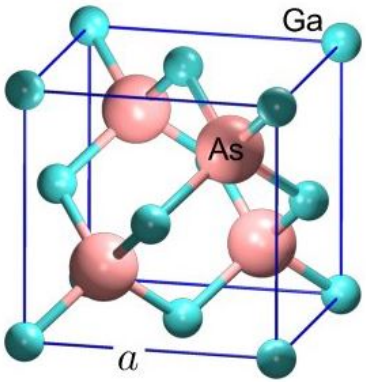

Figure 2.6: The cubic unit cell structure for gallium phosphide [187].

Despite these advantages, THz generation in semiconductors is strongly limited by low order multiphoton absorption (MPA). At common pump wavelengths, two photon absorption (2PA) generates free carriers that introduce significant free carrier absorption (FCA) of the THz field, thereby restricting the usable pump intensity and suppressing conversion efficiency [96]. This effect is particularly severe in ZnTe and GaAs when pumped at 800 nm. As a result, THz energies from collinearly pumped ZnTe typically saturate at the μJ level, with efficiencies around 10^{-5} [188]. Large aperture ZnTe crystals can mitigate saturation by reducing local fluence, but FCA remains the dominant limiting mechanism [189, 190].

In gallium phosphide (GaP), each atom is in the centre of a regular tetrahedron, with atoms of the other kind at each of its four corners, as shown in Figure 2.6. GaP has emerged as a promising alternative due to its wide transparency range, low THz absorption $\sim$ 3 cm^{-1} at 1 THz, and high phonon frequency near 11 THz [191–193]. Optimal velocity matching occurs

near 1 μm, where GaP exhibits minimal linear absorption and avoids strong 2PA. Experiments using Yb fiber lasers have demonstrated average THz powers of 6.5 μW with 210 fs pulses [194], 82.6 μW with chirped sub 60 fs pulses [195], and broadband emission up to 5 THz using 20 fs pulses at 1 μm [193]. GaP's ability to support high average power pumping while maintaining broad bandwidth makes it particularly attractive for MHz repetition rate THz systems. GaAs, with its large nonlinear coefficient and broad transmission range, also benefits significantly from long wavelength pumping. When driven at 1.8 μm, beyond the 2-photon absorption edge, GaAs has produced THz pulses with energies of 0.6 μJ and efficiencies of 5×10^{-4} [67]. Figure 2.7 shows the cut-off wavelengths up to 4 μm for MPA of various orders are indicated by symbols for a few different materials. The direct bandgap of ZnTe is 2.26 eV and that of GaP is 2.79 eV. These are sufficiently large to avoid both two- and three-photon absorption for pump wavelengths longer than 1.65 μm [65].

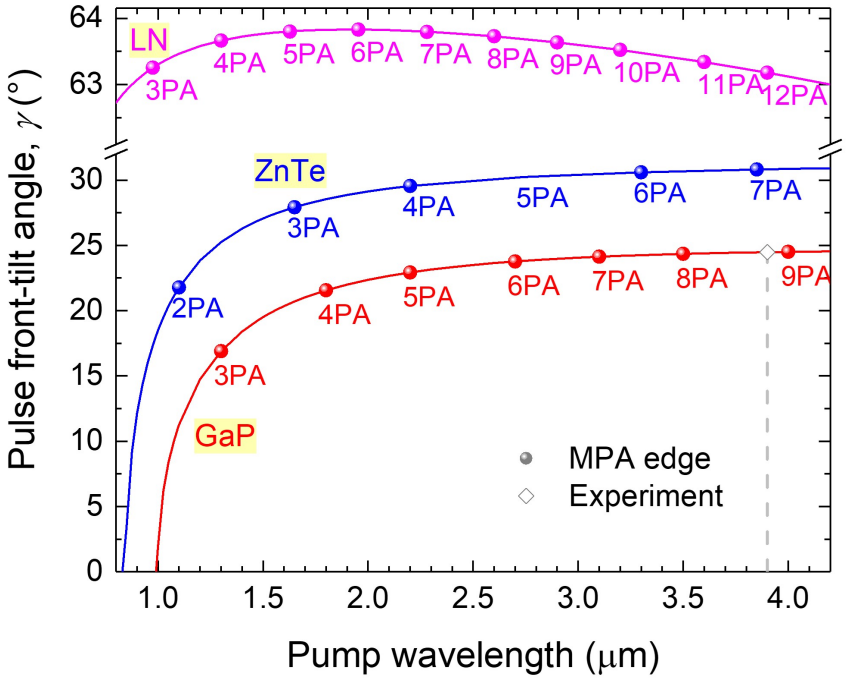

Figure 2.7: PFT angle versus pump wavelength for phase matching at 1 THz in LN and selected semiconductors considering the direct bandgap [65]. The symbols (circles) indicate the cut-off wavelengths for MPA of various orders. The dashed vertical line and the diamond symbols indicate the wavelength and material used in the experiment described in Chapter 4.

GaSe is also suitable, though its 2.02 eV bandgap requires pump wavelengths >1.85 μm to suppress two- and three-photon absorption. Such wavelengths are readily produced by Ti:sapphire- or Yb-pumped OPAs, as well as Ho-based lasers operating near 2.05 μm [196, 197]. Materials with much smaller bandgaps, such as CdTe or GaAs (both 1.43 eV) [198], would demand even longer pump wavelengths to avoid nonlinear absorption, making them less practical. For this reason, ZnTe and GaP remain the preferred choices. The use of longer pump wavelengths has become a central strategy for overcoming multiphoton absorption in semiconductors. Pumping beyond the 2-photon and 3-photon thresholds dramatically reduces free carrier generation, enabling higher pump intensities and improved THz conversion

efficiencies [63, 198]. However, at these wavelengths, collinear phase matching is no longer satisfied, necessitating the use of tilted pulse front (TPF) or contact grating (CG) techniques. The pulse front tilt angles required for pump–THz velocity matching in semiconductors are relatively small—typically below 30° [65]—which minimizes spatial nonuniformity, reduces angular dispersion, and allows longer effective interaction lengths. The CG approach, in particular, enables monolithic THz sources in which a grating structure fabricated directly on the entrance surface of the semiconductor crystal plate tilts the intensity front of the pump pulse [39]. This eliminates the need for conventional external TPF optics and offers excellent scalability to large apertures and high pulse energies. Using CG based TPF, ZnTe has produced THz pulses with energies of 3.9 μJ, peak fields of 0.57 MV/cm, and efficiencies of 0.3$\%$ [69], two orders of magnitude higher than earlier collinear results at shorter wavelengths [188]. Even higher performance has been demonstrated by pumping ZnTe at 1.7 μm, yielding THz energies up to 14 μJ with efficiencies of 0.7$\%$ [65]. CG technology has also been adapted to GaP pumped at 1 μm [199] and implemented in THz time domain spectroscopy systems [200].

Overall, semiconductor materials offer a compelling combination of moderate nonlinearity, low THz absorption, broad bandwidth, and compatibility with high power femtosecond laser systems. Their small required pulse front tilt angles and favorable dispersion properties allow long interaction lengths that compensate for their lower nonlinear coefficients. With the advent of long wavelength pumping and advanced TPF/CG techniques, semiconductors such as GaP, GaAs, and ZnTe have demonstrated scalable THz pulse energies upto 14 μJ [65], efficiencies approaching 1$\%$, and spectral coverage extending beyond 5–7 THz. These developments position semiconductor crystals as strong candidates for next generation high energy, broadband THz sources suitable for both table top and high repetition rate laser systems.

2.3.3 Organic crystals

Organic nonlinear optical crystals have emerged as leading materials for generating high field terahertz (THz) radiation via optical rectification (OR) of femtosecond laser pulses. The most widely used crystals include DAST, DSTMS, BNA, OH1, and HMQ TMS [73, 74, 76–80, 128, 145, 201–212]. These organic salts exhibit exceptionally large second order nonlinear coefficients, among the highest of all materials used for OR, with reported values such as d_{eff}=615 pm/V for DAST [204]. Their high nonlinear figure of merit (FOM) enables efficient THz generation with broad spectral coverage extending from 0.1 THz up to 20 THz in favorable cases [203, 206–208, 210]. A key advantage of organic crystals is their collinear phase matching behavior in the 1.2–1.6 μm pump wavelength range, which naturally produces collimated, aberration free THz beams with excellent focusability and high achievable field strengths [128, 208, 213] Pumping at shorter wavelengths (e.g., Ti:sapphire at 0.8 μm) generally restricts phase matching to frequencies below 1 THz [214], although some crystals such as NMBA, BNA, and MNA can be pumped directly by Ti:sapphire or Yb based lasers [79, 80, 145]. At these shorter wavelengths, however, two and three photon absorption can induce significant heating and free carrier generation, reducing THz efficiency and potentially damaging the crystal due to their relatively low melting points (101–131° C) [80, 145, 148].

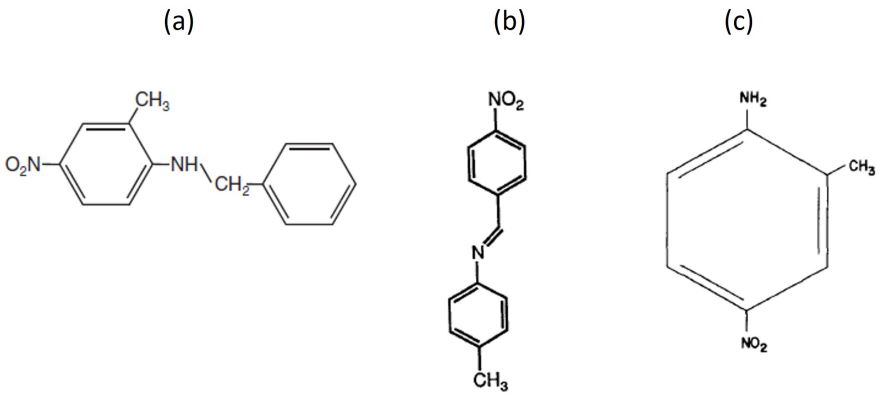

Figure 2.8: Chemical structure of the commonly used organic crystals (a) N-benzyl-2-methyl-4-nitroaniline (BNA), (b) 4-nitro-4'-methylbenzylidene aniline (NMBA), and (c) 2-methyl-4-nitroaniline (MNA). From Ref. [144, 148, 205].

Despite their small typical dimensions (millimeter scale lateral size and hundreds of micrometers thickness) [[76], organic crystals have demonstrated remarkable THz pulse energies and field strengths. Partitioned aperture crystal designs can overcome size limitations [201, 213], enabling record level performance. A 400 mm^2 partitioned DSTMS crystal produced 0.9 mJ THz pulses with 42 MV/cm electric and 14 T magnetic peak fields when pumped by a 30 mJ Cr:forsterite laser at 1.25 μm, achieving 3% conversion efficiency [76]. Even higher conversion efficiencies up to 6% have been reported in DAST pumped by a high power mid IR OPCPA at 3.9 μm [78]. Field strengths exceeding 10 MV/cm and 3 T have been demonstrated using Cr:forsterite lasers directly pumping various organic crystals [128]. However, scaling THz energies in organic materials remains challenging due to strong phonon absorption at low THz frequencies, limited crystal size, and relatively low optical damage thresholds [76, 87, 213]. White light seeded OPAs, often used to reach the required 1.2–1.6 μm pump wavelengths, suffer from low conversion efficiency, irregular beam profiles, and shot to shot fluctuations, which limit usable pump fluence and reduce THz stability [128, 213]. Improved thermal management, such as bonding crystals to sapphire or diamond substrates, can mitigate multiphoton absorption induced heating and increase the damage threshold [79, 215].

Organic crystals remain among the most promising materials for generating intense, broadband THz pulses with high efficiencies, due to their large nonlinearities, favorable phase matching properties. Continued advances in crystal engineering, thermal management, and pump laser technology are expected to further enhance their performance for strong field THz science and applications.

2.4 Terahertz detection

Analogous to the previous section on THz generation, the detection of THz radiation also encompasses several possible techniques, each with its own application range, benefits, and limitations. Detecting THz frequencies is inherently challenging because established methods from either the optical or radio-frequency domains cannot be directly applied. At THz

energies, the photon energy is too low for conventional photodetection schemes used at optical wavelengths, while the frequencies are too high for standard electronic detection techniques developed for radio-frequency signals. As a result, specialized detection concepts are required to address the unique characteristics of the THz regime.

2.4.1 Measurement of pulse energy

The relatively low output power of most THz sources, combined with strong atmospheric absorption, places stringent demands on detector sensitivity, responsivity, and noise performance. THz detection techniques are generally categorized into coherent and incoherent (direct) detection schemes. Coherent detectors, including Schottky diode mixers and superconducting hot electron bolometers, provide access to both the amplitude and phase of the incident field but require a stable local oscillator for heterodyne operation. In contrast, incoherent detectors measure only the total incident power and encompass a variety of technologies such as thermal detectors, pyroelectric sensors, Golay cells, and microbolometers [216–218]. Among these, thermal detectors are particularly attractive due to their inherently broadband spectral response, room temperature operation, and robustness against electromagnetic interference. Thermal detectors operate by converting incident THz radiation into heat. Their core structure consists of a THz absorbing element that is thermally linked to a heat sink. When THz radiation is absorbed, the electromagnetic energy is transformed into a temperature rise within the absorber. This temperature change is subsequently measured by an integrated thermometer element, whose electrical response is directly proportional to the absorbed energy. By applying appropriate calibration procedures, the detector output can be quantitatively related to the incident THz power or energy with high accuracy [219–221].

Pyroelectric detectors form an important subclass of thermal sensors and rely on the intrinsic properties of pyroelectric crystals. These crystals exhibit spontaneous polarization, meaning each unit cell possesses a permanent electric dipole moment aligned along a specific crystallographic axis. The magnitude of this spontaneous polarization is temperature dependent. The polarization is accompanied by bound surface charge, which is normally neutralized by free carriers or by external electrodes, establishing a steady state equilibrium. For detector fabrication, the pyroelectric crystal is typically cut perpendicular to its polar axis and sandwiched between two electrodes. One electrode surface is often coated with an absorbing layer to enhance coupling to incident radiation. When THz or optical radiation is absorbed, the resulting heat increases the crystal temperature, reducing the spontaneous polarization and altering the associated surface charge [14]. Because the electrodes form a capacitor, any change in surface charge induces a transient current in a closed circuit as the system attempts to restore charge neutrality. To maximize responsivity, the detector is usually operated with a large load resistance, and the resulting voltage signal is further amplified using a low noise operational amplifier. Since pyroelectric detectors respond only to changes in temperature, no pyroelectric current is generated under steady state illumination. Consequently, these detectors are typically used with modulated radiation, such as chopped THz beams or pulsed light sources, enabling AC detection with high signal to noise ratio [222–227]. Common pyroelectric materials include triglycine sulfate (TGS), lithium tantalate ($\mathrm{LiTaO_3}$), and polyvinylidene fluoride (PVDF), each offering distinct advantages in terms of sensitivity, thermal stability,

dielectric properties, and fabrication complexity [228–230].

Pyroelectric detectors are essential for applications requiring room-temperature operation [231]. They are highly relevant for terahertz (THz) power and energy measurement, serving as one of the primary, versatile technologies for characterizing THz radiation, in a broadband range [196]. Their ability to provide high sensitivity and reliability, makes them the standard for many practical and industrial THz applications [232].

2.4.2 Electro-optic sampling

Electro-optic sampling (EOS) is a widely used technique for detecting instantaneous electric field of the pulse by measuring the differential signal, which is linearly proportional to the electric field strength. It relies on the second-order nonlinear interaction between an applied electric field and an optical probe pulse in a non-centrosymmetric crystal. Static or low-frequency electric fields modify the refractive index of such materials through the electro-optic (Pockels) effect [82]. In a lossless medium, the induced second-order polarization is given by

$$P_i^{(2)} = 2\sum_{j,k} \varepsilon_0 \chi_{ijk}^{(2)}(\omega, \omega, 0)\, E_j(\omega)\, E_k(0) = \sum_j \varepsilon_0 \chi_{ij}^{(2)}(\omega)\, E_j(\omega), \tag{2.24}$$

demonstrating that the refractive index change is linearly proportional to the applied THz field. The Pockels effect shares the same nonlinear susceptibility tensor as optical rectification, since $\chi_{ij}^{(2)}(\omega) = 2\sum_k \chi_{ijk}^{(2)}(\omega, \omega, 0)\, E_k(0)$ [109].

Free-space EOS measures the electric field of THz pulses directly in the time domain by exploiting this induced birefringence [109]. Unlike traditional spectroscopic techniques, EOS provides access to both the amplitude and phase of the THz waveform. When the optical group velocity and THz phase velocity are well matched inside the electro-optic crystal, the probe pulse experiences the THz field as quasi-static during co-propagation. By scanning the relative delay between the pulses, the full temporal THz waveform can be reconstructed [109].

In the absence of a THz field, a linearly polarized probe pulse traverses the EO crystal without modification and is converted into circular polarization by a quarter-wave plate. A Wollaston prism then splits the beam into two orthogonal components of equal intensity, resulting in a zero differential signal at the balanced photodetector. When a THz field is present, the induced birefringence introduces a phase retardation over a propagation distance L given by

$$\Delta\phi = (n_y - n_x)\,\omega\frac{L}{c} = \omega\frac{L}{c}\, n_0^3 r_{41} E(\Omega), \tag{2.25}$$

where n_0 is the refractive index at the probe wavelength and r_{41} is the electro-optic coefficient [110]. For small phase shifts, the detected intensities become

$$I_x = \frac{I_0}{2}\,(1 - \sin\Delta\phi) \approx \frac{I_0}{2}\,(1 - \Delta\phi)\,, \tag{2.26}$$

$$I_y = \frac{I_0}{2}\,(1 + \sin\Delta\phi) \approx \frac{I_0}{2}\,(1 + \Delta\phi)\,, \tag{2.27}$$

yielding a differential signal

$$I_s = I_y - I_x = I_0 \Delta\phi = I_0 \frac{\omega L}{c} n_0^3 r_{41} E(\Omega) \ \propto \ E(\Omega), \tag{2.28}$$

which is directly proportional to the THz field amplitude [109].

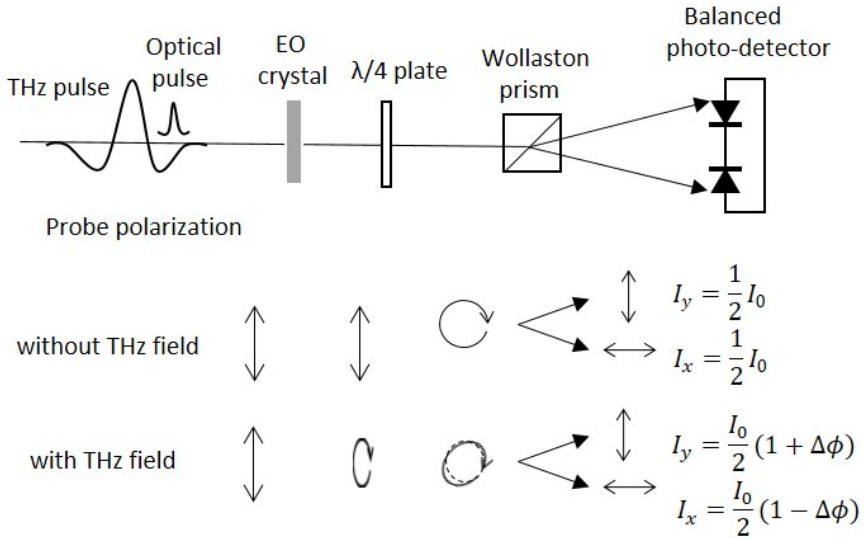

Figure 2.9: Schematic diagram of a typical setup for free-space electro-optic sampling [109].

EOS is widely used in ultrafast electronics and optoelectronics, complementing other THz detection methods such as photoconductive antennas and far-infrared interferometry [61, 233]. Its application to ultrafast electrical transients was first demonstrated by Valdmanis [234]. Coherent detection with high signal-to-noise ratio is achievable when phase-matching conditions are satisfied [235].

Common EO crystals include ZnTe and GaP. ZnTe is particularly suitable for detection at 800 nm due to its high transparency, large electro-optic coefficient, and favorable refractive-index matching between the optical and THz ranges [236]. Typical crystal thicknesses are a few hundred micrometers: thicker crystals provide stronger signals but reduced bandwidth due to phonon absorption and accumulated phase mismatch.

The performance of EOS is limited by three main factors [109]:

1. finite duration of the optical probe pulse,
2. frequency dependence of the nonlinear susceptibility,
3. mismatch between optical group velocity and THz phase velocity.

Additional constraints arise from dispersion, coherence length, and crystal orientation. For optimal detection, the probe polarization should be parallel or orthogonal to the THz polarization [236], and zinc-blende crystals are often oriented along the $[1\bar{1}0]$ axis for maximum signal strength. In cases of extremely strong THz fields, the induced phase retardation may exceed $\pi/2$, causing over-rotation of the probe polarization and reducing the detected signal;

attenuation of the THz beam may therefore be required [237]. Alternative approaches such as spectral-domain interferometric THz detection avoid this limitation [238].

2.5 Applications of intense THz pulses

Advances in terahertz (THz) technology have transformed the field from weak sources, to a regime where intense THz pulses enable active manipulation of matter. Modern high-intensity THz emitters now provide electric field strengths in the 1 – 260 MV/cm range [90, 91, 122, 239–241], granting access to unprecedented nonlinear light–matter interactions across the THz spectrum. These strong fields allow the initiation and tracking of ultrafast processes through THz pump–THz probe [242, 243] and THz pump–optical probe spectroscopy, enabling both resonant and non-resonant control of ionic, electronic, and spin degrees of freedom in a wide variety of materials [244, 245]. Comprehensive reviews of nonlinear THz interactions are also available [89, 246, 247].

Nonlinear electronic responses under intense THz excitation have been demonstrated in several platforms. Rydberg atoms, with their large transition dipole moments, exhibit strong sensitivity to THz fields [184, 248, 249]. In semiconductors, intense THz pulses have revealed ultrafast carrier heating, impact ionization, and saturation of free-carrier absorption [242, 245, 250–254]. Experiments in n-type GaAs showed coherent THz emission arising from stimulated transitions between impurity states under population inversion [245]. In InSb, THz pump–THz probe studies uncovered rapid carrier redistribution and strong nonlinear absorption [242, 252]. High-field single-cycle THz pulses have also enabled ultrafast gating of interlayer transport in cuprate superconductors, with peak fields around 150 kV/cm [255, 256]. Even stronger nonlinearities occur in single-walled carbon nanotubes, where 0.7MV/cm THz fields generate ponderomotive energies exceeding the bandgap, enabling interband excitation despite low photon energies [257].

Lattice-driven nonlinearities are equally significant. Ferroelectric materials exhibit strong anharmonicity due to double-well potentials [90, 258–260], leading to THz-frequency nonlinear coefficients that exceed optical values by orders of magnitude. For example, the nonlinear refractive index of lithium niobate (LN) in the THz regime is estimated to be three orders of magnitude larger than in the visible [90, 261]. Intense THz pulses have been used to drive the ferroelectric soft mode in $SrTiO_3$ thin films to large amplitudes, revealing quartic anharmonicity and field-induced blueshifts of the soft-mode resonance [262]. These results suggest that coherent THz control of macroscopic order parameters, including ferroelectric phase transitions, may be achievable.

Beyond materials control, intense THz pulses are emerging as a powerful tool in accelerator physics. Achieving manipulation of relativistic beams requires THz fields in the 1–10 MV/cm range, with potential extension to 100 MV/cm. Such fields enable THz-assisted enhancement of attosecond-pulse generation through control of electron trajectories in high-harmonic generation [263–267], as well as THz-driven electron acceleration, deflection, and spatiotemporal focusing [43]. Compared with microwave-based accelerators, THz-driven schemes offer reduced timing jitter and improved synchronization with ultrafast electron bunches. A

proof-of-concept experiment demonstrated 7 keV energy gain over 3 mm in a dielectric-loaded waveguide using THz acceleration [42], and theoretical models predict GeV/m gradients and electron energies in the tens of MeV range with more energetic THz sources.

THz-driven electron guns are also promising for ultrafast electron microscopy and diffraction, where high charge density and femtosecond durations are required [268]. Recent demonstrations show scalable THz-driven sources capable of delivering higher energies and larger bunch charges while preserving ultrashort pulse durations [269, 270]. THz-based post-acceleration of laser-generated proton beams has likewise been proposed [29], using evanescent THz fields in dielectric structures. Simulations indicate that a 40 MeV proton bunch could be boosted to 56 MeV through five THz stages, with significantly reduced energy spread, an important step toward compact ion accelerators for hadron therapy, which requires 100 MeV/nucleon and 1% energy stability. THz pulses in the 0.1–0.5 THz range with MV/cm fields, already demonstrated using LN sources [93], are well suited for this purpose, and THz-driven ion sources based on near-critical-density hydrogen plasma have also been proposed [38].

Chapter 3

Scientific goals

The utilization of THz radiation has increased substantially, driven by advances in ultrafast laser systems and THz generation technologies, which enabled the deployment of THz radiation across a broad range of scientific and technological applications. Optical rectification (OR) in $LiNbO_3$, combined with the tilted-pulse-front technique [100], is one of the most widely used methods to generate low THz frequencies in the range of 0.1 THz to 2 THz. However, in addition to restricted bandwidth, this technique has limitations due to the large ($\sim 63°$) pulse-front tilt angle [61, 63, 64].

Semiconductors (GaAs [67], ZnTe [65, 69] and GaP [65]) are emerging as promising sources of intense THz fields. In these materials, the bandgap is in the range of 1.4 eV to 2.8 eV, enabling two or three-photon absorption at the commonly used near-infrared laser wavelengths. Such detrimental low-order multiphoton absorption (MPA) of the pump [86, 96] can be eliminated by using infrared pump wavelengths longer than 1 μm [63, 86]. The pulse-front tilt angles, required for pump–THz velocity matching, are relatively small in the mentioned semiconductors, typically below 30° [65]. Recently, the CG technology was adapted to GaP pumped at 1 μm wavelength [199], where three-photon absorption is still present, and implemented in a time-domain spectroscopy system [200]. In a contact grating (CG) based THz source, the grating structure at the entrance surface of the semiconductor crystal plate tilts the intensity front of the pump pulse. There is no need for a conventional external pulse-front-tilting arrangement [39], which consists of a transmission or reflection grating, and an imaging lens or telescope. The main advantage of the CG approach is the scalability to large sizes and pulse energies. Previous work with a GaP prism [65] and ZnTe CG [69] demonstrated the advantage of a longer pump wavelength of around 1.8 μm. However, four-photon absorption still limited the useful pump intensity at as low as 15 GW/cm^2.

• One of the goal was to experimentally investigate and characterize a scalable, highly efficient contact-grating GaP THz source pumped at an infrared wavelength which is significantly longer than previously used. In experiment and numerical simulations, I study broadband high-field THz pulse generation performance in this new regime. This enables identifying the physical limitations and exploring the performance potential of such sources under extended pumping conditions. The development of powerful mid-infrared (MIR) femtosecond sources based on optical parametric chirped-pulse amplification (OPCPA) [70–72] are ideally suited

as efficient drivers of semiconductor CG THz sources, which are free from the detrimental low-order multiphoton pump absorption.

Another popular THz source, organic nonlinear optical crystals, are very attractive for the efficient generation of strong-field THz pulses by optical rectification of femtosecond laser pulses [73, 74, 76–80, 145, 202, 205, 208, 212]. They have exceptionally large second-order nonlinear optical coefficients and can provide large bandwidths up to 20 THz [203, 208] in a simple collinear scheme. When pumped by Ti:sapphire or Yb-based lasers directly, two- and three-photon absorption can increase heat dissipation to the crystal and can produce free carriers, which increases the absorption of THz radiation and reduces the efficiency of THz generation [80]. Although nonlinear absorption is a major factor in determining the THz generation performance of organic crystals, measured values for multiphoton absorption coefficients are still missing in the literature. Knowledge of these related material data is important for the design of robust THz sources with optimal performance.

• My second goal was to measure the optical transmittance, as function of the pump fluence, in the organic THz generator crystals NMBA, BNA, and MNA at the commonly used laser wavelengths of 780 nm and 1030 nm and to give values for the relevant nonlinear optical parameters in all three materials. These values can be used to more precisely calculate nonlinear pump absorption and can be included into numerical models of THz generation and optical heating.

Chapter 4

Results

4.1 Broadband GaP contact-grating terahertz source pumped at 3.9 μm

Recently, semiconductors (GaAs [67], ZnTe and GaP [65]) emerged as promising alternative sources of intense THz fields. Detrimental low-order multiphoton pump absorption [96] can be eliminated by longer infrared pump wavelengths. The pulsefront tilt angles, required for pump-THz velocity matching, are relatively small, typically below 30°. This enabled the demonstration of a highly efficient, monolithic THz source with collinear geometry, utilizing the contact-grating (CG) technology in a ZnTe crystal slab [69]. The grating structure [39] at the entrance surface of the semiconductor crystal plate tilts the intensity front of the pump pulse. Powerful sources of mid-infrared femtosecond pulses based on optical parametric chirped-pulse amplification (OPCPA) became available recently [70–72]. They lead to the demonstration of highly efficient THz sources from two-color air plasma [52] and organic nonlinear crystals [78], and are ideally suited to drive efficiently semiconductor CG THz sources. In this work, for the first time, (i) a GaP semiconductor contact grating was realized, with an (ii) optimized trapezoidal relief profile, and (iii) broadband THz pulse generation was demonstrated with 3.9 μm mid-infrared pump wavelength.

4.1.1 GaP contact grating with trapezoidal profile

Figure 4.1(a) shows the scheme of the GaP CG THz source with trapezoidal groove profile. The optical pump beam enters, at a normal incidence, the GaP nonlinear crystal through the CG. Within the bulk of the crystal, two symmetrically propagating beams are formed [169], with diffraction angles $\pm\beta$ for diffraction orders $m = \pm 1$, respectively. For the pulse-front-tilt angle $\gamma = \beta$ holds in both diffracted beams, due to normal incidence. Because of the opposite signs of the angular dispersion in the two beams, their pulse fronts are merged (light blue shaded area in Figure 4.1(a). Consequently, a single THz beam is generated by OR, with its wavefront parallel to the pump pulse front. The generated THz beam leaves the nonlinear crystal through the backside surface, in a direction normal to the crystal surface. The collinear pumping geometry is advantageous for applications. As a semiconductor nonlinear material for OR,

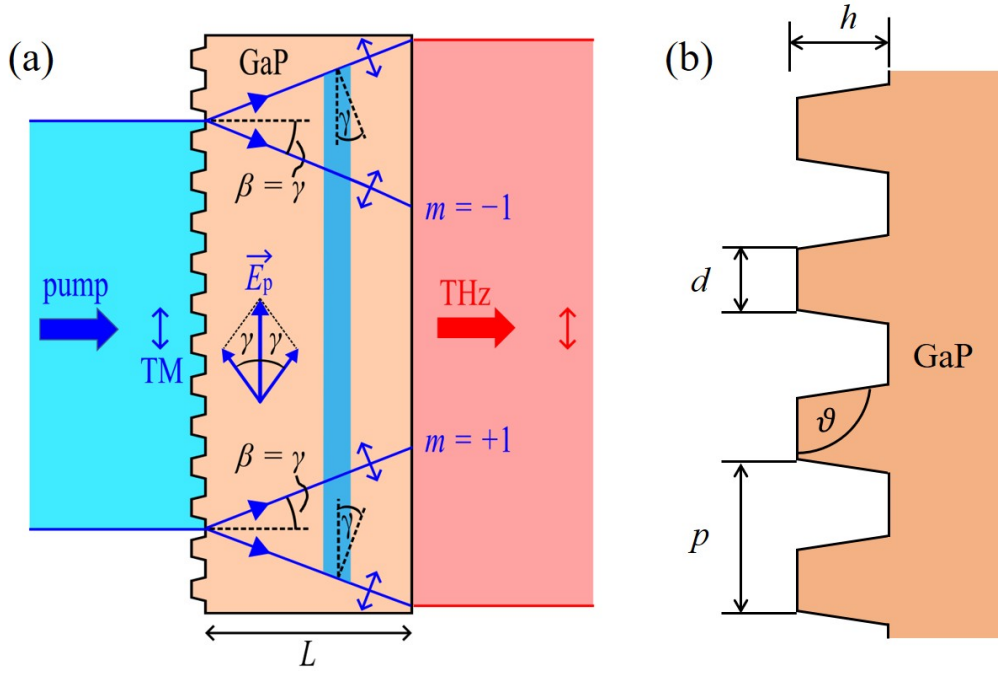

Figure 4.1: Scheme of the GaP CG THz source with trapezoidal relief profile. (a) Layout of the source and the beam geometry. Double arrows indicate the electric field polarization directions. $\vec{E}_p$ is the total electric field originating from the superposition of both diffraction orders $m = \pm 1$. (b) Definition of grating profile parameters [272].

we selected GaP (rather than the previously used ZnTe [69]) for two reasons. First, GaP is available in large sizes with high optical quality and is free of multidomain orientation. Second, GaP supports the generation of a broad THz bandwidth, due to its favorable absorption and dispersion properties in the THz range. The transverse optical (TO) phonon frequency is at 11 THz, below which the second-order nonlinear susceptibility decreases with increasing frequency and changes sign at 8 THz [186]. This feature limits the achievable gapless OR bandwidth to about 6 THz [200, 271], depending on velocity-matching conditions (see below). Furthermore, GaP has a relatively large direct bandgap of 2.79 eV, facilitating the elimination of low-order multiphoton absorption at MIR pump wavelengths.

In GaP, the highest pump-to-THz conversion efficiency can be expected near 3 THz [271], around the center of the OR bandwidth. Consequently, we designed the CG THz source for velocity matching between the optical pump and the generated THz pulse for an output frequency of 3 THz. According to the velocity-matching condition $\cos(\gamma)c/n_g(\lambda_p) = c/n(3\ \mathrm{THz})$ [100], a pulse-front-tilt angle of $\gamma \approx 25°$ is needed at the central pump wavelength $\lambda_p = 3.9\,\mu\mathrm{m}$. Here, c is the vacuum speed of light, $n(3\ \mathrm{THz})$ is the phase refractive index at the velocity-matched THz frequency in GaP, and $n_g(\lambda_p)$ is the group index at the pump wavelength in GaP [273]. The grating period of $p = 3026$ nm, which produces the required pulse-front-tilt angle inside the GaP material, can be calculated from the grating equation $n(\lambda_p)\,\sin(\beta) = \pm\lambda_p/p$ [274], with the diffraction angle $\beta = \pm\gamma$. The CG structure was formed on the front surface of a (110)-cut GaP single-crystal plate, with the grating lines aligned at $\pi/2 - \varphi = 35.3°$ to the Z-axis of the crystal (Figure 4.2a)). The angle between the TM polarized pump electric

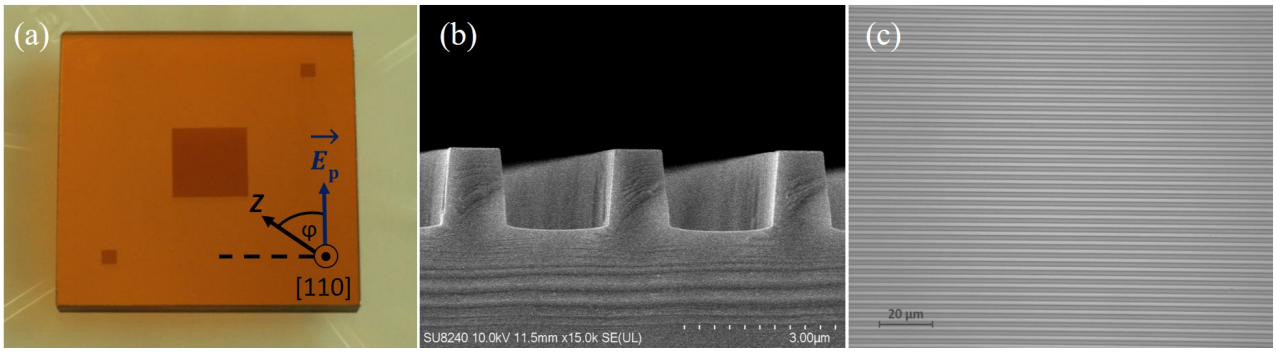

Figure 4.2: The broadband GaP CG THz source. (a) Photograph of the THz source. The rectangular dark orange area in the center is the CG patterned area. The horizontal black dashed line indicates the direction of the grating lines, the [110]-axis points out of the plane of the picture, $\varphi = 54.7°$ is the angle between the Z- or [001]-axis of the crystal and the polarization direction of the pump electric field $\vec{E}_{\mathrm{p}}$ (vertical blue arrow). (b) Scanning electron microscope (SEM) micrograph of a cleaved test sample showing the cross section of the grating profile. (c) Top-down SEM image of the grating surface [272].

field and the Z-axis was $\varphi = 54.7°$, maximizing the effective nonlinear coefficient for OR [69]. The residual local electric field is the superposition of the local electric fields originating from the two diffraction orders $m = \pm 1$ (see $\vec{E}_{\mathrm{p}}$ in Figure 4.1(a)). Due to a noncollinearity angle of 2γ between the two TM-polarized field contributions, the residual electric field is reduced and its direction varies between $\pm\gamma$ through the beam cross section. This effect reduces somewhat the effective nonlinear coefficient. The grating, limited in size by the available patterning capability, covered the central 7×7 mm^2 surface area of the 30×30 mm^2 sized GaP substrate (Figure 4.2(a)). A substrate thickness of $L = 4$ mm was a trade-off between increasing the interaction length for THz generation and decreasing the overlap between the $m = \pm 1$ diffraction orders due to lateral walk-off (Figure 4.1(a)).

Figure 4.3 shows the calculated THz generation efficiency as a function of the GaP crystal thickness for a pump intensity of 160 GW/cm^2. For this calculation, we used the same optical-rectification model as described in Section 4.1.5. Similar results were shown at a shorter MIR wavelength of 1.7 μm, related to the proper choice of the crystal length [275]. According to our calculation, the efficiency goes to saturation at crystal thicknesses exceeding about 4 mm. To achieve a relatively high efficiency without saturation, we chose 4 mm for the GaP crystal thickness of the CG THz source. Electron beam microlithography and dry (plasma) etching were used to produce the surface-relief grating profile (Kelvin Nanotechnology Ltd., UK). Before live sample manufacturing, test samples were produced in a process capability study to determine the achievable sidewall angle (ϑ) of the line profile (Figure 4.1(b)). Scanning electron microscope micrograph of a cleaved test sample showed a trapezoidal line profile (Figure 4.2(b)), with a sidewall angle of $\vartheta \approx 95°$. For the live sample, the ridge width at the top of the structure, $d = 1362\ (+151/-242)$ nm, and the profile depth, $h = 1325\ (+75/-99)$ nm (Figure 4.1(b)), were optimized for the maximum useful diffraction efficiency for TM polarization. This efficiency is higher in TM mode than in TE mode. Consequently, for the given grating period of $p = 3026$ nm, the optimal filling

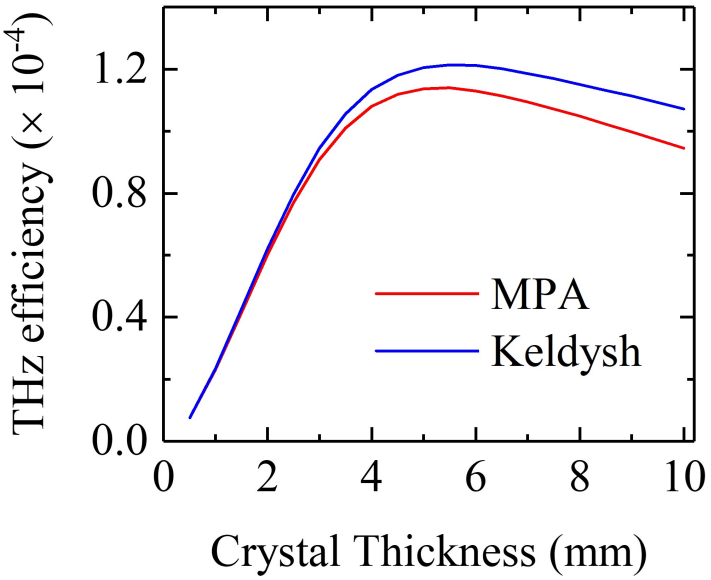

Figure 4.3: Calculated THz generation efficiency as a function of the GaP crystal thickness for a pump intensity of 160 GW/cm^2 using MPA (red line) and Keldysh models (blue line) for free-carrier generation [272].

factor is 45%. According to calculation [276], the maximum combined diffraction efficiency of the two symmetrically propagating orders $m = \pm 1$ is 78%. The tolerances for d and h allow for 2% efficiency drop below the maximum. The profile shape of the live sample was within the tolerances and the line pattern was highly uniform over the entire processed surface (Figure 4.2(c)).

4.1.2 Experimental setup

A high-peak-power MIR OPCPA system [71], operating at 20 Hz repetition rate, pumped the GaP CG THz source. Figure 4.4 shows the schematic of the OPCPA system and the experimental arrangement. We characterized the temporal and spectral structure of the pump pulses by second-harmonic FROG measurements, retrieving a pulse duration of τ_p = 110 fs (full width at half maximum of the intensity) and a central wavelength of λ_p = 3.9 μm. The pump beam diameter at the GaP CG THz source was $2w_\mathrm{p}$ = 6.9 mm (full width at 1/e^2 level of the peak intensity). For THz generation, to avoid damage to the CG device, we used a maximum pump pulse energy of W_p = 15 mJ, corresponding to an average pump fluence of $F_\mathrm{p} = W_\mathrm{p}/(\pi w_\mathrm{p}^2)$ = 40 mJ/cm^2, and an average intensity of $I_\mathrm{p} = F_\mathrm{p}/(\sqrt{2\ln 2}\tau_\mathrm{p})$ = 310 GW/cm^2. The peak intensity [277] at the center of the beam and pulse was $I_0 = 4\sqrt{\ln 2/\pi} I_\mathrm{p}$ = 1.88 I_p = 583 GW/cm^2.

The generated THz beam propagated parallel to the incident pump beam and left the GaP crystal through its back surface (Figure 4.1(a)). A long-pass filter (Tydex, model LPF 21.4) transmitted only the THz radiation and blocked the MIR pump light. The THz beam was steered to a calibrated pyroelectric detector (Gentec, model THZ5I-BL-BNC) to measure the pulse energy, and to an electro-optic sampling (EOS) unit to record the THz waveform (Figure 4.6). For details on the calibration of the THz pulse energy measurement using

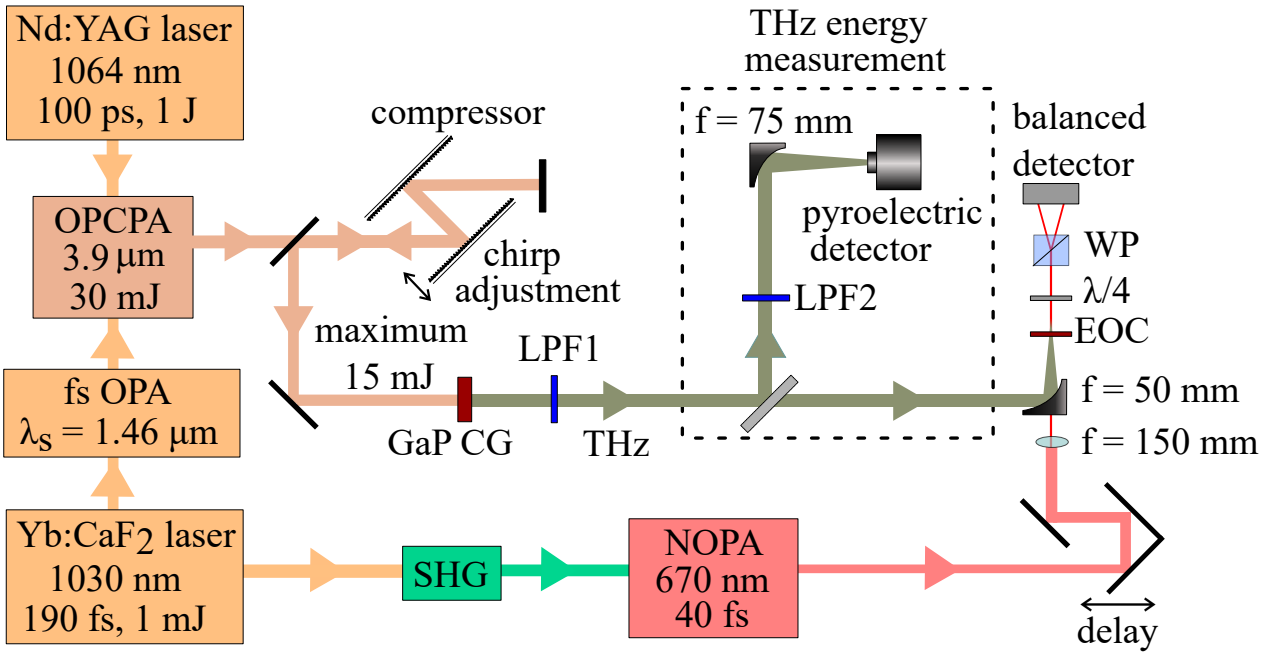

Figure 4.4: Scheme of the experimental setup. OP(CP)A: optical parametric (chirped-pulse) amplifier, NOPA: noncollinear OPA, SHG: second-harmonic generation, LPF: long-pass filter, EOC: electro-optic crystal, $\lambda/4$: quarter-wave retardation plate, WP: Wollaston prism [272].

the pyroelectric detector, see the Supplementary information for Ref. [52]. Because the pyroelectric detector was very sensitive to the MIR pump wavelength, we inserted a wire-grid filter with a cutoff frequency of 9 THz (Swiss Terahertz, LLC) as a second long-pass filter in front of the detector. For EOS, we used a sandwiched GaP crystal, composed of a 50 μm thick (110)-oriented GaP plate as the active layer and a 2 mm thick inactive GaP substrate to delay reflected pulses for a larger reflection-free time window. An off-axis parabolic mirror of 50 mm reflected focal length focused the THz pulses into the GaP crystal. A home-built, white-light-seeded, noncollinear optical parametric amplifier, based on a BBO crystal with type-I phase matching, produced synchronized sampling pulses for EOS (Figure 4.4). The sampling pulses were compressed to 40 fs; their central wavelength was 670 nm. A lens of 150 mm focal length focused the sampling pulses through a center hole in the off-axis parabolic mirror to overlap with the focused THz pulses in the GaP crystal. We measured the THz-field-induced change in the polarization state of the sampling pulses by conventional balanced detection [14].

4.1.3 THz generation results

Figure 4.5(a) shows the measured THz pulse energy as a function of the average pump fluence. At low fluences up to about 17 mJ/cm^2, the THz energy increased quadratically with increasing fluence, which corresponds to a linear increase in efficiency (Figure 4.5(b)). The characteristics changed abruptly to a saturation regime, extending from about 20 mJ/cm^2 to 30 mJ/cm^2 pump fluence, with nearly linear energy scaling and approximately constant efficiency. Above 30 mJ/cm^2, the efficiency started to drop. At the highest pump fluence of

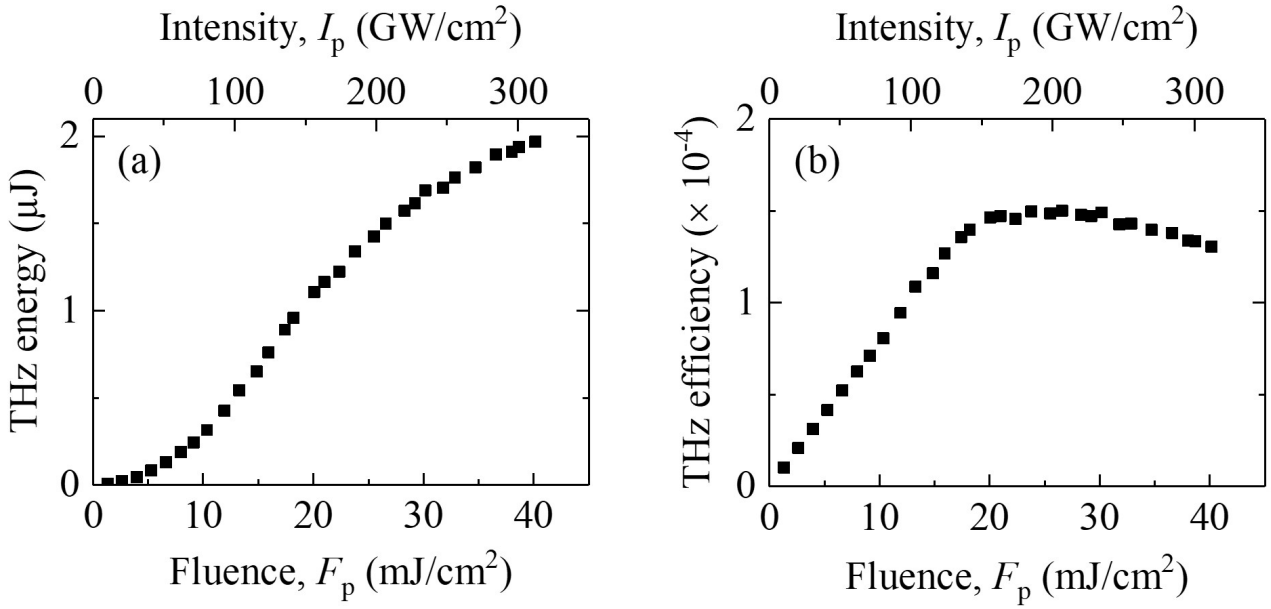

Figure 4.5: Measured THz pulse energy (a) and pump-to-THz energy conversion efficiency (b), as functions of the pump fluence and intensity [272].

40 mJ/cm^2, we observed a THz pulse energy of 2 μJ. Because the diffraction orders $|m| > 0$ undergo total internal reflection and do not leave the CG directly through the back surface, it is mainly the order $m = 0$ that is partially transmitted. According to calculation, about 21% of the incident pump pulse energy goes into this order, of which $\mathrm{e}^{-\alpha L}$ = 41% is transmitted through the bulk of GaP and of this $4n/(n+1)^2$ = 75% through the back surface. Here, $n(\lambda_\mathrm{p})$ = 3.014 is the refractive index and $\alpha(\lambda_\mathrm{p})$ = 2.2 cm^{-1} is the linear absorption coefficient of GaP at 3.9 μm wavelength. Together, about 6.5% of the incident pump pulse energy is expected to be transmitted through the CG slab. In comparison, at low pump intensity, we measured a somewhat higher 10% transmittance. This indicates that the diffraction efficiency of the usable $m = \pm 1$ diffraction orders could be slightly lower than the expectation but close to it within a few percent, allowing efficient coupling of pump energy into the GaP crystal.

The prechirp affects the evolution of the pump pulse duration and the pump intensity with propagation distance within the GaP material [63]. By adjusting the compressor grating separation (Figure 4.4), we set a positive prechirp of the incident pump pulse to yield the highest THz pulse energy at 26 mJ/cm^2 pump fluence, near the highest efficiency (Figure 4.5(b)). The measurements presented in Figures 4.5 and 4.6 used this setting. The positive prechirp partially compensated for the negative dispersion arising from the angular dispersion of the CG [278].

Figure 4.6 shows THz pulse waveforms, measured at pump fluences of 13 mJ/cm^2 and 40 mJ/cm^2, and the corresponding amplitude spectra both on linear and logarithmic scales, calculated by Fourier transformation of the waveforms. The two selected fluences represent different regimes of THz generation: quadratic energy scaling and strong saturation, respectively (Figure 4.5). Both waveforms had similar, nearly single-cycle shapes with similar spectra, demonstrating the robustness of the source for practical applications. For both pump fluences,

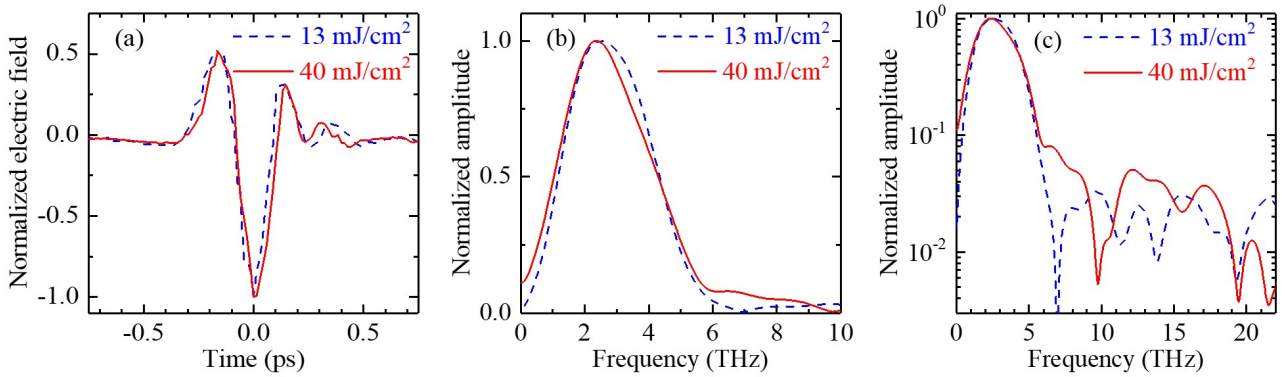

Figure 4.6: (a) Temporal waveforms of the THz pulses measured by EOS at pump fluences of 13 mJ/cm^2 (blue dashed line) and 40 mJ/cm^2 (red solid line). (b) Amplitude spectra of THz pulses, obtained by Fourier transformation of the waveforms in (a), shown on a linear scale for the amplitude. (c) The same amplitude spectra as in (b), shown on a logarithmic scale for the amplitude and in a broader frequency range [272].

the maximum spectral amplitude was at a frequency of about 2.3 THz. In agreement with expectation (Section 4.1.1), the pulse bandwidth was 6 THz, corresponding to a width at 10% of the maximum amplitude, about three times that of popular $LiNbO_3$-based sources. In case of 40 mJ/cm^2 pump fluence, a high-frequency shoulder is clearly visible in the amplitude spectrum (Figure 4.6(c)), which extends to almost 20 THz. The possible reason for this spectral feature can be a nonlinear spectral broadening of the THz pulses. These results demonstrate a scalable monolithic THz source with nearly-single-cycle waveform and a broad bandwidth of 6 THz. Due to the large bandwidth and the scalable size, the THz source has the potential to deliver high field strengths. Assuming a THz spot size at the CG output similar to the pump spot size $2w_\mathrm{p}$ = 6.9 mm, in the focus of the off-axis parabolic mirror with f = 50 mm effective focal length, we estimate a THz focal spot size of $2w_0 \approx 2\lambda_\mathrm{THz} f/(\pi w_\mathrm{p})$ = 1.2 mm. Here, λ_THz = 130 μm is the wavelength corresponding to 2.3 THz, the frequency at which the measured amplitude spectrum reached its maximum (Figure 4.6(b)). From this focal spot size, the measured waveform, and the maximum measured THz pulse energy of 2 μJ, we estimate a peak electric field of about 1 MV/cm.

4.1.4 Simulation model

Free-carrier absorption (FCA)

If a semiconductor, such as GaP, is exposed to intense light, electrons can be excited from the valence to the conduction band, thereby increasing the density of free carriers (electrons and holes). Electrons in the conduction band further absorb the incident radiation and transition to a higher energy state within the band. Likewise, the promoted holes in the heavy-hole band can also be excited to a higher energy state. Consequently, free-carrier absorption is proportional to carrier densities. The densities of charge carriers depend nonlinearly on the incident intensities, while their generation rate is influenced by the order of multiphoton

absorption involved. The increase in free-carrier concentration contribute to the complex dielectric function of the material, both at optical as well as at THz frequencies, thereby limiting the pump intensity available for THz generation. In this work, we used two different models, Multiphoton absorption and Keldysh model to estimate the free-carrier concentration generated by the mid-infrared optical pump in GaP, as described below. Subsequently, we used a Drude model, to calculate the intensity-dependent absorption at optical and THz frequencies from the free-carrier concentrations.

Multiphoton absorption model

In semiconductors, absorption of light can lead to the excitation of electrons from the valence band to the conduction band. Linear electronic absorption in dielectric materials or semiconductors can only take place if the energy of the photon exceeds the band gap energy. Nevertheless, it is feasible to bridge that bandgap at elevated optical intensity through the simultaneous absorption of two or more photons with lower energy, where the total energy of the photons surpasses the bandgap energy. These nonlinear absorption phenomena are referred to as multiphoton absorption (MPA) [279–282], and result in losses, which restricts the efficiency of nonlinear optical materials. The most basic form of MPA is two-photon absorption. The intensity- dependent absorption coefficient, $\alpha(I)$, describes how a material's transparency changes as the incident pump pulse intensity (I) increases. This behavior is mathematically represented by the Taylor series expansion in terms of intensity [283]

$$\alpha(I) = \alpha_0 + \beta_2 I + \beta_3 I^2 + \beta_4 I^3 + \ ..., \tag{4.1}$$

where α_0 is the linear absorption coefficient, β_2, β_3, and β_4 are the two-, three-, and four-photon absorption coefficients, respectively. The density of free carriers (N_{fc}) generated by the incident pump pulse can be estimated by [63, 96]

$$N_{\mathrm{fc}} = \frac{I\tau}{hc/\lambda_0}\left(\alpha_0 + \frac{1}{2}\beta_2 I + \frac{1}{3}\beta_3 I^2 + \frac{1}{4}\beta_4 I^3 + \ ...\right), \tag{4.2}$$

where τ is the pulse duration, h is the Planck constant, c is the speed of light, and and λ_0 is the central pump wavelength.

Keldysh model of photoionization

The Keldysh model [284] describes the ionization of atoms in a strong laser field. It includes, as special cases, multiphoton and tunneling ionization regimes. The Keldysh parameter (γ, quantifies the transition between multiphoton ionization ($\gamma \gg 1$) and tunneling ionization ($\gamma \ll 1$). The model provides an analytical formula for the ionization rate and shows how it transits from a multiphoton to a tunneling process as the laser intensity increases. Figure 4.7 shows the photoionization rate, including multiphoton, tunneling, and full Keldysh photoionization, in GaP (using direct bandgap of 2.78 eV), as a function of laser intensity for a wavelength of 3.9 μm, and 100 fs pulse duration. The corresponding Keldysh parameter is also plotted against intensity. The full excitation rate per unit volume, W_{full}, is calculated using the Keldysh expression [285–288],

$$W_{\text{full}} = 2 \cdot \frac{2\,\omega}{9\pi} \left(\frac{\sqrt{(1+\gamma^2)}}{\gamma} \frac{m_{\text{eff}}\,\omega}{\hbar} \right)^{3/2} Q\left(\gamma, \frac{E_{\text{g}}^*}{\hbar\,\omega_0}\right) \times \exp\left(-\pi \frac{E_{\text{g}}^*}{\hbar\,\omega_0} + 1\right) \times \left[K\left(\frac{\gamma^2}{1+\gamma^2}\right) - E\left(\frac{\gamma^2}{1+\gamma^2}\right) / E\left(\frac{1}{1+\gamma^2}\right) \right], \tag{4.3}$$

with the function Q defined as:

$$Q(x) = \left[\pi/2K\left(\frac{1}{1+\gamma^2}\right) \right]^{1/2} \times \sum_{n=-\infty}^{\infty} \exp\left(-\left(\left(\frac{x^2}{1+\gamma^2} \right) - E \right) \left(\frac{x^2}{1+\gamma^2} \right)^{n/E} \left(\frac{1}{1+\gamma^2} \right) \right) \times \phi\left(\left[2\,(x+1) - 2x + \ln(2\pi) \left(\frac{1}{1+\gamma^2} \right) \right] E\left(\frac{1}{1+\gamma^2} \right) \left(\frac{1}{1+\gamma^2} \right)^{1/2} \right). \tag{4.4}$$

The variable E_{g}^* takes a new form in the full rate equation. The effective band-gap, E_{g}^*, becomes:

$$E_{\text{g}}^* = \frac{2}{\pi} E_{\text{g}} \frac{\sqrt{1\,+\,\gamma^2}}{\gamma} E\left(\frac{1}{1\,+\,\gamma^2} \right). \tag{4.5}$$

K and E are complete elliptic integrals of the first and second kind. These elliptic integrals are handled by the tool *ellipke* in MATLAB [289]. The Dawson integral is given by $\phi(x) = \int_0^x \exp(\xi^2 - x^2)\,d\xi$ [285]. To calculate the free-carrier electron density, the full ionization rate is integrated in a time interval $\pm T$ over which the pulse is defined and is given by $N_{\text{fc}} = \int_{-T}^{T} W_{\text{full}} \mathrm{d}t$.

Drude model

The Drude model is a semiclassical theory used to describe free-carrier absorption (FCA) in metals and doped semiconductors. It treats free carriers (electrons or holes) as a gas of independent classical particles that oscillate in response to an electromagnetic field, with their motion limited by collisions with the lattice. In the Drude model, the free-carrier contribution to the dielectric function of a semiconductor is given by the following expression [290]:

$$\epsilon_{\text{fc}}(\Omega) = -\frac{\epsilon_\infty \Omega_{\text{p}}^2}{\Omega^2 + i\Omega/\tau_{\text{sc}}}, \tag{4.6}$$

where ϵ_∞ is the high-frequency dielectric constant, Ω_{p} is the plasma frequency, Ω is the optical or THz angular frequency, and τ_{sc} is the electron scattering time. Here $\Omega_{\text{p}}^2 = e^2 N_{\text{fc}}/(\epsilon_0 \epsilon_\infty m_{\text{eff}})$, e is the electron charge, N_{fc} is the free-carrier density, ϵ_0 is the free space permittivity, and m_{eff} is the effective electron-hole mass.

The dielectric function of an optically driven semiconductor is given by the sum of the material's

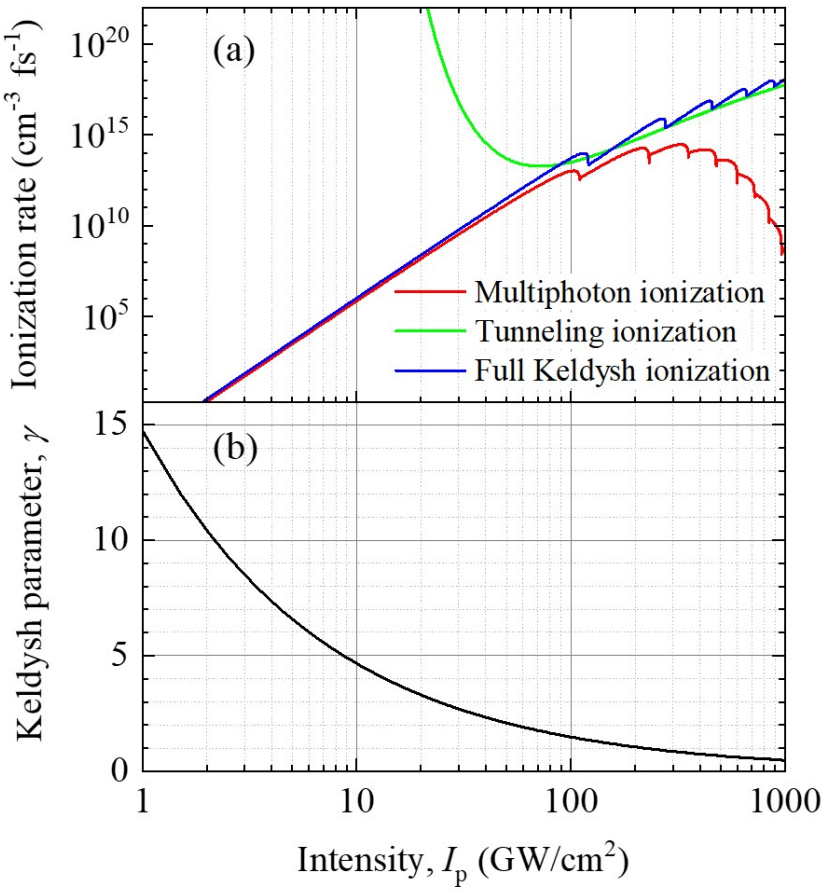

Figure 4.7: (a) Photoionization rate as function of laser intensity. The red line represents the multiphoton ionization rate, the green line the tunneling ionization rate, and the blue line the full ionization rate. (b) Keldysh parameter as function of laser intensity [272].

dielectric function $\epsilon_{\mathrm{mat}}(\Omega)$, describing its linear response, and the free-carrier contribution $\epsilon_{\mathrm{fc}}(\Omega)$:

$$\epsilon(\Omega) = \epsilon_{\mathrm{mat}}(\Omega) + \epsilon_{\mathrm{fc}}(\Omega). \tag{4.7}$$

The absorption coefficient $\alpha(\Omega)$, and the refractive index $n(\Omega)$ of the optically driven semiconductor can be calculated from the dielectric function as

$$\begin{aligned} \alpha(\Omega) &= \frac{2\Omega}{c} \cdot \mathrm{Im}\left[\sqrt{\epsilon(\Omega)}\right], \\ n(\Omega) &= \mathrm{Re}\left[\sqrt{\epsilon(\Omega)}\right]. \end{aligned} \tag{4.8}$$

Spatial averaging for THz generation efficiency

To give a more realistic estimation of the pump-to-THz energy conversion efficiency,

$$\overline{\eta} = \frac{W_{\mathrm{THz}}}{W_{\mathrm{p}}}, \tag{4.9}$$

as a function of the average pump fluence Figure 4.5 , we improved the one-dimensional optical-rectification model (including FCA) by a spatial averaging over the pump and THz beam cross sections. Here, W_{THz} and W_{p} are the pump and the THz pulse energies, respectively. For simplicity, we assumed radial symmetry for both the incoming pump and the outgoing THz beams, and a Gaussian fluence distribution for the incoming pump,

$$F_{\mathrm{p}}(r) = F_{\mathrm{p},0}\ \mathrm{e}^{-r^2/w_{\mathrm{p}}^2}. \tag{4.10}$$

Here, r is the radial beam coordinate and $F_{\mathrm{p},0}$ is the pump fluence at the beam center. We used the one-dimensional model to calculate the local pump-to-THz energy conversion efficiency,

$$\eta(r) = \frac{F_{\mathrm{THz}}(r)}{F_{\mathrm{p}}(r)}. \tag{4.11}$$

Integration of the pump and THz local fluences over the respective beam cross sections gives the pulse energies:

$$\begin{aligned} W_{\mathrm{p}} &= 2\pi \int_0^\infty \mathrm{d}r\ r\ F_{\mathrm{p}}(r), \\ W_{\mathrm{THz}} &= 2\pi \int_0^\infty \mathrm{d}r\ r\ F_{\mathrm{THz}}(r) \\ &= 2\pi \int_0^\infty \mathrm{d}r\ r\ \eta(r)\ F_{\mathrm{p}}(r), \end{aligned} \tag{4.12}$$

where $\eta(r) = \eta\left(F_{\mathrm{p}}(r)\right)$. Substituting Equation 4.12 into Equation 4.9 results in the following expression for the energy conversion efficiency, as a function of the (peak or average) pump fluence:

$$\overline{\eta}\left(F_{\mathrm{p},0}\right) = \frac{2}{w^2} \int_0^\infty \mathrm{d}r\ r\ \mathrm{e}^{-r^2/w_{\mathrm{p}}^2}\ \eta\left(F_{\mathrm{p},0}\ \mathrm{e}^{-r^2/w_{\mathrm{p}}^2}\right). \tag{4.13}$$

Thus, $\overline{\eta}\left(F_{\mathrm{p},0}\right)$ is a weighted integral of all (local) efficiency values η, which correspond to pump fluences smaller than $F_{\mathrm{p},0}$.

This simple spatial averaging procedure significantly improved the agreement between measured and calculated THz generation efficiencies, as functions of the pump fluence. A more accurate calculation requires a 3-dimensional model, but this is beyond the scope of the present work. In such a model, the varying interaction length for THz generation in the plane of the pulse-front tilt and the interference between the $m = \pm 1$ diffraction orders also need to be taken into account [169]. Furthermore, because of the sudden steep increase in the intensity-dependent absorption at the pump wavelength (Figure 4.9), a similar averaging procedure makes only a small difference, and we do not discuss it here in detail.

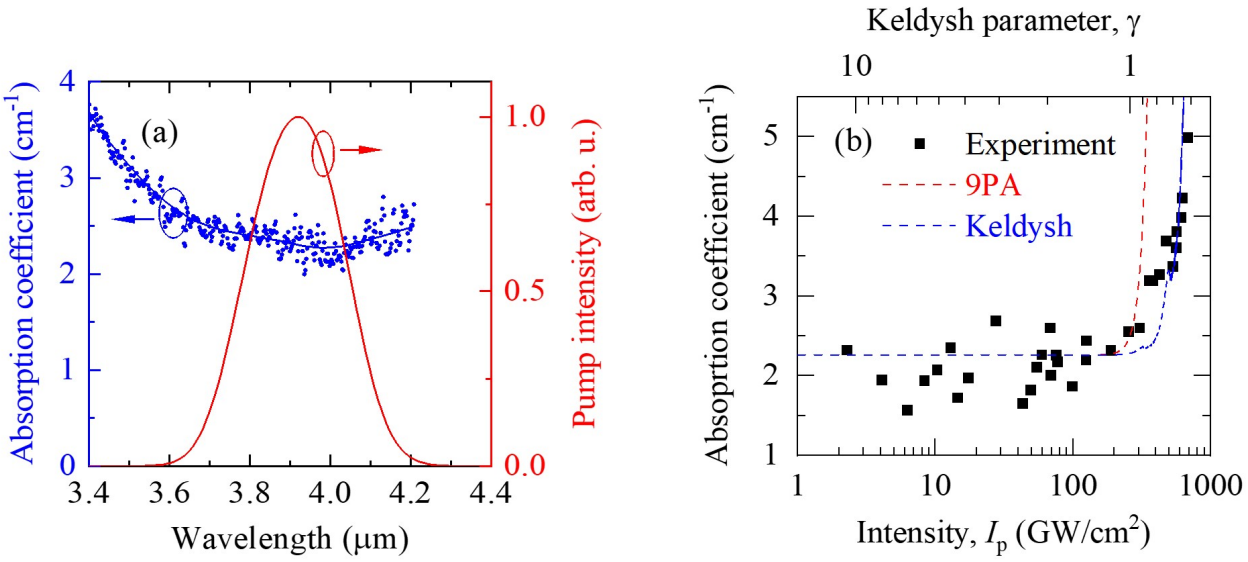

Figure 4.8: (a) MIR absorption coefficient of the GaP crystal as a function of the wavelength (blue symbols), measured in the range of linear absorption by the ultrabroadband MIR laser system at ELI ALPS [291] at a low power of 0.14 GW/cm^2, using a spectrometer (Fastlite, model Mozza). The blue solid line shows the smoothed data. The red solid line shows the normalized spectrum of the 3.9 μm pump pulses used for THz generation, as retrieved from FROG measurement. (b) Spectrally averaged absorption coefficient of the GaP crystal as a function of the 3.9 μm pump intensity: measured (black symbols), calculated by the multiphoton model (red dashed line), and by the Keldysh model (blue dashed line) [272].

4.1.5 Discussion

Multiphoton absorption (MPA) at the pump wavelength, along with the resulting increase in free-carrier absorption, is the primary cause of THz generation efficiency saturation in semiconductors pumped at near-infrared wavelengths (see e.g. Ref. [188]). Using a longer pump wavelength eliminated two-photon absorption in GaAs [67] and two- and three-photon absorption in ZnTe [65, 69], thus leading to a dramatic increase in the THz generation efficiency. However, in ZnTe pumped at 1.8 μm, four-photon absorption still limited the useful pump intensity to only 14 GW/cm^2 in a bulk crystal [65] and 8 GW/cm^2 in a CG source [69]. The reason for the lower maximum useful pump intensity in case of the CG was the two times higher peak intensity due to interference of the overlapping $m = \pm 1$ diffraction orders [275]. In GaP pumped at a wavelength of 1.03 μm, saturation of THz generation efficiency occurred at a pump intensity of only 2 GW/cm^2 due to three-photon absorption [96]. In another case, pumped at 1.7 μm and limited by four-photon absorption, saturation occurred at 6 GW/cm^2 intensity [65]. In contrast to the latter case, our experiment applied more than two times longer pump wavelength of 3.9 μm (Figure 4.8(a)), and saturation of THz generation efficiency occurred at a 27-times higher pump intensity of about 160 GW/cm^2 (Figure 4.5(b)). This observation is consistent with a limitation of the THz generation efficiency by MPA of a much higher order. Indeed, due to the small MIR photon energies, the lowest effective order of MPA in GaP is nine-photon (ten-photon) absorption below (above) about 4 μm wavelength.

To investigate the saturation of THz generation, we performed numerical calculations with an optical-rectification model, complemented by free-carrier absorption (FCA) [63, 271, 275]. The model took into account the variation of the pump pulse duration and intensity due to material and angular dispersions, as well as linear absorption and pump-induced free-carrier absorption in the THz range. As the physical origin of the pump-induced increase in free-carrier concentration, we first assumed MPA and calculated the corresponding FCA from the Drude model [271, 275, 290]. The model took into account 9PA, the lowest effective order of MPA, and neglected higher-order effects in lack of independently measured values for their coefficients. For comparison and further analysis, we also used the more general Keldysh model [284] to calculate the free-carrier concentration (see Section 4.1.4). To estimate the effective 9PA coefficient $\beta_{9\mathrm{PA}}$ in GaP at 3.9 μm wavelength, we measured the intensity-dependent transmittance of a 1 mm thick test sample that had no grating on its surface. This sample was cut from the same GaP crystal boule as the CG substrate.

From the measured transmittance, also accounting for the reflection loss at the crystal surfaces [273], we calculated the intensity-dependent absorption coefficient (Figure 4.8(b)). The absorption coefficient maintained its low-intensity value of 2.2 cm^{-1} up to about 200 GW/cm^2 intensity, but above this pump level, it increased rapidly up to 5 cm^{-1} at 700 GW/cm^2. Using a 9PA coefficient as a fit parameter, the FCA model with $\beta_{9\mathrm{PA}} = (1.0 + 1.0/-0.5) \times 10^{-22}$ cm^{15}/GW^8 reproduced well the observed onset of nonlinear absorption (Figure 4.8(b)). In the model for THz generation, we used this value. With the value obtained for the 9PA coefficient, using the optical-rectification model combined with pump-induced FCA, we calculated the THz generation efficiency as a function of pump intensity (red dashed line in Figure 4.9). The calculation reproduced the observed linear increase of the efficiency. In this range, extending up to a pump of about 140 GW/cm^2, free-carrier generation effects are negligible. The calculation also reproduces the observed onset of saturation of THz generation around the mentioned pump intensity, which is due to the steep increase of FCA caused by 9PA. However, in contrast to experimental observations, the calculation predicts a rapid drop in efficiency beyond its maximum.

The measurement of the pump-to-THz energy conversion efficiency is based on measuring pump and THz pulse energies with detectors integrating over the entire beam cross sections. However, because of the very high order of nonlinearity of 9PA, free-carrier generation and the (local) THz generation efficiency with its saturation can vary significantly across the beam. To obtain a more realistic picture of the THz generation process, we complemented the simulation model with spatial averaging, assuming a Gaussian pump beam intensity distribution (see Section 4.1.4). The averaging had little effect at intensities below about 140 GW/cm^2, where the THz generation efficiency scaled linearly with pump intensity (red solid line in Figure 4.9). However, at higher intensities, in the saturation regime, the efficiency calculated with spatial averaging decreases much weaker with increasing intensity than without averaging. This behavior reproduced the experimental observation much better and shows that spatial averaging is a necessary step. A general theory of photoionization was developed by Keldysh [284], who provided an expression for the number of electron-hole pairs generated in a semiconductor by an applied strong electric field. Different interaction regimes are distinguished by the Keldysh parameter $\gamma = \omega\sqrt{mE_\mathrm{g}}/(e\vec{E}_\mathrm{p})$. Here, ω is the laser angular

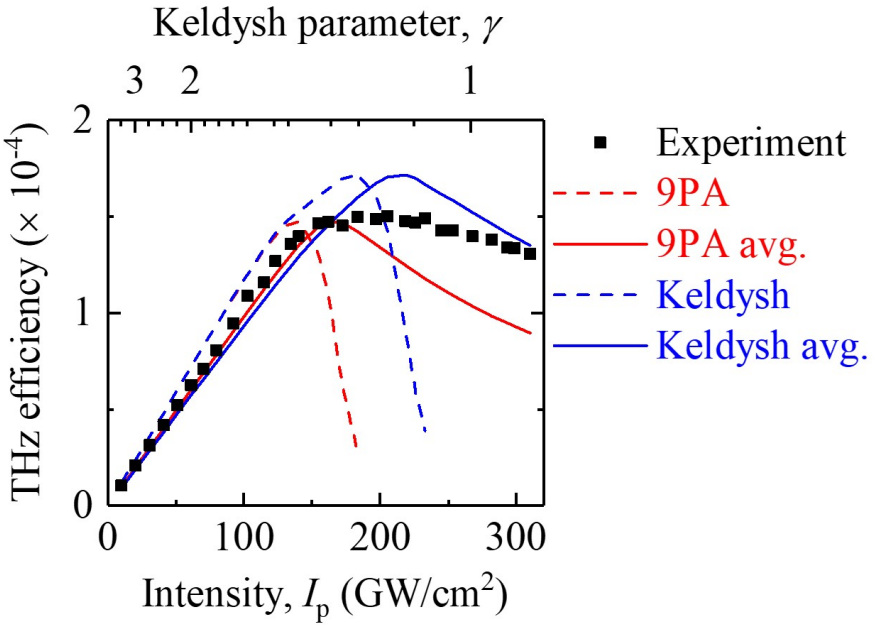

Figure 4.9: THz generation efficiencies calculated with a 9PA (red lines) and a Keldysh (blue lines) model of photoionization, without (dashed lines) and with (solid lines) averaging over the beam cross section [272]. Black symbols show the same experimental data as in Figure 4.5(b)).

frequency, $m_{\text{eff}} = (m_{\text{n}}^* m_{\text{p}}^*)/(m_{\text{n}}^* + m_{\text{p}}^*)$ is the effective electron-hole mass, where m_{n}^* and m_{p}^* are the effective masses of an electron and hole, E_{g} is the bandgap energy of the material, e is the elementary charge, and $\vec{E}_{\text{p}} = \sqrt{2I_0/cn\epsilon_0}$ is the laser electric field, with the laser intensity I_0, vacuum speed of light c, refractive index n at the laser wavelength, and free-space permittivity ϵ_0. The Keldysh model describes ionization by MPA at a low-intensity and high-frequency limit, where $\gamma \gg 1$. In our experiment, due to relatively low MIR frequencies, $\gamma \approx 1$ in the saturation regime of THz generation (Figure 4.9), which is in the transition regime between multiphoton ionization and tunnel ionization. Therefore, in a second series of calculations, we replaced the simple MPA model and applied the general Keldysh theory to calculate the transfer rate of the electrons from the valence band into the conduction band [285–288] (see Section 4.1.4). The material parameters used for the calculations were the effective electron-hole mass in GaP, $m_{\text{eff}} = 0.27\ m_{\text{e}}$ [292], and the direct bandgap energy, $E_{\text{g}} = 2.79$ eV. Here, m_{e} is the free electron rest mass. The calculation based on the Keldysh model gave a similar steep increase of the absorption coefficient with increasing pump intensity as the 9PA-based calculation, with the onset of FCA at a slightly higher intensity (blue dashed line in Figure 4.8(b)). Similarly, the saturation of the THz generation efficiency occurred at a slightly higher intensity of about 180 GW/cm^2 in the calculation based on the Keldysh model, with a similar rapid drop at still higher intensities (blue dashed line in Figure 4.9). Averaging over the beam cross section resulted in a significant improvement in reproducing the experimental data (blue solid line in Figure 4.9).

In the infrared range, GaP is transparent up to about 11 μm [135] and pump-THz velocity matching is feasible using CG technology. Increasing the pump wavelength beyond 3.9 μm

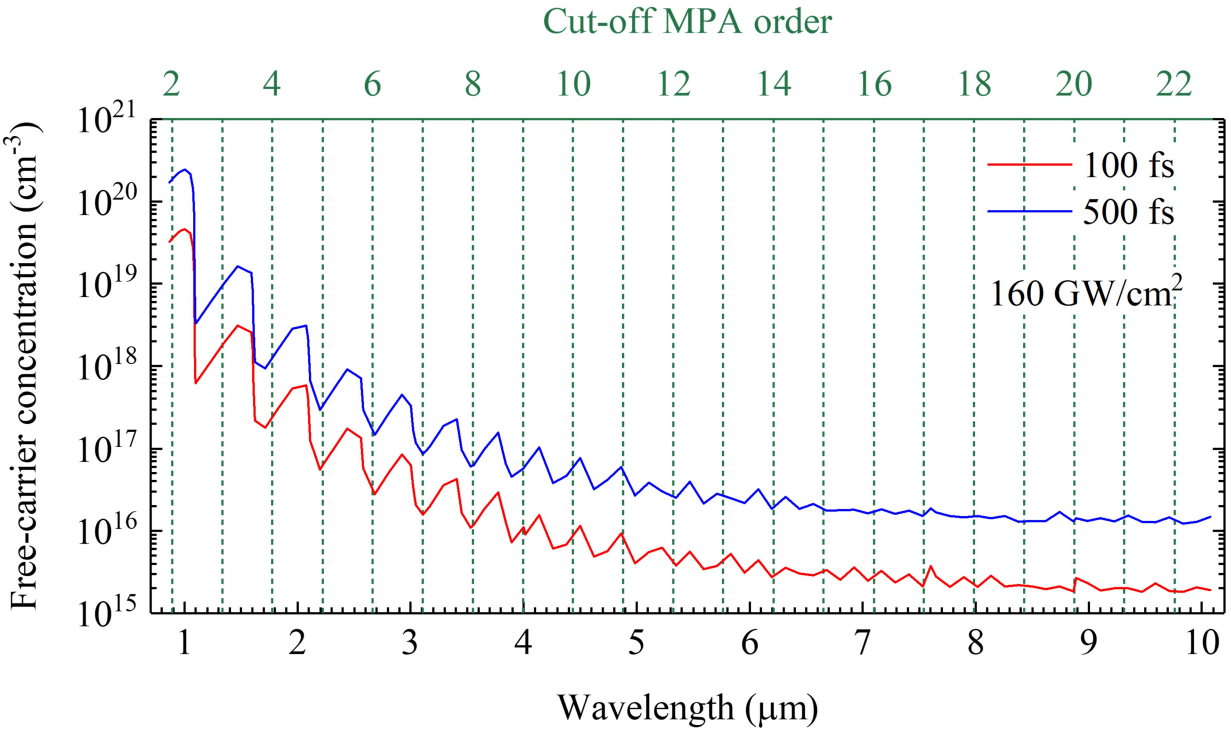

Figure 4.10: Concentration of free carriers generated by optical pumping, as a function of the pump wavelength, calculated using the Keldysh model with a pump intensity of 160 GW/cm^2 and two different pulse durations of 100 fs and 500 fs [272].

can advantageously eliminate MPA of still higher order (9PA and beyond). However, the benefit of a smaller free-carrier concentration (at a given pump intensity, see Figure 4.10), or a higher useful pump intensity (generating a given amount of free carriers) reduces at longer wavelengths. Assessing the efficiency of THz generation at such longer pump wavelengths requires knowledge of material nonlinearity parameters that are not available to us currently. The proof-of-concept experiments reported here used an OPCPA pump source. Substantially higher wall-plug to THz efficiencies are expected by driving THz generation with lasers based on transition-metal doped chalcogenide laser crystals, which can produce pulses in a similar MIR wavelength range [293–295].

4.1.6 Conclusions

A novel GaP contact grating THz source with a trapezoidal line profile was demonstrated, pumped at a mid-infrared wavelength of 3.9 μm. The source generated nearly-single-cycle waveforms with a broad bandwidth of 6 THz. Due to the long pump wavelength, the lowest-order effective multiphoton absorption was 9-photon absorption, which enabled exceptionally high useful pump intensities up to 310 GW/cm^2. The THz generation efficiency saturated at a pump intensity of about 160 GW/cm^2, 27 times higher than in a GaP source limited by four-photon absorption [65]. Using 9-photon absorption and Keldysh photoionization models, we analyzed effects of pump-induced free-carrier generation on THz generation and the saturation of its efficiency. From the measurement of the intensity-dependent pump transmission, we obtained a value of $\beta_{9\mathrm{PA}} = (1.0 + 1.0/-0.5) \times 10^{-22}$ cm^{15}/GW^8 for the

9-photon absorption coefficient of GaP at 3.9 μm. With the measured 2 μJ pulse energy, the estimated THz peak electric field strength was 1 MV/cm. Because of its lateral uniformity, the GaP contact grating THz source is scalable to high pump pulse energies, available from powerful mid-infrared sources, and multi-MV/cm THz field strengths. The monolithic and collinear setup geometry is advantageous for user experiments, offering new possibilities for high-field THz applications.

4.2 Two-Photon absorption and its saturation in organic terahertz-generator crystals

Organic nonlinear crystals are very attractive for the efficient generation of strong-field THz pulses by optical rectification of femtosecond laser pulses. They have exceptionally large second-order nonlinear optical coefficients and can provide broad bandwidth (>5 THz) in a collinear geometry [74]. However, a disadvantage is the susceptibility of these materials to optical damage. Linear and multiphoton absorption of the pump can increase the crystal temperature above the melting point, or cause other degradation. Bonding the crystal to a substrate with high thermal conductivity, such as sapphire, increases the damage threshold. Besides heating, multiphoton absorption can produce free carriers, which absorb the generated THz radiation, thereby reducing the efficiency of THz generation [79]. For designing efficient and robust THz sources with organic crystals, it is important to have values for multiphoton absorption coefficients.

4.2.1 Methods and experimental data

Figure 4.11(a) shows photographs of the crystal samples, manufactured by Terahertz Innovations and used in our transmittance measurements. The shape of the samples varied and their size was about 10×10 mm^2. The thicknesses of the crystals were (430 ± 11.5) μm for NMBA, (237 ± 3.5) μm for BNA, and (662 ± 8.7) μm for MNA, as measured near their centers by a stylus profilometer (KLA Instruments, model Alpha-Step D-600). The uncertainties in the thickness values give the standard deviations along center lines across the areas illuminated by the laser beam (see Figure 4.18). To increase optical damage thresholds, the manufacturer fused the crystals to sapphire plates of 1 inch diameter for better heat removal [79]. A higher damage threshold was important to enable transmittance measurements at higher pump intensities, which would not be accessible with free-standing crystals but is needed for efficient THz generation.

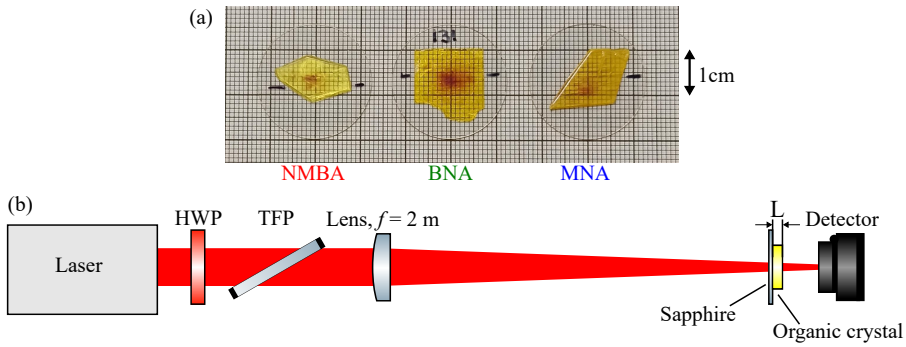

Figure 4.11: (a) Photograph of the organic crystal samples fused to sapphire plates. (b) Scheme of the experimental setup for the intensity-dependent transmittance measurements. HWP: half-wave retardation plate, TFP: thin-film polarizer [143].

All crystal samples were b- or (010)-cut, suitable for the most efficient THz generation by optical rectification [145, 147, 296]. In the linear and nonlinear transmission measurements, we set

the laser polarization along the polarization direction for the most efficient THz generation (indicated by the black markers in Figure 4.11(a): in NMBA [145] and MNA [147] close to the a-direction and in BNA along the c-direction [296]. We note that the colour inhomogeneity (browning), observable in Figure 4.11(a) near the center of each crystal, is a known effect of longer exposure to intense optical pumping and is associated with noncatastrophic damage different from melting [79]. The pictures were taken later, after longer usage of the crystals, but the optical measurements reported here were made in a new, intact condition of the crystals, before browning occurred. Additional measurements on used crystals are described in Section 4.2.3.

For the intensity-dependent (nonlinear) transmission measurements (see Figure 4.15), we used two laser sources with different wavelengths. A Ti:sapphire laser provided pulses of 100 fs duration (at half of the intensity maximum) and 780 nm mean wavelength (1.59 eV photon energy), at a repetition rate of 1 kHz (black solid line in Figure 4.12(b)). The other source, an Yb:CaF_2 laser, delivered pulses of 220 fs duration at 1030 nm mean wavelength (1.20 eV photon energy), with a repetition rate of 1 kHz. Because of the relatively large bandgap energies in all three materials, the lowest effective order of multiphoton absorption at 780 nm can be 2PA and at 1030 nm three-photon absorption.

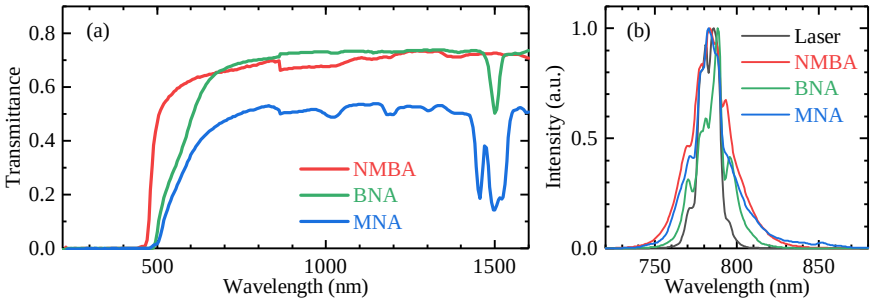

Figure 4.12: (a) Measured transmittances of the crystal samples at low intensity, as functions of the wavelength. (b) Normalized spectra transmitted through the crystal samples, measured with the 780-nm laser pulses at the highest average pump fluence of 6.3 mJ/cm^2. The spectrum of the incident laser pulses is shown for comparison (black solid line) [143].

With polarized light of low intensity in a spectrophotometer (PerkinElmer, model Lambda 1050), we measured the linear transmittances of the crystal samples. Figure 4.12(a) shows the measured transmittances as functions of wavelength. From these data, we calculated the bandgap energies of 2.75 eV in NMBA, 2.50 eV in BNA, and 2.56 eV in MNA. A comparison of the bandgap energies to the laser photon energies gives information on the lowest effective order of multiphoton absorption. To estimate the bandgap energies of the NMBA, BNA, and MNA organic crystal samples, we used the Tauc plots [297–299], as shown in Figure 4.13. Here, we plotted the quantity $(\alpha_0 h\nu)^{1/p}$ as function of the photon energy $h\nu$, where ν is the optical frequency, h is the Planck constant, and $\alpha_0(\nu)$ is the frequency-dependent linear absorption coefficient, with $\nu = c/\lambda$ and the speed of light, c. For materials with a direct bandgap, the Tauc exponent $p = 1/2$ is commonly used. In the Tauc plot, the fundamental absorption edge, associated with the bandgap, appears as a nearly linear, steep increase of the function value with increasing photon energy. The bandgap energy (E_g) can then be

determined as the energy corresponding to the linear extrapolation of this steep part to zero function value (to the horizontal axes in Figure 4.13). For the bandgap energies, we obtained 2.75 eV in NMBA, 2.50 eV in BNA, and 2.56 eV in MNA, which agree well with previously reported values in Refs. [144, 145, 300], [80, 145], and [145, 146], respectively. The Tauc plots of NMBA and MNA in Figure 4.13 feature rising parts at photon energies below their respective bandgaps. These features are related to transmittance drops below 1% in NMBA and 2% in MNA within a 25-nm narrow band above the respective fundamental absorption edge and slower drops in a broader range (Figure 4.14). We note that these features were not observed in Ref. [145] and may be related to different crystal qualities.

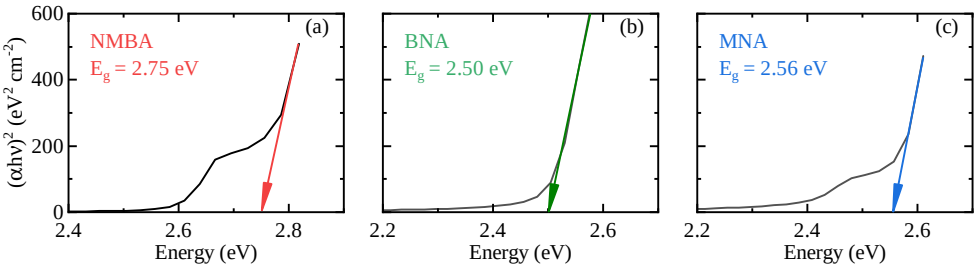

Figure 4.13: Tauc plots to determine the bandgap energies for the NMBA, BNA, and MNA crystal samples [143].

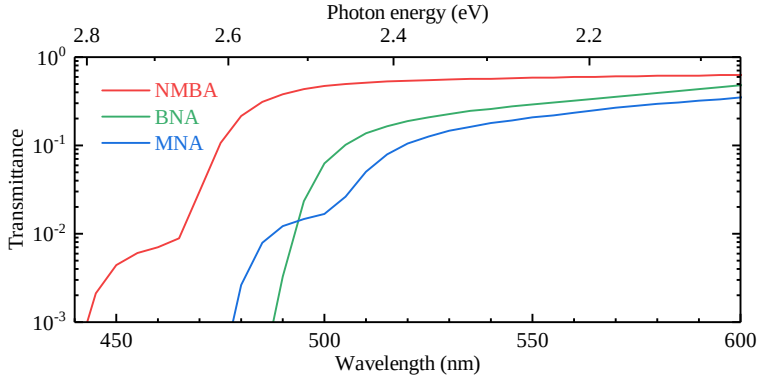

Figure 4.14: Transmittances above the fundamental absorption edges, measured in the NMBA, BNA, and MNA crystal samples as functions of the wavelength (bottom axis) and photon energy (top axis) [143]. Same data as in Figure 4.12(a).

The maximum pulse energy used in the experiment was about 4 mJ. The light intensity in the crystal sample was controlled by a half-wave retardation plate and a thin-film polarizer (Figure 4.11(b)). The laser beam first passed through the sapphire substrate and then through the organic crystal. To reduce possible effects of material inhomogeneity and thickness variation, and to exclude detector aperture effects, we placed the crystal samples into the weakly converging beam of a lens with a long focal length of 2 m. The lens reduced the beam diameter of the 780-nm (1030-nm) laser to $2w$ = 3.5 mm (2.7 mm) (at $1/e^2$ of the intensity maximum) at the sample and to a slightly smaller value at the detector. For the nonlinear transmission measurements, we used a detector (Gentec, model BEAMAGE-4M) with a sensitive surface of 20.5×20.5 mm^2. At the sample entrance, the maximum fluence

was 6.3 mJ/cm^2, averaged over the beam cross section πw^2, and the maximum intensity was 65 GW/cm^2, averaged over the pulse duration τ and the beam cross section. Throughout the paper, fluence and intensity values refer to such averaging. Up to this highest fluence, we did not observe any damage to the three crystal samples. (For comparison, the damage threshold of a 200- μm thin BNA on sapphire with similar laser parameters is about 13 mJ/cm^2 [79].) No variation of the transmitted beam size was observed, and possible beam reshaping effects on the transmission due to the nonlinear phase could be excluded. Reference measurements without and with the bare sapphire substrate confirmed the linearity of the detector response within the range of interest.

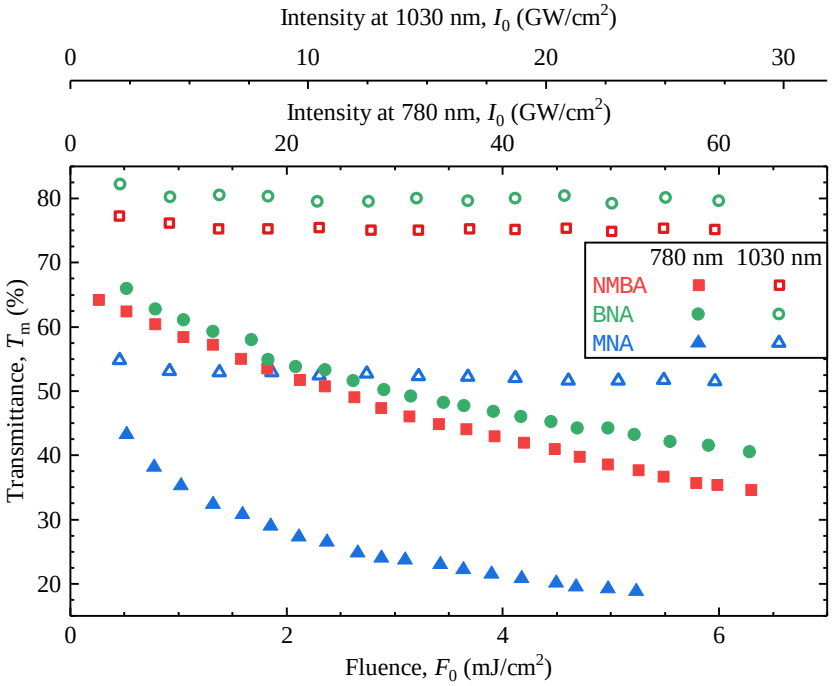

Figure 4.15: Measured transmittances (T_m) of the organic crystals NMBA (red squares), BNA (green circles), and MNA (blue triangles) at 780 nm (full symbols) and 1030 nm (empty symbols) wavelengths, as functions of the incident pump fluence (F_0), averaged over the beam cross section (bottom axis). The top axes indicate the corresponding incident intensities, averaged over the pulse duration and the beam cross section, for the 780-nm and the 1030-nm pulses [143].

Figure 4.15 shows the optical transmittances (T_m) of the NMBA, BNA, and MNA crystal samples, measured at the laser wavelengths of 780 nm (full symbols) and 1030 nm (empty symbols), as functions of the incident pump fluence $F_0 = E/(\pi w^2)$ and intensity $I_0 = F_0/\tau$. Here, E is the laser pulse energy, w is the laser spot radius, and τ = 100 fs (220 fs) is the pulse duration of the 780-nm (1030-nm) laser. For all three organic materials, the transmittances at 780 nm decrease with increasing fluence. Ludlow *et al.* found similar behavior with 800-nm pulses up to 3 mJ/cm^2 fluence, with somewhat higher transmittances [145], probably due to different crystal qualities. In contrast to 780 nm, at 1030 nm the transmittances are nearly constant (empty symbols in Figure 4.15). This indicates that strong 2PA is present at 780 nm, but no significant three-photon absorption occurs at 1030 nm within the applied intensity range [301–303].

To determine the 2PA coefficient, it is helpful to use the transmittance of a free-standing (bare) organic crystal slab, without the effect of the sapphire substrate. In the calculation model, we took into account the different qualities and, hence, reflection coefficients of the front and back surfaces of the bare organic crystals, R and R_s, respectively. The quality of the front surfaces was determined mainly by the sapphire surface of high polishing quality fused to the sample, whereas the quality of the back surfaces by the lower polishing quality of the sample (Figure 4.11). By assuming a flat air-crystal front surface, we calculated R from the measured refractive indices of the crystal samples. For the rough crystal-air back surface with scattering, we obtained R_s from fit to the experimental data, as described in Section 4.2.2 below. The transmittance of the free-standing organic crystal slab (T) can be obtained by multiplying the measured transmittance (T_m) with a correction factor:

$$T = \frac{(1-R)}{(1-R_1)(1-R_2)} T_\mathrm{m}. \tag{4.14}$$

Here, R_1 and R_2 are the intensity reflection coefficients at the air-sapphire and sapphire-crystal surfaces, respectively. Because the contribution of multiple internal reflections to the total transmitted intensity is below 1%, we neglected this in Equation 4.14. The corrected transmission (T) includes losses due to the first reflections at the flat front air-crystal and rough back crystal-air surfaces, and the absorption inside the crystal. We calculated the reflection coefficients R_1 and R_2 from the measured refractive indices of the crystal samples and from the literature value of the refractive index of sapphire, 1.76 [79]. Within the intensity and wavelength ranges applied here, sapphire can be regarded as a transparent plate with no intensity dependence of the refractive index. Using a spectroscopic ellipsometer (Semilab, model SE-2000), we determined the refractive indices of the organic crystal samples as a function of the wavelength, $n(\lambda)$ (Figure 4.16). The measured data are in good agreement with the data in the literature above the fundamental absorption edges. At 780 nm wavelength, the measured refractive indices are 2.03 for NMBA, 1.82 for BNA, and 2.23 for MNA. These values match within 1.5% the reported data, 2.01 [144, 304], 1.84 [141], and 2.20 [146, 305], respectively. To calculate the reflection coefficients R_1, R_2, and R, and the corrected transmittances of the free-standing organic crystal slabs (T), we used the measured refractive indices and the measured transmittances (T_m, see the main article). Here, R_1, R_2, and R are the intensity reflection coefficients for perpendicular incidence at the air-sapphire, sapphire-crystal, and flat crystal-air surfaces, respectively. The values of $R = (n-1)^2/(n+1)^2$ at 780 nm are 11.6% for NMBA, 8.5% for BNA, and 14.5% for MNA.

From the measured refractive indices and the corrected transmittances, we calculated the linear absorption coefficients as functions of the wavelength, $\alpha_0(\lambda)$ (Figure 4.16). For the calculation, we used the following formula [306]:

$$\alpha_0 = \frac{1}{L} \ln \left[\frac{2TR^2}{\sqrt{(1-R)^4 + 4T^2R^2} - (1-R)^2} \right] \tag{4.15}$$

Here, L is the thickness of the organic crystal. At 780 nm wavelength, we obtained linear absorption coefficients of 3.5 cm^{-1} for NMBA, 6.7 cm^{-1} for BNA, and 4.5 cm^{-1} for MNA.

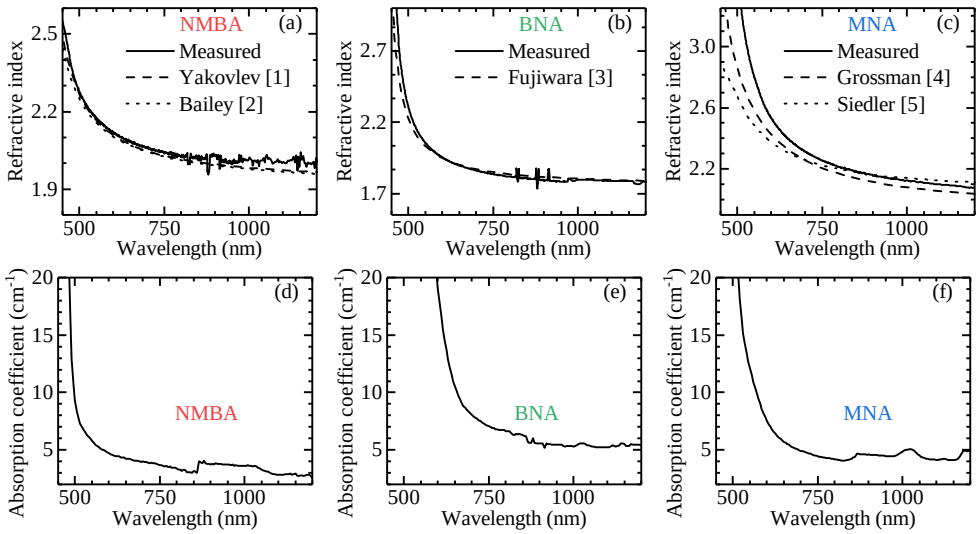

Figure 4.16: Measured refractive indices $n(\lambda)$ and linear absorption coefficients $\alpha_0(\lambda)$, which has not been reported yet for NMBA, BNA, and MNA, as functions of the wavelength (solid lines). Other refractive index data (dashed and dotted lines) are from the indicated literature. The small jumps in the absorption coefficient data near 850 nm are due to a grating exchange in the spectrophotometer [143].

For BNA, 5.3 cm^{-1} was reported elsewhere [307], matching within 21% our result. To our knowledge, for NMBA and MNA no optical absorption data have been reported yet. In the following discussion, we focus on the 780-nm case. The goal is to characterize 2PA in the organic crystals and to determine the relevant material data.

4.2.2 Two-photon absorption in NMBA

Based on the experimental data presented in Section 4.2.1, we start with a simple 2PA model [308, 309], $\mathrm{d}I/\mathrm{d}z = -\beta_0 I^2$, where β_0 is the 2PA coefficient, and z is the propagation coordinate inside the crystal sample. The solution to this propagation equation is $I(z) = I(0)/\left[1 + I(0)\beta_0 z\right]$ [308, 309]. In this solution, replacing $I(0)$ by $(1-R)I_0$, $I(z)$ by $I_\mathrm{t}/(1-R_\mathrm{s})$, and z by L accounts for reflection losses (multiple reflections are neglected). Subsequent rearranging gives for the reciprocal transmittance through a free-standing crystal slab of thickness L the following expression:

$$\frac{1}{T} = \frac{I_0}{I_\mathrm{t}} = \frac{1}{(1-R)(1-R_\mathrm{s})} + \frac{\beta_0 L}{1-R_\mathrm{s}} I_0. \tag{4.16}$$

Here, I_t is the transmitted intensity. A linear fit based on Equation 4.16 to the reciprocal corrected transmittance data gives the 2PA coefficient β_0 [204, 310, 311], and the back-surface loss coefficient R_s.

For NMBA, the simple 2PA model of Equation 4.16 with β_0 = 0.41 cm/GW and R_s = 25.7% agrees well with the experimental data throughout the entire intensity range up to 65 $\mathrm{GW/cm}^2$ (Figure 4.17(a)). This indicates that 2PA determines the response of the material and this

response can be described by a single parameter β_0.

At low intensities of about $I \lesssim \alpha_0/\beta_0 \approx 8.5$ GW/cm^2, linear absorption is not negligible in NMBA and the analytic solution and Equation 4.16 are not accurate. Here, α_0 is the linear absorption coefficient (see Supplement 1: Refractive indices and linear absorption coefficients). Fitting the numerical solution of the propagation equation $\mathrm{d}I/\mathrm{d}z = -(\alpha_0+\beta_0 I)I$ to experiment gives $\beta_0 = 0.43$ cm/GW, about 5% larger than with the analytic solution. Furthermore, a simple calculation shows that about half of the losses represented by R_s originates from linear absorption and scattering contributes with about 2% on top of the Fresnel loss. In contrast to NMBA, in BNA and MNA the simple model with an intensity-independent 2PA coefficient can fit the experimental data only at lower intensities, up to about 20 GW/cm^2 in BNA and 13 GW/cm^2 in MNA (dashed lines in Figures 4.17(b) and 4.17(c), respectively). At higher intensities, the simple model strongly underestimates the transmittances of BNA and MNA. Such a discrepancy clearly indicates that the simple 2PA model is not sufficient to describe the intensity dependence of the crystal absorption and that other effects also contribute.

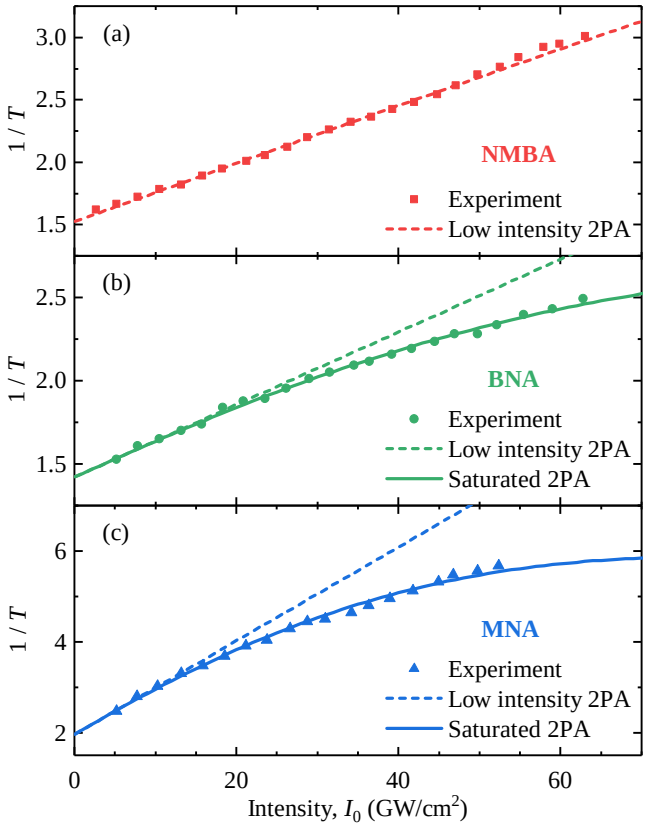

Figure 4.17: Reciprocal transmittance ($1/T$) as function of the incident laser intensity (I_0) for NMBA (a), BNA (b), and MNA (c). Symbols: corrected transmittance data, dashed lines: linear fit based on Equation 4.16, solid lines: fit based on the saturated 2PA model [143].

4.2.3 Saturated two-photon absorption in BNA and MNA

A possible explanation why the observed behaviour in BNA and MNA deviates from the predictions of a simple 2PA model could be the onset of higher-order multiphoton absorption

above 20 GW/cm^2 and 13 GW/cm^2, respectively. For example, the increase of the four-photon absorption coefficient with increasing intensity was observed in GaP and ZnTe semiconductors, which may be explained by the contribution of five-photon absorption [312]. In our case, three-photon absorption would increase the nonlinear absorption $\beta_0 I + \gamma_0 I^2$, with a three-photon absorption coefficient $\gamma_0 > 0$, and consequently increase the reciprocal transmittance. However, we observed an opposite behaviour: the sublinear scaling of $1/T$ with intensity (symbols in Figures 4.17(b) and 4.17(c)). Therefore, we can rule out the onset of three-photon absorption at higher intensities. Furthermore, a negligible three-photon absorption in the investigated intensity range is also consistent with the nearly constant transmittances observed at 1030 nm wavelength (empty symbols in Figure 4.15).

Vicario et al. observed in DAST [209], another organic nonlinear crystal, a large spectral broadening of the transmitted optical pulses. In combination with linear absorption, such a spectral broadening can cause an effective nonlinear absorption different from 2PA. However, this mechanism could be ruled out in our case because the observed moderate spectral broadening (Figure 4.12(b)) was not sufficient to convert a significant fraction of the laser pulse energy to the absorption bands of BNA and MNA near 1500 nm wavelength, or below 600 nm near the fundamental absorption edges (Figure 4.12(a)).

At intensities where the transmittances in BNA and MNA start to deviate from the simple 2PA model, the nonlinear absorption is already strong. This can lead to a significant population of the excited state and the depletion of the ground state. Thus, reduction of the number of absorbing molecules may lead to the saturation of 2PA. The saturation of 2PA was observed in CdS semiconductor [310], organic conjugated polymers [311], and green fluorescent protein [313]. Two-photon-pumped lasing was reported in a dye-doped solid matrix [309]. Saturation of two- and three-photon absorption was observed in dye solutions [314]. The saturation of four-photon absorption in GaP and ZnTe semiconductors was also observed [312].

To fit the experimental data for BNA and MNA, we applied a saturated 2PA model. In this case, the saturated 2PA coefficient $\beta(I)$ is no longer constant but becomes intensity dependent [310, 311, 313, 314]. Some of the early works on saturated 2PA used a hyperbolic approximation $\beta(I) = \beta_0/(1+I/I_\mathrm{s})$ [310], similar to saturated single-photon absorption [315]. Here, I_s is the 2PA saturation intensity. Schroeder and Ullrich noticed that even though such an approximation can describe experimental data at low intensities well, it leads to incorrect values of β_0 and I_s [311]. More exact expressions were derived for homogeneously [311, 313] and inhomogeneously [313] broadened saturated 2PA coefficients. Because our samples are crystalline solids, to fit the experimental data, we used the expression for a homogeneously broadened system [311, 313],

$$\beta(I) = \frac{\beta_0}{1 + I^2/I_\mathrm{s}^2}. \tag{4.17}$$

In the saturated case, we refer to β_0 as the *low-intensity* 2PA coefficient. For such $\beta(I)$ and negligible linear absorption, Schroeder and Ullrich gave an expression for the sample transmittance. This expression can be easily modified to account for reflection and scattering losses at the sample surfaces (similarly to Equation 4.16 above):

$$T(I_0) = (1-R)(1-R_\mathrm{s}) \cdot \left[\frac{1}{2} \left(-\frac{I_\mathrm{s}^2}{{I_0}^2(1-R)^2} - \frac{I_\mathrm{s}^2}{I_0(1-R)} \beta_0 L + 1 \right) + \sqrt{\left(\frac{I_\mathrm{s}^2}{2{I_0}^2(1-R)^2} - \frac{I_\mathrm{s}^2}{2I_0(1-R)} \beta_0 L - \frac{1}{2} \right)^2 + \frac{I_\mathrm{s}^2}{{I_0}^2(1-R)^2}} \right] . \quad (4.18)$$

In the evaluation of the saturated 2PA parameters for BNA and MNA, we first determined β_0 and R_s by a linear fit to the low-intensity part of the data, similarly to the simple 2PA case based on Equation 4.16. Then we used Equation 4.18 to fit the full set of the corrected transmittance data, with I_s as the only free parameter. Table 4.1 lists the best-fitting values of the low-intensity 2PA coefficients (β_0) and the 2PA saturation intensities (I_s). The corresponding values of R_s are 23.1% in BNA and 40.3% in MNA, with estimated contributions of back-surface scattering of about 1.4% and 5.1%, reypectively. To obtain the uncertainties of β_0 and I_s, we varied one of these parameters while keeping the other one fixed at the best-fitting value and allowed for a twofold increase in the root-mean-square deviation from the experimental data. With the best-fitting values, the calculated intensity dependence of the reciprocal transmittance is in good agreement with the experimental data throughout the entire intensity range (solid curves in Figures 4.17(b) and 4.17(c)).

Table 4.1: Low-intensity 2PA coefficients (β_0) of NMBA, BNA, and MNA and 2PA saturation intensities (I_s) of BNA and MNA at 780 nm, obtained with the analytic and the numerical models [143].

Material	Low-intensity 2PA coefficient β_0 (cm/GW)		2PA satuation intensity I_s (GW/cm^2)	
	Analytic	Numerical	Analytic	Numerical
NMBA	0.41 ± 0.02	0.43	—	
BNA	0.71 ± 0.03	0.78	77^{+15}_{-9}	71
MNA	0.93 ± 0.03	1.07	37^{+6}_{-4}	34

The low-intensity 2PA coefficients of BNA and MNA are similar, 0.71 cm/GW and 0.93 cm/GW, respectively. In contrast, the 2PA saturation intensity of MNA (37 GW/cm^2) is about two times smaller than that of BNA (77 GW/cm^2), indicating a stronger saturation in MNA. This is also visually obvious from the larger deviation of the experimental data from the simple (unsaturated) 2PA model in MNA (dashed line in Figure 4.17(c)). Comparison shows that the fluence corresponding to the 2PA saturation intensity in BNA, $I_\mathrm{s}\tau$ = 7.7 mJ/cm^2 (Table 4.1), and the damage threshold of BNA on sapphire as mentioned in Section 4.2.1, for a thin crystal about 13 mJ/cm^2 [79], are of similar magnitude and the latter is about 1.7-times larger.

Because nonlinear absorption may depend on crystal quality and organic crystals are difficult to grow, the crystal quality can have sample-to-sample variations or may degrade with usage and time. We investigated the same three crystal samples at a few different positions (Figure 4.18), after extensive use. The crystals were stored for a few months under ambient conditions between the measurements in the intact and used states. (Figure 4.17, Table 4.1) discusses

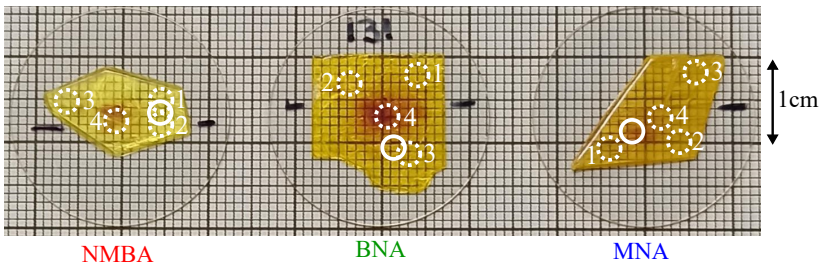

Figure 4.18: Photographs of the organic crystal samples (same as 4.11(a)), with locations of the laser spot in different nonlinear transmittance measurements. Solid circles refer to the intact-state, and the dotted circles to the used-state measurements [143].

the results with the new intact crystals. Here, we also compare the results with intact samples to those with used ones (Figure 4.19, Table 4.2). For a better accuracy of the 2PA parameters β_0 and I_s, in the evaluation of the transmittance measurements, we used the local sample thicknesses at each position, as measured with a profilometer (KLA Instruments, model Alpha-Step D-600).

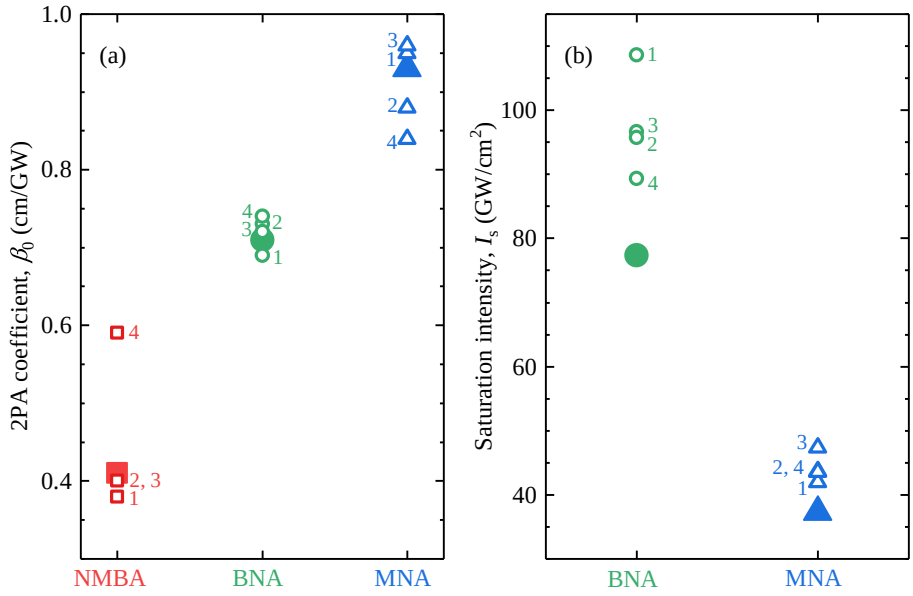

Figure 4.19: (a) Low-intensity 2PA coefficients (β_0) and (b) 2PA saturation intensities (I_s), measured at different positions on the NMBA, BNA, and MNA crystal samples at 780 nm and evaluated with the analytic model [143]. Full symbols: intact crystals (same data as in Table 4.1); empty symbols: used crystals, with position labels (Figure 4.18).

The relative deviation of the low-intensity 2PA coefficients in the used state from those given in Table 1 for new intact crystals was in most cases less than 10%. The only exception is Position 4 in NMBA, which deviates by about 50%. This might be related to the browning damage at this spot, but in the other crystals we could not observe a clear similar correlation. For the 2PA saturation intensities, we found up to 40% (27%) increased values in the used BNA (MNA) crystals, which could hint at some slow change or degradation of these samples. These findings support the importance of crystal quality and conditions of use for the optical parameters.

The (low-intensity) 2PA coefficient of NMBA, obtained with the simple 2PA model without saturation (0.41 cm/GW), is nearly two times smaller than the low-intensity 2PA coefficients of BNA and MNA (Table 4.1). This difference is consistent with the absence of saturation in NMBA, because with weaker 2PA also the excited-state population is expected to be smaller. Similarly to NMBA, at low intensities of about $I \lesssim \alpha_0/\beta_0 \approx$ 9.4 GW/cm^2 (4.8 GW/cm^2) in BNA (MNA), linear absorption is not negligible and the analytic Equation 4.18 is not accurate. Fitting the numerical solution of the propagation equation $\mathrm{d}I/\mathrm{d}z = -\alpha_0 I - \beta(I)I^2$ to experiment gives for BNA (MNA) β_0 = 0.78 cm/GW (1.07 cm/GW), about 10% (15%) larger than with the analytic solution. The saturation intensity is 71 GW/cm^2 (34 GW/cm^2), about 8% smaller than with the analytic solution.

In future work, a more accurate 2PA model, going beyond one-dimensional propagation, needs to take into account the effects of linear absorption and the intensity variation across the laser beam. Nonlinear absorption directly affects THz generation in two ways: (i) it influences the optical pump intensity during propagation through the crystal; (ii) free carriers generated by pump absorption can increase the absorption at THz frequencies. Furthermore, as discussed above, nonlinear pump absorption is related to damage, which limits the useful pump intensity for THz generation. The effective values of the 2PA material data in Table 4.1 can be used in more realistic simulation models of THz generation and for more accurate estimations of the crystal temperature and the damage threshold.

Table 4.2: Low-intensity 2PA coefficients (β_0) and 2PA saturation intensities (I_s), measured at different positions on the NMBA, BNA, and MNA crystal samples at 780 nm and evaluated with the analytic model [143] (Same data as in Figure 4.19).

Material	Position	Low-intensity 2PA coefficient β_0 (cm/GW)	2PA satuation intensity I_s (GW/cm^2)
NMBA	intact	0.41	—
	1	0.38	
	2	0.40	
	3	0.40	
	4	0.59	
BNA	intact	0.71	77
	1	0.69	109
	2	0.73	97
	3	0.72	96
	4	0.74	89
MNA	intact	0.93	37
	1	0.95	42
	2	0.88	44
	3	0.96	47
	4	0.84	44

4.2.4 Conclusions

Organic nonlinear optical crystals, pumped by femtosecond laser pulses in a simple collinear geometry, are very attractive for the efficient generation of strong-field THz pulses by optical rectification. Crystals like NMBA, BNA, and MNA can be pumped directly at common laser wavelengths. However, optical absorption in these crystals can critically limit the THz-generation efficiency and result in optical damage. For the development of high-power and high-field THz sources based on these promising materials, it is important to know the nonlinear absorption. Therefore, in NMBA, BNA, and MNA crystals, we measured intensity-dependent transmittances at the common laser wavelengths of 1030 nm and 780 nm. In BNA and MNA, pumped at 780 nm, the measurements revealed strongly saturated two-photon absorption above 20 GW/cm^2 (2.0 mJ/cm^2) and 13 GW/cm^2 (1.3 mJ/cm^2) intensities (fluences), respectively. In NMBA, within the observed range up to about 60 GW/cm^2 (6 mJ/cm^2), we did not observe the saturation of two-photon absorption. We gave effective values for the low-intensity two-photon absorption coefficients and the saturation intensities for two-photon absorption. Our results enable to build better numerical models of THz generation and optical heating, with nonlinear pump absorption included, as well as more accurate predictions on optical damage. These capabilities will aid the design and optimization of robust strong-field THz sources using organic crystals pumped by femtosecond lasers directly, without frequency conversion.

Chapter 5

Summary

Strong-field terahertz (THz) radiation has rapidly evolved into a central tool for probing and controlling matter [246, 247]. Its unique ability to interact with low-energy excitations makes it invaluable across diverse applications, ranging from particle acceleration [29, 38, 42] to nonlinear spectroscopy [246] and even emerging medical techniques [316, 317]. The generation of intense THz fields is therefore a cornerstone of modern ultrafast science, and recent advances have focused on developing compact, efficient, and scalable THz sources.

Semiconductor materials [65, 93, 188] have recently emerged as promising alternative sources of strong THz fields. However, semiconductors with small bandgaps face a significant drawback at common near-infrared pump wavelengths. They suffer from strong two- and three-photon absorption and reduces THz generation efficiency. A promising solution is the use of longer pump wavelengths, beyond 1 μm [63, 86]. At these wavelengths, low-order multiphoton absorption is strongly suppressed, allowing efficient THz generation without compromising material integrity. Importantly, the pulse-front tilt (PFT) angles required for velocity matching in semiconductors remain relatively small, typically below 30° [65]. This is a crucial advantage, as it enables the use of contact-grating (CG) technology, which integrates the grating directly onto the semiconductor surface. This grating structure [39] at the entrance surface of the semiconductor crystal tilts the intensity front of the pump pulse to achieve velocity matching. CG-based designs eliminate the need for bulky external optics, resulting in highly efficient and compact monolithic THz sources. Demonstrations in ZnTe [69] and GaP [199] have already validated the effectiveness of this approach, showing that semiconductor CG emitters can achieve strong THz output with minimal complexity. The emergence of powerful mid-infrared optical parametric chirped-pulse amplification (OPCPA) and laser systems [70–72] further strengthens this strategy. By avoiding the detrimental multiphoton absorption that plagues near-infrared pumping, mid-IR drivers provide an ideal platform for scaling THz output. Semiconductor CG emitters driven by mid-IR OPCPA systems offer a pathway to overcome longstanding limitations in THz generation, enabling strong-field sources free from multiphoton absorption losses. In this work, I investigated a GaP contact-grating THz source operated in a previously unaccessed mid-infrared pump wavelength range around 4 μm and explored some of the limitations by combining experiments with numerical simulations. Below, thesis points 1 and 2 summarize the corresponding results.

Organic nonlinear optical crystals have proven to be another highly efficient class of materials for strong-field terahertz (THz) generation [73, 74, 76–80, 145, 165, 202, 205, 208, 212]. Their large nonlinear coefficients, favorable phase-matching properties, and broad transparency windows make them attractive alternatives to conventional inorganic crystals. In many cases, organic materials can achieve higher conversion efficiencies, positioning them as leading candidates for next-generation THz emitters. Despite these advantages, organic crystals face significant challenges when pumped at shorter near-infrared wavelengths. Multiphoton absorption processes, particularly two- and three-photon absorption, become prominent under strong-field excitation [79, 145, 148, 215]. These nonlinear absorption effects reduce THz generation efficiency, introduce heating, and can lead to irreversible material damage. The problem is especially severe at high repetition rates, where cumulative heating and absorption effects limit operational stability [215, 318, 319]. Consequently, while organic crystals are efficient THz emitters, their performance is strongly dependent on pump wavelength and operating conditions. To address these issues, several thermal management strategies have been proposed [79, 215]. These include active cooling systems, optimized crystal geometries, and careful control of pump fluence to minimize heating. Such approaches can extend the operational lifetime of organic crystals and reduce damage risks, but they do not fully eliminate the underlying problem of multiphoton absorption. Moreover, the effectiveness of these strategies varies depending on the specific crystal material and experimental configuration. Thus, while thermal management can mitigate damage, it cannot substitute for a fundamental understanding of the nonlinear absorption processes themselves. A critical limitation in the current understanding of organic THz sources is the lack of reported multiphoton absorption parameters. Key quantities such as damage thresholds, and wavelength-dependent nonlinear coefficients remain largely uncharacterized for many organic materials. This absence of systematic data hinders predictive modeling of performance and makes it difficult to design robust THz sources with confidence. The lack of predictive understanding also complicates efforts to compare organic crystals with other classes of THz emitters, such as semiconductors or lithium niobate, under equivalent operating conditions. However, multiphoton absorption at shorter pump wavelengths remains a fundamental obstacle, leading to reduced efficiency and material degradation. Future research should prioritize systematic measurement of multiphoton absorption parameters, damage thresholds, and thermal properties across a wide range of organic crystals. Such data will enable predictive modeling, guide the design of optimized THz sources, and unlock the full potential of organic materials in strong-field regimes. With these advances, organic crystals could become central to the next generation of efficient, high-power THz emitters, complementing semiconductor and inorganic approaches and expanding the toolbox of ultrafast science. Motivated by this knowledge gap, I characterized the nonlinear absorption of organic THz generator crystals like the widely-used BNA, and the novel NMBA and MNA. Below, thesis points 3 and 4 summarize the corresponding results.

5.1 Thesis points

1. A novel gallium phosphide (GaP) contact-grating THz source with a trapezoidal line profile was demonstrated using a 3.9 μm mid-infrared pump. The estimated THz peak electric field strength with 2 μJ pulse energy was 1 MV/cm. Because of its lateral uniformity, plane-parallel geometry, and availability of large GaP single crystals of good quality, it is scalable to high pump pulse energies, multi-MV/cm THz field strengths, and can generate nearly-single-cycle THz pulses with a broad spectral bandwidth reaching 6 THz. At this long pump wavelength of 3.9 μm, the lowest-order effective multiphoton absorption process was 9-photon absorption, enabling the use of remarkably high pump intensities up to 310 GW/cm^2 [272]. The THz generation efficiency saturated at approximately 160 GW/cm^2, which is about 27 times higher than in a GaP source limited by four-photon absorption [65].The monolithic and collinear setup geometry is advantageous for experiments, offering a powerful and scalable platform for strong field THz science, nonlinear spectroscopy, and ultrafast material control, ideally compatible with emerging powerful MIR pump sources offering new possibilities for high-field THz applications .

2. Based on high-order multiphoton absorption and Keldysh photoionization frameworks, I developed simulation models suitable to consistently predict both intensity-dependent optical pump absorption and THz generation in a broad intensity range, exceeding 300 GW/cm^2 in mid-infrared pumped GaP. From intensity-dependent pump transmission measurements, using the model based on multiphoton absorption, I determined a 9-photon absorption coefficient of $\beta_{9\mathrm{PA}} = (1.0 + 1.0/-0.5) \times 10^{-22}$ cm^{15}/GW^8 in GaP at 3.9 μm wavelength. By comparing measurements and simulations, I showed that the observed saturation of THz conversion efficiency at high pump intensities arises from pump-induced free-carrier generation. I incorporated a spatial averaging over the pump beam cross section and found it crucial for reproducing the experimental observation at high intensities, demonstrating that realistic beam-profile effects must be included for accurate modelling. These results provide a comprehensive experimental–theoretical description of nonlinear pump absorption and its impact on mid-infrared driven THz generation [272].

3. For the widely used organic THz-generator crystal BNA, and the new promising organic THz-generator crystals NMBA and MNA, I measured the intensity-dependent pump transmittance at the common laser wavelength of 780 nm. I determined the corresponding low-intensity effective two-photon absorption coefficients to be (0.41 $\pm$ 0.02) cm/GW for NMBA, (0.71 $\pm$ 0.03) cm/GW for BNA, and (0.93 $\pm$ 0.03) cm/GW for MNA. These results can enable improved numerical models of THz generation and optical heating, incorporating nonlinear pump absorption, to support the design of simple and robust strong-field THz sources using organic crystals directly pumped by femtosecond lasers [143].

4. At higher pump intensities of 780 nm wavelength, I showed that the intensity-dependent absorption in BNA and MNA exhibit clear deviations from pure two-photon absorption. Three-photon absorption, as well as the combined effect of linear absorption and spectral broadening

could be excluded as possible reasons for this behaviour. I showed that the effect can be explained by a saturation of two-photon absorption, occurring above an intensity of 20 GW/cm^2 in BNA and 13 GW/cm^2 in MNA. In contrast, NMBA showed no evidence of two-photon absorption saturation within the explored intensity range up to approximately 60 GW/cm^2. In BNA and MNA, I determined the saturation intensities of two-photon absorption to be 77^{+15}_{-9} GW/cm^2 and 37^{+6}_{-4} GW/cm^2, respectively [143].

Chapter 6

Magyar nyelvű összefoglaló

Az erős terű THz-es sugárzás napjainkra kulcsfontosságú eszközzé vált az anyagvizsgálatban és egyes anyagi tulajdonságok szabályozásában [246, 247], előmozdítva olyan alkalmazásokat, mint a részecskegyorsítás [29, 38, 42], nemlineáris spektroszkópa [246], valamint új orvosi diagnisztikai és gyógyászati módszerek [316, 317]. Egyes félvezető anyagok az utóbbi években ígéretesnek bizonyultak nagy térerősségű THz-es impulzusok keltésében [65, 93, 188], azonban tipikus közeli infravörös pumpáló hullámhosszakon két- és háromfotonos abszorpció lép fel a viszonylag keskeny tiltott sáv miatt. A káros alacsonyrendű többfotonos abszorpció kiküszöbölhető nagyobb meghajtó hullámhosszak alkalmazásával [63, 86]. A meghajtó optikai és a keltett THz-es impulzusok közötti sebességillesztéshez viszonylag kicsi – jellemzően 30° alatti [65] – impulzusfront-dőlési szög szükséges. Ez lehetővé teszi az ún. kontaktrács technológián alapuló, egyetlen komponensből álló hatékony THz-es források megvalósítását, amit ZnTe [69] és GaP [199] esetében korábban már demonstráltak. A gyorsan fejlődő, nagy teljesítményű közép-infravörös OPCPA- és lézerrendszerek [70–72] ideális meghajtó forrásai lehetnek olyan félvezető anyagú THz-es forrásoknak, amelyek mentesek az alacsonyrendű többfotonos abszorpció káros hatásaitól. Jelen munkában egy 4 μm körüli közép-infravörös hullámhosszon meghajtott GaP anyagú kontaktrácsos THz forrást vizsgáltam. Kísérletek és numerikus szimulációk segítségével elemeztem a legfontosabb korlátozó tényezőket ebben az adott alkalmazás szempontjából korábban nem vizsgált tartományban. A vonatkozó eredményeket az alábbi 1. és 2. tézispont foglalja össze.

Magas hatásfokú THz-es források egy másik csoportja szerves anyagú nemlineáris kristályokon alapul [73, 74, 76–80, 145, 165, 202, 205, 208, 212]. Egyik hátrányuk azonban, hogy – különösen rövidebb meghajtó hullámhosszak esetében – a többfotonos abszorpció korlátozza az elérhető hatásfokot [79, 145, 148, 215], fokozza a kristály melegedését és roncsolódást is okozhat. Léteznek ugyan hőhatást csökkentő módszerek [79, 215], de a korlátozó tényezők a nagy ismétlési frekvenciák esetében még erősebben jelentkeznek [215, 318, 319]. A kulcsfontosságú többfotonos abszorpció részletesebb vizsgálata korábban nem történt meg, ami korlátozza az elérhető teljesítmény és a roncsolási küszöb előrejelezhetőségét. Jelen munkában ezt a hiányt igyekeztem pótolni egyes szerves THz-keltő kristályok – így a széles körben használt BNA, valamint az új NMBA és MNA – nemlineáris abszorpciójának jellemzésével. A vonatkozó eredményeket az alábbi 3. és 4. tézispont foglalja össze.

6.1 Tézispontok

1. Egy új, 3,9 μm-es közép-infravörös hullámhosszon meghajtott, trapéz keresztmetszetű vonalprofilt alkalmazó gallium-foszfid (GaP) kontaktrácsos THz-forrást demonstráltam. A keltett THz-es impulzusok elektromos térerősségének becsült csúcsértéke 2 μJ impulzusenergia esetében elérte az 1 MV/cm-t. A sík-párhuzamos geometriának, valamint a jó minőségű, nagy méretű GaP egykristályok elérhetőségének köszönhetően a forrás jól skálázható nagy meghajtó impulzusenergiára és több MV/cm térerősségre. Képes nagy, akár 6 THz spektrális sávszélességű, közel egyciklusú THz-es impulzusok előállítására. A legalacsonyabb rendű effektív többfotonos abszorpciós folyamat a kilencfotonos abszorpció volt az alklamazott nagy, 3,9 μm-es meghajtó hullámhosszon, ami lehetővé tette a rendkívül nagy, akár 310 GW/cm^2 pumpáló intenzitás alkalmazását [272]. A THz-keltés hatásfoka 160 GW/cm^2 pumpáló intenzitásnál telítődött, ami mintegy 27-szerese a négyfotonos abszorpció által korlátozott intenzitásnak [65]. Az egyetlen komponensből alló, egyszerű kollináris pumpálású THz forrás kifejezetten előnyös kísérletekhez az erős terű THz-es fizika, a nemlineáris spektroszkópia, valamint az ultragyors folyamatok vizsgálatában és kontrollálásában. A nagy teljesítményű közép-infravörös pumpáló forrásokkal való kompatibilitása révén új lehetőségeket nyit a nagy térerősségű THz-es alkalmazásokban.

2. Magasrendű többfotonos abszorpción és Keldysh-féle fotoionizációs elméleten alapuló szimulációs modelleket dolgoztam ki, amelyek alkalmasak arra, hogy előre jelezzék mind a meghajtó közép-infravörös impulzusok intenzitásfüggő abszorpcióját, mind pedig a THz-keltést egy igen széles, akár 300 GW/cm^2-t is meghaladó intenzitástartományban GaP esetében. A pumpa intenzitásfüggő transzmissziójának méréséből – a többfotonos abszorpción alapuló modell alkalmazásával – meghatároztam a GaP 9-fotonos abszorpciós együtthatóját, amely $(1,0 + 1,0/ - 0,5) \times 10^{-22}$ cm^{15}/GW^8 értékűnek adódott 3,9 μm hullámhosszon. Mérések és szimulációk összehasonlításával kimutattam, hogy a THz-konverziós hatásfok nagy pumpáló intenzitásoknál megfigyelt telítődése a pumpa által keltett szabad töltéshordozók hatására vezethető vissza. A pumpáló nyaláb keresztmetszetére kiterjesztett térbeli átlagolás kulcsfontosságúnak bizonyult a nagy intenzitásoknál mért kísérleti eredmények reprodukálásához. Megállapítható tehát, hogy pontos modellezéshez szükséges a valósághű nyalábprofil hatásainak figyelembevétele is. Ezek az eredmények átfogó kísérleti és elméleti leírást adnak az alkalmazott közép-infravörös meghajtó impulzusok nemlineáris abszorpciójáról, valamint ennek THz-keltésre gyakorolt hatásáról [272].

3. Egy széles körben használt szerves THz-keltő kristály, a BNA, valamint két új ígéretes kristály, az NMBA és az MNA esetében a gyakran használt 780 nm-es lézer hullámhosszon megmértem az intenzitásfüggő transzmittanciát. Mindhárom anyagra meghatároztam az alacsony intentzitásoknál érvényes kétfotonos abszorpciós együtthatót, amely BNA esetében (0,71 $\pm$ 0.03) cm/GW-nak, NMBA esetében (0,41 $\pm$ 0.02) cm/GW-nak és MNA esetében (0,93 $\pm$ 0,03) cm/GW-nak adódott. Az eredmények lehetővé teszik a THz-keltés és az optikai pumpálásból eredő hőhatás pontosabb numerikus modellezését, amely figyelembe veszi a meghajtó impulzusok nemlineáris abszorpcióját is. Mindez hozzájárulhat szerves kristályokat alkalmazó, egyszerű és megbízható erős terű THz-es források tervezéséhez, amelyek femtoszekundumos

lézerekkel közvetlenül, frekvenciaátalakítás nélkül meghajthatók [143].

4. Kimutattam, hogy BNA-ban és MNA-ban az intenzitásfüggő abszorpció vieselkedése nagyobb intenzitású, 780 nm-es hullámhosszú pumpálás hatására eltér a tiszta kétfotonos abszorpció esetében várhatótól. A lehetséges magyarázatok közül kizárható volt a háromfotonos abszorpció, illetve a lineáris abszorpció és spektrális kiszélesedés együttes hatása. Megmutattam, hogy a tapasztalt jelenség a kétfotonos abszorpció telítődésével magyarázható, amely BNA esetében 20 GW/cm^2, MNA esetében pedig 13 GW/cm^2 feletti intenzitásoknál jelentkezett. Ezzel szemben az NMBA esetében a vizsgált intenzitástartományban – nagyjából 60 GW/cm^2-ig – nem mutatkozott a kétfotonos abszorpció telítődésére utaló jel. BNA és MNA esetében a kétfotonos abszorpció telítési intenzitását rendre 77^{+15}_{-9} GW/cm^2-nek, illetve 37^{+6}_{-4} GW/cm^2-nek határoztam meg [143].

Publication list

Journal publications in the topic of thesis

[1] **A. Gupta**, R. Jutas, C. Gollner, A. Baltuška, A. Pugžlys, and J. A. Fülöp, "Broadband GaP Contact-Grating Terahertz Source Pumped at 3.9 μm," *Opt. Express*, vol. 34, accepted, 2026, https://doi.org/10.1364/OE.588300.

[2] **A. Gupta**, T. Zhang, V. Hanyecz, J. Bohus, V. Gupta, A. Sharma and J. A. Fülöp, "Two-photon absorption and its saturation in organic terahertz-generator crystals," *Opt. Mater. Express*, vol. 15, pp. 2056-2065, 2025, https://doi.org/10.1364/OME.557213.

Journal publications in other topics

[1] G. Rana, **A. Gupta**, A. Bhattacharya, S. P. Duttagupta, S. S. Prabhu, "Enhanced THz emission from photoconductive antennas by integrating photonic structures on a semi-insulating GaAs substrate," *Pramana J. Phys.*, vol. 99, no. 1, 2025, https://doi.org/10.1007/s12043-024-02886-0.

[2] P. J. Dalton, C. T. Shaw, J. T. Bradbury, C. D. W. Mosley, A. Sharma, V. Gupta, J. Bohus, **A. Gupta**, J.-G. Son, J. A. Fülöp, R. B. Appleby, G. Burt, S. P. Jamison, M. T. Hibberd, D. M. Graham, "Cryogenically-Cooled Periodically-Poled Lithium Niobate Wafer Stacks for Multi-Cycle Terahertz Pulses," *Appl. Phys. Lett.*, vol. 125, 141101, 2024, https://doi.org/10.1063/5.0230877.

[3] A. Sharma, V. Gupta, J.-G. Son, **A. Gupta**, J. A. Fülöp and T. Gebert, "Linearity of Fast and Highly Sensitive LiTaO3 Pyroelectric Detectors in the Terahertz Range," *IEEE Trans. Terahertz Sci. Technol.*, vol. 14, pp. 823-839, 2024, https://doi.org/10.1109/TTHZ.2024.3445603.

[4] G. Rana, A. Bhattacharya, **A. Gupta**, R. Jain, D. Ghindani, S. P. Duttagupta, S. S. Prabhu, "A Polarization-Resolved Study of Nanopatterned Photoconductive Antenna for Enhanced

Terahertz Emission," *IEEE Trans. Terahertz Sci. Technol.*, vol. 9, pp. 193-199, 2019, https://doi.org/110.1109/TTHZ.2019.2891022.

[5] E. Manikandan, B. S. Sreeja, S. Radha, M. Duraiselvam, **A. Gupta**, and S. S. Prabhu, "Microfabrication of Low Cost Frequency Selective Surface for Terahertz Wave by Laser Ablation," *J. Electron. Mater.*, vol. 48, pp. 2423-2429, 2019, https://doi.org/10.1063/5.0230877.

[6] **A. Gupta**, G. Rana, A. Bhattacharya, A. Singh, R. Jain, R. D. Bapat, S. P. Duttagupta, S. S. Prabhu, "Enhanced optical-to-THz conversion efficiency of photoconductive antenna using dielectric nano-layer encapsulation," *APL Photonics*, vol. 3, 051706, 2018, https://doi.org/10.1063/1.5021023.

[7] G. Rana, P. Deshmukh, S. Palkhivala, **A. Gupta**, S. P. Duttagupta, S. S. Prabhu, V. G. Achanta, G. S. Agarwal, "Quadrupole-Quadrupole Interactions as New Paradigam in Plasmon Induced Transparency," *Phys. Rev. Applied,*, vol. 9, 064015, 2018, https://doi.org/10.1103/PhysRevApplied.9.064015.

[8] E. Manikandan, B. S. Sreeja, S. Radha, M. Duraiselvam, **A. Gupta**, and S. S. Prabhu, "Microfabrication of terahertz frequency-selective surface by short- and ultrashort laser ablation," *Opt. Eng.*, vol. 58, 011007, 2018, https://doi.org/10.1117/1.OE.58.1.011007.

[9] S. C. Ambhire, S. Palkhivala, A. Agarwal, A. Gupta, G. Rana, R. Mehta, D. Ghindani, A. Bhattacharya, A. Venugopal, S. S. Prabhu, "“Pattern and Peel” method for fabricating mechanically tunable terahertz metasurface on an elastomeric substrate," *Opt. Mater. Express,*, vol. 8, pp. 3382-3391, 2018, https://doi.org/10.1364/OME.8.003382.

[10] E. Manikandan, B. S. Sreeja, S. Radha, **A. Gupta**, G. Rana, and S. S. Prabhu, "Laser Patterning of Thin Film Copper and ITO on Flexible Substrates for Terahertz Antenna Applications," *J. laser micro nanoeng.*, vol. 12, pp. 313-330, 2017, https://doi.org/10.2961/jlmn.2017.03.0023.

Non-refereed conference abstracts in the topic of thesis

[1] **A. Gupta**, R. Jutas, C. Gollner, A. Baltuška, A. Pugžlys, and J. A. Fülöp, "Broadband GaP Contact Grating Terahertz Source Pumped at 3.9 μm," in *10th International conference on Optical Terahertz Science and Technology*, Marburg, Germany, 8^{th}-12^{th} April, 2024.

[2] **A. Gupta**, T. Zhang, V. Hanyecz, and J. A. Fülöp, "Two-Photon Absorption of Organic Crystals BNA, NMBA, and MNA," in *10th International conference on Optical Terahertz Science and Technology*, Marburg, Germany, 8^{th}-12^{th} April, 2024.

[3] **A. Gupta**, T. Zhang, V. Hanyecz, and J. A. Fülöp, "Saturated Two-Photon Absorption of Organic Crystals BNA, NMBA, and MNA" in *49th International Conference on Infrared, Milimeter, and Terahertz Waves*, Perth, Australia, 1^{st}-6^{th} September, 2024.

[4] **A. Gupta**, R. Jutas, C. Gollner, A. Baltuška, A. Pugžlys, and J. A. Fülöp, "Broadband GaP Contact Grating Terahertz Source Pumped at 3.9 μm". in *48th International Conference on Infrared, Milimeter, and Terahertz Waves*, Montreal, Canada, 17^{th}-22^{nd} September, 2023.https://doi.org/10.1109/IRMMW-THz57677.2023.10299250.

Non-refereed conference abstracts in other topics

[1] R. Sharma, M. Schneller, V. Stummer, **A. Gupta**, V. Gupta, A. Sharma, J. A. Fülöp, A. Pugžlys, A. Baltuška, "Burst-Enabled THz Absorption Spectroscopy with Direct Thermo-Optical Detection" in *11th International conference on Optical Terahertz Science and Technology*, Durhum, North Carolina, USA, 12^{th}-17^{th} April, 2026.

[2] C. M. Garcia-Rosas, X. Ropagnol, V. Gupta, **A. Gupta**, A. Sharma, J. A. Fülöp, F. Blanchard, T. Ozaki, "Ultrafast carrier dynamics in undoped InSb driven by intense THz pulses" in *50th International Conference on Infrared, Milimeter, and Terahertz Waves*, Espoo, Finland, 17^{th}-23^{th} August, 2025. https://doi.org/10.1109/IRMMW-THz61557.2025.11319990.

[3] A. Sharma, V. Gupta, J.-Gon Son, **A. Gupta**, J. Bohus, and J. A. Fülöp, "Linearity of Fast and Highly Sensitive LiTaO3 Pyroelectric Detectors in the Terahertz Range," in *Conference on Lasers and Electro-Optics Europe and European Quantum Electronics Conference (CLEO/Europe-EQEC)*, Munich, Germany, 23^{rd}-27^{th} June, 2025. https://opg.optica.org/abstract.cfm?URI=CLEO_Europe-2025-cc_p_15.

[4] **A. Gupta**, T. Zhang, P. P. Geetha, B. Nagyillés, B. Farkas, A. Körmöczi, S. Tóth, V. Gupta, A. Sharma, J. Csontos, Z. Divéki, J. A. Fülöp, "Few-Cycle Pulse Driven Terahertz Generation in Organic Crystals for THz–XUV Pump-Probe" in *50th International Conference on Infrared, Milimeter, and Terahertz Waves*, Espoo, Finland, 17^{th}-23^{th} August, 2025. https://doi.org/10.1109/IRMMW-THz61557.2025.11319730.

[5] P. J. Dalton, C. T. Shaw, J. T. Bradbury, C. D. W. Mosley, A. Sharma, V. Gupta, J. Bohus, **A. Gupta**, J.-G. Son, J. A. Fülöp, R. B. Appleby, G. Burt, S. P. Jamison, M. T. Hibberd, D. M. Graham, "Multi-Cycle Terahertz Pulse Generation in Cryogenically-Cooled Periodically-Poled Lithium Niobate Wafer Stacks" in *50th International Conference on Infrared, Milimeter, and Terahertz Waves*, Espoo, Finland, 17^{th}-23^{th} August, 2025. https://doi.org/10.1109/IRMMW-THz61557.2025.11320017.

[6] R. Sharma, M. Schneller, V. Stummer, A. Pugzlys, A. Baltuska, J. A. Fülöp, **A. Gupta**, V. Gupta, A. Sharma, "Programmable Pulse Bursts for Terahertz Spectroscopy by using Bolometric only Detection" in *50th International Conference on Infrared, Milimeter, and Terahertz Waves*, Espoo, Finland, 17^{th}-23^{th} August, 2025. https://doi.org/10.1109/IRMMW-THz61557.2025.11319632.

[7] A. Sharma, V. Gupta, J.-Gon Son, **A. Gupta**, J. Bohus, and J. A. Fülöp, "Linearity of a Fast, Highly-Sensitive $LiTaO_3$ Pyroelectric Detector in the Terahertz Range," in *49th International Conference on Infrared, Milimeter, and Terahertz Waves*, Perth, Australia, 1^{st}-6^{th} September, 2024. https://doi.org/10.1109/CLEO/Europe-EQEC65582.2025.11110241.

[8] **A. Gupta**, T. Ostatnický, V. Gupta, A. Sharma, and J. A. Fülöp, "Ultrafast Control of Carrier Population in Germanium by Strong THz Field," in *49th International Conference on Infrared, Milimeter, and Terahertz Waves*, Perth, Australia, 1^{st}-6^{th} September, 2024. https://doi.org/10.1109/IRMMW-THz60956.2024.10697637.

[9] **A. Gupta**, V. Gupta, J. Bohus, K. Chordiya, M. U. Kahaly, A. Sharma, G. Polónyi, and J. A. Fülöp, "Ultrafast Carrier Dynamics in Germanium Driven by Strong THz Field," in *48th International Conference on Infrared, Milimeter, and Terahertz Waves*, Montreal, Canada 17^{th}-22^{nd} September, 2023. https://doi.org/10.1109/IRMMW-THz57677.2023.10299211.

[10] **A. Gupta**, V. Gupta, J. Bohus, K. Chordiya, M. U. Kahaly, A. Sharma, G. Polónyi, and J. A. Fülöp, "Ultrafast Carrier Dynamics in n-Doped Ge Driven by Strong-Field THz," in *Conference on Lasers and Electro-Optics Europe and European Quantum Electronics Conference (CLEO/Europe-EQEC),* Munich, Germany, 26^{th}-30^{th} June, 2023. https://doi.org/10.1109/CLEO/Europe-EQEC57999.2023.10231758.

[11] **A. Gupta**, V. Gupta, A. Sharma, and J. A. Fülöp, "Ultrafast Nonlinear Carrier Dynamics in n-Doped Ge at High Field Strengths," in *46th International Conference on Infrared, Milimeter, and Terahertz Waves*, Chengdu, China, 29^{th} Aug - 3^{rd} September, 2021. https://doi.org/10.1109/IRMMW-THz50926.2021.9566951.

[12] **A. Gupta**, V. Gupta, A. Sharma, B. Monoszlai, P. S. Nugraha, G. Polónyi, G. Krizsán, Á. Burián, S. Turnár, J. Hebling, G. Almási, and J. A. Fülöp, "Nonlinear THz Spectroscopy User Facility at ELI-ALPS," in *45th International Conference on Infrared, Milimeter, and Terahertz Waves*, Bufalo, New york, USA, 8^{th}-13^{th} November, 2020. https://doi.org/10.1109/IRMMW-THz46771.2020.9370703.

[13] **A. Gupta**, G. Rana, A. Bhattacharya, A. Singh, R. Jain, R. D. Bapat, S. P. Duttagupta, S. S. Prabhu, "Improving Efficiency of Terahertz Photoconductive Antenna Using Dielectric Nano-Layer Encapsulation," in *43rd International Conference on Infrared, Milimeter, and Terahertz Waves*, Nagoya, Japan, 9^{th}-14^{th} September, 2018. https://doi.org/10.1109/IRMMW-THz.2018.8510437.

[14] G. Rana, **A. Gupta**, A. Bhattacharya, S. P. Duttagupta, S. S. Prabhu, "Enhancing the THz emission through surface patterning in PhotoConductive Antenna," in *43rd International Conference on Infrared, Milimeter, and Terahertz Waves*, Nagoya, Japan, 9^{th}-14^{th} September, 2018. https://doi.org/10.1109/IRMMW-THz.2018.8510396.

[15] S. C. Ambhire, S. Palkhivala, A. Agarwal, **A. Gupta**, G. Rana, R. Mehta, A. Bhattacharya, A. Venugopal, S. S. Prabhu, "Reverse Fabrication Technique to Develop Mechanically Tunable THz Metasurfaces using a Flexible Polydimethylsiloxane Substrate," in *43rd International Conference on Infrared, Milimeter, and Terahertz Waves*, Nagoya, Japan, 9^{th}-14^{th} September, 2018. https://doi.org/10.1109/IRMMW-THz.2018.8509856.

ACKNOWLEDGEMENT

First and foremost, I would like to express my sincere gratitude to my supervisor, **Dr. József András Fülöp**, for his unwavering support, guidance, and the opportunities he provided throughout my doctoral studies. His mentorship played a crucial role in enabling me to pursue and complete my PhD at the University of Szeged.

I am thankful to **Tianmiao Zhang**, for the assistance provided during the laboratory experiments. I also extend my appreciation to all members of the THz group at ELI ALPS for their continuous support and motivation during this journey.

My heartfelt thanks go to **Rokas Jutas, Claudia Gollner, Audrius Pugžlys**, and everyone at the Photonics Institute, TU Wien, Vienna, Austria, for their help in conducting experiments in their laboratory and for the insightful discussions that followed.

I would also like to thank all other individuals from ELI-ALPS who contributed to the success of this research, whether directly or indirectly.

Finally, I am deeply grateful to my beloved parents, my wife **Monika**, and my daughter **Anaisha**. Their constant support, encouragement, and patience over the years have been invaluable, and this achievement would not have been possible without them.

References

[1] H. Rubens and F. Kurlbaum. Anwendung der methode der reststrahlen zur prüfung des strahlungsgesetzes. *Annalen der Physik*, 310(4):649–666, 1901.

[2] Erik Bründermann, Heinz-Wilhelm Hübers, and Maurice Kimmitt. *Terahertz Techniques*, volume 151. Springer Berlin Heidelberg, 2012.

[3] Matthew C. Beard, Gordon M. Turner, and Charles A. Schmuttenmaer. Terahertz spectroscopy. *The Journal of Physical Chemistry B*, 106(29):7146–7159, 2002.

[4] Masayoshi Tonouchi. Cutting-edge thz technology. *Nat. Photonics*, 1:97–105, 2007.

[5] P.U. Jepsen, D.G. Cooke, and M. Koch. Terahertz spectroscopy and imaging – modern techniques and applications. *Laser & Photonics Reviews*, 5(1):124–166, 2011.

[6] Wai Lam Chan, Jason Deibel, and Daniel M. Mittleman. Imaging with terahertz radiation. *Reports on Progress in Physics*, 70(8):1325–1379, 2007.

[7] Gintaras Valušis, Alvydas Lisauskas, Hui Yuan, Wojciech Knap, and Hartmut G. Roskos. Roadmap of terahertz imaging 2021. *Sensors*, 21(12), 2021.

[8] A. Giles Davies, Edmund H. Linfield, Michael Pepper, and Stafford Withington. Terahertz astronomical telescopes and instrumentation. *Philosophical Transactions of the Royal Society A: Mathematical, Physical and Engineering Sciences*, 362(1815):395–402, 12 2003.

[9] Jing Li, Xianjin Deng, Yangmei Li, Jie Hu, Wei Miao, Changxing Lin, Jun Jiang, and Shengcai Shi. Terahertz science and technology in astronomy, telecommunications, and biophysics. *Research*, 8:0586, 2025.

[10] William R Loerop, Michael Shur, and Dwight L Woolard. *Terahertz Sensing Technology:Emerging Scientific Applications and Novel Device Concepts*, volume 2. River Edge, N.J: World Scientific, 1st edition, 2003.

[11] Jae-Sung Rieh. *Introduction*, pages 1–17. Springer International Publishing, Cham, 2021.

[12] Xiang Yang, Xiang Zhao, Ke Yang, Yueping Liu, Yu Liu, Weiling Fu, and Yang Luo. Biomedical applications of terahertz spectroscopy and imaging. *Trends in Biotechnology*, 34(10):810–824, 2016.

[13] Ch. Fattinger and D. Grischkowsky. Point source terahertz optics. *Applied Physics Letters*, 53(16):1480–1482, 1988.

[14] Yun-Shik Lee. *Principles of Terahertz Science and Technology*. Springer Publishing Company, Incorporated, 1st edition, 2008.

[15] B. B. Hu and M. C. Nuss. Imaging with terahertz waves. *Opt. Lett.*, 20(16):1716–1718, 1995.

[16] D. M. Mittleman, M. Gupta, M. Neelamani, R. G. Baraniuk, J. V. Rudd, and M. Koch. Recent advances in terahertz imaging. *Appl. Phys. B.*, 68:1085–1094, 1999.

[17] Wanli Tu, Shuncong Zhong, Yaochun Shen, and Atilla Incecik. Nondestructive testing of marine protective coatings using terahertz waves with stationary wavelet transform. *Ocean Engineering*, 111:582–592, 2016.

[18] Soufiene Krimi, Jens Klier, Joachim Jonuscheit, Georg von Freymann, Ralph Urbansky, and René Beigang. Highly accurate thickness measurement of multi-layered automotive paints using terahertz technology. *Applied Physics Letters*, 109(2):021105, 2016.

[19] D. M. Hailu and D. Saeedkia. *Applications of Terahertz Technology for Plastic Industry*. Boca Raton, CRC Press, Taylor & Francis Group, 2017.

[20] Christian Jördens and Martin Koch. Detection of foreign bodies in chocolate with pulsed terahertz spectroscopy. *Optical Engineering*, 47(3):037003, 2008.

[21] Young-Ki Lee, Sung-Wook Choi, Seong-Tae Han, Deog Hyun Woo, and Hyang Sook Chun. Detection of foreign bodies in foods using continuous wave terahertz imaging. *Journal of Food Protection*, 75(1):179–183, 2012.

[22] Kodo Kawase, Yuichi Ogawa, Yuuki Watanabe, and Hiroyuki Inoue. Non-destructive terahertz imaging of illicit drugs using spectral fingerprints. *Opt. Express*, 11(20):2549–2554, 2003.

[23] Steven R. Murrill, Eddie L. Jacobs, Steven K. Moyer, Carl E. Halford, Steven T. Griffin, Frank C. De Lucia, Douglas T. Petkie, and Charmaine C. Franck. Terahertz imaging system performance model for concealed-weapon identification. *Appl. Opt.*, 47(9):1286–1297, 2008.

[24] Yookyeong Carolyn Sim, Jae Yeon Park, Kang-Min Ahn, Chansik Park, and Joo-Hiuk Son. Terahertz imaging of excised oral cancer at frozen temperature. *Biomed. Opt. Express*, 4(8):1413–1421, 2013.

[25] Fritzi Töpfer, Sergey Dudorov, and Joachim Oberhammer. Millimeter-wave near-field probe designed for high-resolution skin cancer diagnosis. *IEEE Transactions on Microwave Theory and Techniques*, 63(6):2050–2059, 2015.

[26] A. A. Angeluts, A. V. Balakin, M. D. Mishchenko, I. A. Ozheredov, M. N. Prokopchuk, T. N. Saphonova, and A. P. Shkurinov. Application of THz reflectometry to eye cornea

hydration measurements. In *2016 41st International Conference on Infrared, Millimeter, and Terahertz waves (IRMMW-THz)*, 2016.

[27] Hichem Guerboukha, Kathirvel Nallappan, and Maksim Skorobogatiy. Toward real-time terahertz imaging. *Adv. Opt. Photon.*, 10(4):843–938, 2018.

[28] Mukesh Jewariya, Emmanuel Abraham, Takayuki Kitaguchi, Yoshiyuki Ohgi, Masa aki Minami, Tsutomu Araki, and Takeshi Yasui. Fast three-dimensional terahertz computed tomography using real-time line projection of intense terahertz pulse. *Opt. Express*, 21(2):2423–2433, 2013.

[29] L. Pálfalvi, J. A. Fülöp, Gy. Tóth, and J. Hebling. Evanescent-wave proton postaccelerator driven by intense THz pulse. *Phys. Rev. ST Accel. Beams*, 17:031301, 2014.

[30] Kenta Kitano, Nobuhisa Ishii, and Jiro Itatani. High degree of molecular orientation by a combination of THz and femtosecond laser pulses. *Phys. Rev. A*, 84:053408, 2011.

[31] Ronald Ulbricht, Euan Hendry, Jie Shan, Tony F. Heinz, and Mischa Bonn. Carrier dynamics in semiconductors studied with time-resolved terahertz spectroscopy. *Rev. Mod. Phys.*, 83:543–586, 2011.

[32] Ping-Keng Lu, Anuar de Jesus Fernandez Olvera, Deniz Turan, Tom Sebastian Seifert, Nezih Tolga Yardimci, Tobias Kampfrath, Sascha Preu, and Mona Jarrahi. Ultrafast carrier dynamics in terahertz photoconductors and photomixers: beyond short-carrier-lifetime semiconductors. *Nanophotonics*, 11(11):2661–2691, 2022.

[33] Hideki Hirori and Koichiro Tanaka. Nonlinear optical phenomena induced by intense single-cycle terahertz pulses. *IEEE Journal of Selected Topics in Quantum Electronics*, 19(1), 2013.

[34] Ryo Shimano, Shinichi Watanabe, and Ryusuke Matsunaga. Intense terahertz pulse-induced nonlinear responses in carbon nanotubes. *Journal of Infrared, Millimeter, and Terahertz Waves, Volume 33, Issue 8, pp.861-869*, 33:861–869, 2012.

[35] G. Imeshev, M. E. Fermann, K. L. Vodopyanov, M. M. Fejer, X. Yu, J. S. Harris, D. Bliss, and C. Lynch. High-power source of THz radiation based on orientation-patterned GaAs pumped by a fiber laser. *Opt. Express*, 14(10):4439–4444, 2006.

[36] F. Junginger, B. Mayer, C. Schmidt, O. Schubert, S. Mährlein, A. Leitenstorfer, R. Huber, and A. Pashkin. Nonperturbative interband response of a bulk InSb semiconductor driven off resonantly by terahertz electromagnetic few-cycle pulses. *Phys. Rev. Lett.*, 109:147403, 2012.

[37] Kai Zhong, Wei Shi, DeGang Xu, PengXiang Liu, YuYe Wang, JiaLin Mei, Chao Yan, ShiJie Fu, and JianQuan Yao. Optically pumped terahertz sources. *SCIENCE CHINA Technological Sciences*, 60(12):1801–1818, 2017.

[38] A. Sharma, Z. Tibai, and J. Hebling. Intense tera-hertz laser driven proton acceleration in plasmas. *Physics of Plasmas*, 23(6):063111, 2016.

[39] L. Pálfalvi, J. A. Fülöp, G. Almási, and J. Hebling. Novel setups for extremely high power single-cycle terahertz pulse generation by optical rectification. *Applied Physics Letters*, 92(17):171107, 2008.

[40] Peter Salén, Martina Basini, Stefano Bonetti, János Hebling, Mikhail Krasilnikov, Alexey Y. Nikitin, Georgii Shamuilov, Zoltán Tibai, Vitali Zhaunerchyk, and Vitaliy Goryashko. Matter manipulation with extreme terahertz light: Progress in the enabling THz technology. *Physics Reports*, 836-837:1–74, 2019.

[41] Liang Jie Wong, Arya Fallahi, and Franz X. Kärtner. Compact electron acceleration and bunch compression in THz waveguides. *Opt. Express*, 21(8):9792–9806, 2013.

[42] Emilio Nanni, Wenqian Huang, Koustuban Ravi, Arya Fallahi, Gustavo Moriena, R. Miller, and Franz Kärtner. Terahertz-driven linear electron acceleration. *Nature communications*, 6, 2015.

[43] Janos Hebling, József Fülöp, M. Mechler, L. Pálfalvi, C. Tőke, and Gabor Almasi. Optical manipulation of relativistic electron beams using THz pulses. *arXiv:05739*, 2011.

[44] E. R. Brown, F. W. Smith, and K. A. McIntosh. Coherent millimeter-wave generation by heterodyne conversion in low-temperature-grown GaAs photoconductors. *Journal of Applied Physics*, 73(3):1480–1484, 1993.

[45] S. Verghese, K. A. McIntosh, S. Calawa, W. F. Dinatale, E. K. Duerr, and K. A. Molvar. Generation and detection of coherent terahertz waves using two photomixers. *Applied Physics Letters*, 73(26):3824–3826, 1998.

[46] J. Mangeney, A. Merigault, N. Zerounian, P. Crozat, K. Blary, and J. F. Lampin. Continuous wave terahertz generation up to 2 THz by photomixing on ion-irradiated In0.53Ga0.47As at 1.55μm wavelengths. *Applied Physics Letters*, 91(24):241102, 2007.

[47] H.-W. Hübers, S. G. Pavlov, H. Richter, A. D. Semenov, L. Mahler, A. Tredicucci, H. E. Beere, and D. A. Ritchie. High-resolution gas phase spectroscopy with a distributed feedback terahertz quantum cascade laser. *Applied Physics Letters*, 89(6):061115, 2006.

[48] Thorsten Göbel, Dennis Stanze, Björn Globisch, Roman J. B. Dietz, Helmut Roehle, and Martin Schell. Telecom technology based continuous wave terahertz photomixing system with 105 decibel signal-to-noise ratio and 3.5 terahertz bandwidth. *Opt. Lett.*, 38(20):4197–4199, 2013.

[49] Hai Zhang, S. Sfarra, Jaskaran Saluja, Jeroen Peeters, Julien Fleuret, Yuxia Duan, N.P. Avdelidis, Henrique Fernandes, Clemente Ibarra-Castanedo, and Xavier Maldague. Non-destructive investigation of paintings on canvas by continuous wave terahertz imaging and flash thermography. *Journal of Nondestructive Evaluation*, 36, 2017.

[50] M. Hangyo, T. Nagashima, and S. Nashima. Spectroscopy by pulsed terahertz radiation. *Measurement Science and Technology*, 13(11):1727–1738, 2002.

[51] X. Ropagnol, M. Khorasaninejad, M. Raeiszadeh, S. Safavi-Naeini, M. Bouvier, C. Y. Côté, A. Laramée, M. Reid, M. A. Gauthier, and T. Ozaki. Intense THz pulses with large ponderomotive potential generated from large aperture photoconductive antennas. *Opt. Express*, 24(11):11299–11311, 2016.

[52] Anastasios D Koulouklidis, Claudia Gollner, Valentina Shumakova, Vladimir Yu Fedorov, Audrius Pugžlys, Andrius Baltuška, and Stelios Tzortzakis. Observation of extremely efficient terahertz generation from mid-infrared two-color laser filaments. *Nature Communications*, 11(1):292, 2020.

[53] A. Stathopulos, S. Skupin, B. Zhou, P. U. Jepsen, and L. Bergé. Waveshape of terahertz radiation produced by two-color laser-induced air plasmas. *Phys. Rev. Res.*, 6:043274, 2024.

[54] T. I. Oh, Y. J. Yoo, Y. S. You, and K. Y. Kim. Generation of strong terahertz fields exceeding 8 MV/cm at 1 kHz and real-time beam profiling. *Applied Physics Letters*, 105(4):041103, 2014.

[55] Mark D. Thomson, Volker Blank, and Hartmut G. Roskos. Terahertz white-light pulses from an air plasma photo-induced by incommensurate two-color optical fields. *Opt. Express*, 18(22):23173–23182, 2010.

[56] K. Y. Kim, A. J. Taylor, J. H. Glownia, and G. Rodriguez. Coherent control of terahertz supercontinuum generation in ultrafast laser–gas interactions. *Nature Photonics*, 2(10):605–609, 2008.

[57] François Blanchard, Gargi Sharma, Xavier Ropagnol, Luca Razzari, and T. Ozaki. Improved terahertz two-color plasma sources pumped by high intensity laser beam. *Optics Express*, 17:6044–6052, 2009.

[58] A. Gopal, S. Herzer, A. Schmidt, P. Singh, A. Reinhard, W. Ziegler, D. Brömmel, A. Karmakar, P. Gibbon, U. Dillner, T. May, H-G. Meyer, and G. G. Paulus. Observation of gigawatt-class THz pulses from a compact laser-driven particle accelerator. *Phys. Rev. Lett.*, 111:074802, 2013.

[59] Xiaojun Wu, Deyin Kong, Sibo Hao, Yushan Zeng, Xieqiu Yu, Baolong Zhang, Mc Dai, Shaojie Liu, Jiaqi Wang, Zejun Ren, Sai Chen, Jianhua Sang, Kang Wang, Dongdong Zhang, Zhongkai Liu, Jiayan Gui, Xiaojun Yang, Yi Xu, and Ruxin Li. Generation of 13.9-mJ terahertz radiation from lithium niobate materials. *Advanced materials*, 35, 2023.

[60] L. Guiramand, J. E. Nkeck, X. Ropagnol, T. Ozaki, and F. Blanchard. 1.3% conversion efficiency terahertz source based on lithium niobate pumped by sub-millijoule ytterbium laser. In *Optica High-brightness Sources and Light-driven Interactions Congress*, 2022.

[61] K. Ravi, W. R. HuangB., S. Carbajo, X. Wu, and F. K. Limitations to THz generation by optical rectification using tilted pulse fronts. *Opt. Express*, 22(17):20239–20251, 2014.

[62] József András Fülöp, Stelios Tzortzakis, and Tobias Kampfrath. Laser-driven strong-field terahertz sources. *Advanced Optical Materials*, 8:1900681, 2020.

[63] J. A. Fülöp, L. Pálfalvi, and G. Almásiand J. Hebling. Design of high-energy terahertz sources based on optical rectification. *Opt. Express*, 18(12):12311–12327, 2010.

[64] L. Wang, T. Kroh, N. H. Matlis, and F. Kartner. Full 3d+1 modeling of tilted-pulse-front setups for single-cycle terahertz generation. *J. Opt. Soc. Am. B*, 37(4):1000–1007, 2020.

[65] Gy. Polónyi, B. Monoszlai, G. Gäumann, E. J. Rohwer, G. Andriukaitis, T. Balciunas, A. Pugzlys, A. Baltuska, T. Feurer, J. Hebling, and J. A. Fülöp. High-energy terahertz pulses from semiconductors pumped beyond the three-photon absorption edge. *Opt. Express*, 24(21):23872–23882, 2016.

[66] Jia Xu, Björn Globisch, Christina Hofer, Nikolai Lilienfein, Thomas Butler, Nicholas Karpowicz, and Ioachim Pupeza. Three-octave terahertz pulses from optical rectification of 20-fs, 1-μm, 78-MHz pulses in GaP. *Journal of Physics B: Atomic, Molecular and Optical Physics*, 51, 2018.

[67] F. Blanchard, B. E. Schmidt, X. Ropagnol, N. Thiré, T. Ozaki, R. Morandotti, D. G. Cooke, and F. Légaré. Terahertz pulse generation from bulk GaAs by a tilted-pulse-front excitation at 1.8 μm. *Applied Physics Letters*, 105(24):241106, 2014.

[68] Xiaodong Mu, Ioulia B. Zotova, and Yujie J. Ding. Power scaling on efficient generation of ultrafast terahertz pulses. *IEEE Journal of Selected Topics in Quantum Electronics*, 14(2):315–332, 2008.

[69] J. A. Fülöp, Gy. Polónyi, B. Monoszlai, G. Andriukaitis, T. Balciunas, A. Pugzlys, G. Arthur, A. Baltuska, and J. Hebling. Highly efficient scalable monolithic semiconductor terahertz pulse source. *Optica*, 3(10):1075–1078, 2016.

[70] Darren Kraemer, Michael L. Cowan, Renzhong Hua, Kresimir Franjic, and R. J. Dwayne Miller. High-power femtosecond infrared laser source based on noncollinear optical parametric chirped pulse amplification. *J. Opt. Soc. Am. B*, 24(4):813–818, 2007.

[71] Giedrius Andriukaitis, Tadas Balčiūnas, Skirmantas Ališauskas, Audrius Pugžlys, Andrius Baltuška, Tenio Popmintchev, Ming-Chang Chen, Margaret M. Murnane, and Henry C. Kapteyn. 90 GW peak power few-cycle mid-infrared pulses from an optical parametric amplifier. *Opt. Lett.*, 36(15):2755–2757, 2011.

[72] D. Sanchez, M. Hemmer, M. Baudisch, S. L. Cousin, K. Zawilski, P. Schunemann, O. Chalus, C. Simon-Boisson, and J. Biegert. 7 μm, ultrafast, sub-millijoule-level mid-infrared optical parametric chirped pulse amplifier pumped at 2 μm. *Optica*, 3(2):147–150, 2016.

[73] X.-C. Zhang, X. F. Ma, Y. Jin, T.-M. Lu, E. P. Boden, P. D. Phelps, K. R. Stewart, and C. P. Yakymyshyn. Terahertz optical rectification from a nonlinear organic crystal. *Applied Physics Letters*, 61:3080, 1992.

[74] Mojca Jazbinsek, Uros Puc, Andreja Abina, and Aleksander Zidansek. Organic crystals for THz photonics. *Applied Sciences*, 9:882, 2019.

[75] Takashi Notake, Masahiro Takeda, Shuji Okada, Takuya Hosobata, Yutaka Yamagata, and Hiroaki Minamide. Characterization of all second-order nonlinear-optical coefficients of organic N-benzyl-2-methyl-4-nitroaniline crystal. *Scientific Reports*, 9:14853, 2019.

[76] C. Vicario, A. V. Ovchinnikov, S. I. Ashitkov, M. B. Agranat, V. E. Fortov, and C. P. Hauri. Generation of 0.9-mJ THz pulses in DSTMS pumped by a Cr:Mg_2SiO_4 laser. *Optics Letters*, 39:6632, 2014.

[77] Mostafa Shalaby and Christoph P Hauri. Demonstration of a low-frequency three-dimensional terahertz bullet with extreme brightness. *Nature Communications*, 6:5976, 2015.

[78] Claudia Gollner, Mostafa Shalaby, Corinne Brodeur, Ignas Astrauskas, Rokas Jutas, Evan Constable, Lorenz Bergen, Andrius Baltuška, and Audrius Pugžlys. Highly efficient THz generation by optical rectification of mid-IR pulses in DAST. *APL Photonics*, 6(4):046105, 2021.

[79] Zachary B. Zaccardi, Isaac C. Tangen, Gabriel A. Valdivia-Berroeta, Charles B. Bahr, Karissa C. Kenney, Claire Rader, Matthew J. Lutz, Brittan P. Hunter, David J. Michaelis, and Jeremy A. Johnson. Enabling high-power, broadband THz generation with 800-nm pump wavelength. *Optics Express*, 29:38084, 2021.

[80] Samira Mansourzadeh, Tim Vogel, Alan Omar, Mostafa Shalaby, Mirko Cinchetti, and Clara J. Saraceno. Broadband, high power THz source at 540 kHz using organic crystal BNA. *APL Photonics*, 8:011301, 2023.

[81] Pierre Meystre. *Light-Matter Interaction*, pages 997–1007. Springer New York, New York, NY, 2006.

[82] R. W. Boyd. *Nonlinear Optics*. Academic Press, Amsterdam; Boston, 2008.

[83] P. A. Franken, A. E. Hill, C. W. Peters, and G. Weinreich. Generation of optical harmonics. *Phys. Rev. Lett.*, 7:118–119, 1961.

[84] M. Bass, P. A. Franken, J. F. Ward, and G. Weinreich. Optical rectification. *Phys. Rev. Lett.*, 9:446–448, 1962.

[85] A. Rice, Y. Jin, X. F. Ma, X.-C. Zhang, D. Bliss, J. Larkin, and M. Alexander. Terahertz optical rectification from $\langle 110 \rangle$ zinc-blende crystals. *Applied Physics Letters*, 64(11):1324–1326, 1994.

[86] Konstantin L. Vodopyanov. Optical generation of narrow-band terahertz packets in periodically-inverted electro-optic crystals: conversion efficiency and optimal laser pulse format. *Opt. Express*, 14(6):2263–2276, 2006.

[87] Hassan Hafez, Xin Chai, Akram Ibrahim, Sudipta Mondal, Denis Ferachou, Xavier Ropagnol, and T Ozaki. Intense terahertz radiation and their applications. *Journal of Optics*, 18:093004, 2016.

[88] Eric W. Van Stryland and David J. Hagan. Nonlinear absorption. In Craig Hoffman and Ronald Driggers, editors, *Encyclopedia of Optical and Photonic Engineering*, pages 1–7. CRC Press, Boca Raton, FL, 2nd edition, 2015.

[89] Yao Lu, Yibo Huang, Junkai Cheng, Ruobin Ma, Xitan Xu, Yijia Zang, Qiang Wu, and Jingjun Xu. Nonlinear optical physics at terahertz frequency. *Nanophotonics*, 13(18):3279–3298, 2024.

[90] János Hebling, Ka-Lo Yeh, Matthias C. Hoffmann, Balázs Bartal, and Keith A. Nelson. Generation of high-power terahertz pulses by tilted-pulse-front excitation and their application possibilities. *J. Opt. Soc. Am. B*, 25(7):B6–B19, 2008.

[91] Matthias C Hoffmann and József András Fülöp. Intense ultrashort terahertz pulses: generation and applications. *Journal of Physics D: Applied Physics*, 44:083001, 2011.

[92] W. Kuehn, P. Gaal, K. Reimann, M. Woerner, T. Elsaesser, and R. Hey. Terahertz-induced interband tunneling of electrons in gaas. *Phys. Rev. B*, 82:075204, 2010.

[93] J. A. Fülöp, Z. Ollmann, Cs. Lombosi, C. Skrobol, S. Klingebiel, L. Pálfalvi, F. Krausz, S. Karsch, and J. Hebling. Efficient generation of THz pulses with 0.4 mJ energy. *Opt. Express*, 22(17):20155–20163, 2014.

[94] S. Kirkpatrick R.L. Sutherland, D.G. McLean. *Handbook of nonlinear optics*. CRC Press, Boca Raton, 2003.

[95] J. Li, R. Rana, L. G. Zhu, C. L. Liu, H. Schneider, and A. Pashkin. Thz conversion efficiency in dstms limited by high-order nonlinearities. In *2021 46th International Conference on Infrared, Millimeter and Terahertz Waves (IRMMW-THz)*, pages 1–2, 2021.

[96] Matthias C. Hoffmann, Ka-Lo Yeh, János Hebling, and Keith A. Nelson. Efficient terahertz generation by optical rectification at 1035 nm. *Opt. Express*, 15(18):11706–11713, 2007.

[97] Toshiaki Hattori and Kousuke Takeuchi. Simulation study on cascaded terahertz pulse generation in electro-optic crystals. *Opt. Express*, 15(13):8076–8093, 2007.

[98] Mukesh Jewariya, Masaya Nagai, and Koichiro Tanaka. Enhancement of terahertz wave generation by cascaded χ^2 processes in $LiNbO_3$. *J. Opt. Soc. Am. B*, 26(9):A101–A106, 2009.

[99] D. H. Auston, K. P. Cheung, J. A. Valdmanis, and D. A. Kleinman. Cherenkov radiation from femtosecond optical pulses in electro-optic media. *Phys. Rev. Lett.*, 53:1555–1558, 1984.

[100] János Hebling, Gábor Almási, Ida Z. Kozma, and Jürgen Kuhl. Velocity matching by pulse front tilting for large-area THz-pulse generation. *Opt. Express*, 10(21):1161–1166, 2002.

[101] J. Hebling, A. G. Stepanov, G. Almási, B. Bartal, and J. Kuhl. Tunable THz pulse generation by optical rectification of ultrashort laser pulses with tilted pulse fronts. *Applied Physics B: Lasers and Optics*, 78(5):593–599, 2004.

[102] J. A. Armstrong, N. Bloembergen, J. Ducuing, and P. S. Pershan. Interactions between light waves in a nonlinear dielectric. *Phys. Rev.*, 127:1918–1939, 1962.

[103] G. D. Boyd, A. Ashkin, J. M. Dziedzic, and D. A. Kleinman. Second-harmonic generation of light with double refraction. *Phys. Rev.*, 137:A1305–A1320, 1965.

[104] L. E. Myers, G. D. Miller, R. C. Eckardt, M. M. Fejer, R. L. Byer, and W. R. Bosenberg. Quasi-phase-matched 1.064-μm-pumped optical parametric oscillator in bulk periodically poled $LiNbO_3$. *Opt. Lett.*, 20(1):52–54, 1995.

[105] L. E. Myers, R. C. Eckardt, M. M. Fejer, R. L. Byer, W. R. Bosenberg, and J. W. Pierce. Quasi-phase-matched optical parametric oscillators in bulk periodically poled $LiNbO_3$. *J. Opt. Soc. Am. B*, 12(11):2102–2116, 1995.

[106] Joel Edouard Nkeck, Xavier Ropagnol, Riad Nechache, and François Blanchard. Electro-optical detection of terahertz radiation in a zinc sulphide crystal at a wavelength of 512 nm. *Applied Physics Express*, 13(11):112007, 2020.

[107] Xu Xie, Jingzhou Xu, and X.-C. Zhang. Terahertz wave generation and detection from a CdTe crystal characterized by different excitation wavelengths. *Opt. Lett.*, 31(7):978–980, 2006.

[108] O. Hatem. Optimizing the electro-optic detection of terahertz waves by ZnTe at 780 and 1560-nm probe-beam wavelengths. *Journal of Nonlinear Optical Physics & Materials*, 27(04):1850043, 2018.

[109] Yun-Shik Lee. *Principles of Terahertz Science and Technology*. Springer New York, NY, 2009.

[110] Masaya Nagai, Koichiro Tanaka, Hideyuki Ohtake, Toshiaki Bessho, Toshiharu Sugiura, Tomoya Hirosumi, and Makoto Yoshida. Generation and detection of terahertz radiation by electro-optical process in GaAs using 1.56 μm fiber laser pulses. *Applied Physics Letters*, 85(18):3974–3976, 2004.

[111] G. Gallot, Jiangquan Zhang, R. W. McGowan, Tae-In Jeon, and D. Grischkowsky. Measurements of the THz absorption and dispersion of znte and their relevance to the electro-optic detection of THz radiation. *Applied Physics Letters*, 74(23):3450–3452, 1999.

[112] János Hebling. Derivation of the pulse front tilt caused by angular dispersion. *Optical and Quantum Electronics*, 28:1759–1763, 1996.

[113] Gyorgy Toth, Gyula Polonyi, and Janos Hebling. Tilted pulse front pumping techniques for efficient terahertz pulse generation. *Photonics and Nanostructures - Fundamentals and Applications*, 12, 2023.

[114] Ki Young Kim. *Recent Optical and Photonic Technologies*. IntechOpen, London, 2010.

[115] O. E. Martinez, J. P. Gordon, and R. L. Fork. Negative group-velocity dispersion using refraction. *J. Opt. Soc. Am. A*, 1(10):1003–1006, 1984.

[116] J.-C. Diels and W. Rudolph. *Ultrashort Laser Pulse Phenomena: Fundamentals, Techniques, and Applications on a Femtosecond Time Scale*. Optics & Photonics Series. Elsevier / Academic Press, Amsterdam; Boston, 2nd edition, 2006.

[117] Andrei G. Stepanov, János Hebling, and Jürgen Kuhl. Efficient generation of subpicosecond terahertz radiation by phase-matched optical rectification using ultrashort laser pulses with tilted pulse fronts. *Applied Physics Letters*, 83(15):3000–3002, 2003.

[118] A. G. Stepanov, J. Kuhl, I. Z. Kozma, E. Riedle, G. Almási, and J. Hebling. Scaling up the energy of THz pulses created by optical rectification. *Opt. Express*, 13(15):5762–5768, 2005.

[119] K.-L. Yeh, M. C. Hoffmann, J. Hebling, and Keith A. Nelson. Generation of 10μJ ultrashort terahertz pulses by optical rectification. *Applied Physics Letters*, 90(17):171121, 2007.

[120] Andrei G. Stepanov, Luigi Bonacina, Sergei V. Chekalin, and Jean-Pierre Wolf. Generation of 30 μJ single-cycle terahertz pulses at 100 Hz repetition rate by optical rectification. *Opt. Lett.*, 33(21):2497–2499, 2008.

[121] A. G. Stepanov, S. Henin, Y. Petit, L. Bonacina, J. Kasparian, and J.-P. Wolf. Mobile source of high-energy single-cycle terahertz pulses. *Applied Physics B*, 101(1-2):11–14, 2010.

[122] H. Hirori, A. Doi, F. Blanchard, and K. Tanaka. Single-cycle terahertz pulses with amplitudes exceeding 1MV/cm generated by optical rectification in $LiNbO_3$. *Applied Physics Letters*, 98(9):091106, 2011.

[123] Mohsen Sajadi, Martin Wolf, and Tobias Kampfrath. Terahertz-field-induced optical birefringence in common window and substrate materials. *Opt. Express*, 23(22):28985–28992, 2015.

[124] J. A. Fülöp, L. Pálfalvi, S. Klingebiel, G. Almási, F. Krausz, S. Karsch, and J. Hebling. Generation of sub-mj terahertz pulses by optical rectification. *Opt. Lett.*, 37(4):557–559, 2012.

[125] Xiao jun Wu, Jing long Ma, Bao long Zhang, Shu su Chai, Zhao ji Fang, Chen-Yi Xia, De yin Kong, Jin guang Wang, Hao Liu, Chang-Qing Zhu, Xuan Wang, Cun-Jun Ruan, and Yu-Tong Li. Highly efficient generation of 0.2 mJ terahertz pulses in lithium niobate at room temperature with sub-50 fs chirped ti:sapphire laser pulses. *Opt. Express*, 26(6):7107–7116, 2018.

[126] Q. Wu and X.-C. Zhang. Ultrafast electro-optic field sensors. *Applied Physics Letters*, 68(12):1604–1606, 1996.

[127] Jae-Hyeok Jeong, Bongjoo Kang, Ji-Soo Kim, Mojca Jazbinsek, Seung-Heon Lee, Seung-Chul Lee, In Hyung Baek, Hoseop Yun, Jongtaek Kim, Yoon Lee, Jae-Hyeok Lee, Jae-Ho Kim, Fabian Rotermund, and O-Pil Kwon. High-power broadband organic THz generator. *Scientific reports*, 3:3200, 2013.

[128] C. Vicario, M. Jazbinsek, A. V. Ovchinnikov, O. V. Chefonov, S. I. Ashitkov, M. B. Agranat, and C. P. Hauri. High efficiency THz generation in DSTMS, DAST and OH1 pumped by Cr:forsterite laser. *Opt. Express*, 23(4):4573–4580, 2015.

[129] Hang Zhao, Yong Tan, Chen Wang, Ming Liu, Yongzheng Wen, Yuejin Zhao, and Ji Zhou. Extremely efficient terahertz second-harmonic generation from organic crystals. *Advanced Photonics Nexus*, 3, 2024.

[130] Anton S. Sinko, I. A. Ozheredov, Elena B. Rudneva, Vera L. Manomenova, Natalia Kozlova, Natalia A. Lobova, Alexey E. Voloshin, Jean-Louis Coutaz, and Alexander P Shkurinov. Perspective on terahertz applications of molecular crystals. *Electronics*, 2022.

[131] G. D. Boyd, T. J. Bridges, M. A. Pollack, and E. H. Turner. Microwave nonlinear susceptibilities due to electronic and ionic anharmonicities in acentric crystals. *Phys. Rev. Lett.*, 26:387–390, 1971.

[132] D. T. F. Marple. Refractive Index of ZnSe, ZnTe, and CdTe. *Journal of Applied Physics*, 35(3):539–542, 1964.

[133] M. Schall, M. Walther, and P. Uhd Jepsen. Fundamental and second-order phonon processes in CdTe and ZnTe. *Phys. Rev. B*, 64:094301, 2001.

[134] R. E. Nahory and H. Y. Fan. Optical properties of zinc telluride. *Phys. Rev.*, 156:825–833, 1967.

[135] Edward D. Palik, editor. *Handbook of Optical Constants of Solids*, volume 1. Academic Press, 1985.

[136] D. F. Nelson and E. H. Turner. Electro-optic and piezoelectric coefficients and refractive index of gallium phosphide. *Journal of Applied Physics*, 39(7):3337–3343, 1968.

[137] George D. Clark and Nick Holonyak. Optical properties of gallium arsenide-phosphide. *Phys. Rev.*, 156:913–924, 1967.

[138] D.H. Jundt, M.M. Fejer, and R.L. Byer. Optical properties of lithium-rich lithium niobate fabricated by vapor transport equilibration. *IEEE Journal of Quantum Electronics*, 26(1):135–138, 1990.

[139] Michael Schall, Hanspeter Helm, and S. Keiding. Far infrared properties of electro-optic crystals measured by THz time-domain spectroscopy. *International Journal of Infrared and Millimeter Waves*, 20:595–604, 1999.

[140] D. Redfield and W. J. Burke. Optical absorption edge of LiNbO3. *Journal of Applied Physics*, 45(10):4566–4571, 1974.

[141] Masazumi Fujiwara, Minoru Maruyama, Mitsuru Sugisaki, Hironori Takahashi, Shin ichiro Aoshima, Richard J. Cogdell, and Hideki Hashimoto. Determination of the d-tensor components of a single crystal of n-benzyl-2-methyl-4-nitroaniline. *Japanese Journal of Applied Physics*, 46:1528, 2007.

[142] Katsuhiko Miyamoto, Seigo Ohno, Masazumi Fujiwara, Hiroaki Minamide, Hideki Hashimoto, and Hiromasa Ito. Optimized terahertz-wave generation using BNA-DFG. *Opt. Express*, 17(17):14832–14838, 2009.

[143] Abhishek Gupta, Tianmiao Zhang, Veronika Hanyecz, János Bohus, Vineet Gupta, Ashutosh Sharma, and József András Fülöp. Two-photon absorption and its saturation in organic terahertz-generator crystals. *Opt. Mater. Express*, 15(8):2056–2065, 2025.

[144] R. T. Bailey, G. Bourhill, F. R. Cruickshank, D. Pugh, J. N. Sherwood, and G. S. Simpson. The linear and nonlinear optical properties of the organic nonlinear material 4-nitro-4'-methylbenzylidene aniline. *Japanese Journal of Applied Physics*, 73:1591, 1993.

[145] Daisy JH Ludlow, Bruce Wayne H Palmer, Natalie K Green, Sin-Hang Enoch Ho, Coriantumr Z Wayment, Brenan M Kelleher, Connor D Barlow, Olivia N Rollans, Brittan P Hunter, Claire Rader, et al. Intense THz generation with new organic NLO crystal NMBA. *Advanced Optical Materials*, 12:2302402, 2024.

[146] C. H. Grossman and A. F. Garito. Brewster angle method for refractive index measurements of biaxial organic systems. *Molecular Crystals and Liquid Crystals*, 168:255, 1989.

[147] Bruce Wayne H Palmer, Claire Rader, Enoch Sin-Hang Ho, Zachary B Zaccardi, Daisy J Ludlow, Natalie K Green, Matthew J Lutz, Aldair Alejandro, Megan F Nielson, Gabriel A Valdivia-Berroeta, et al. Large crystal growth and THz generation properties of 2-amino-5-nitrotoluene (MNA). *ACS Applied Electronic Materials*, 4:4316, 2022.

[148] B. F. Levine, C. G. Bethea, C. D. Thurmond, R. T. Lynch, and J. L. Bernstein. An organic crystal with an exceptionally large optical second-harmonic coefficient: 2-methyl-4-nitroaniline. *Journal of Applied Physics*, 50:2523, 1979.

[149] F. Pan, G. Knöpfle, Ch. Bosshard, S. Follonier, R. Spreiter, M. S. Wong, and P. Günter. Electro-optic properties of the organic salt 4-n,n-dimethylamino-4′-n′-methyl-stilbazolium tosylate. *Applied Physics Letters*, 69(1):13–15, 1996.

[150] Paul D. Cunningham and L. Michael Hayden. Optical properties of DAST in the THz range. *Opt. Express*, 18(23):23620–23625, 2010.

[151] R. S. Weis and T. K. Gaylord. Lithium niobate: Summary of physical properties and crystal structure. *Applied Physics A: Materials Science & Processing*, 37(4):191–203, 1985.

[152] A. Kling, J.G. Marques, J.G. Correia, M.F. da Silva, E. Diéguez, F. Agulló-López, and J.C. Soares. Study of structural differences between stoichiometric and congruent lithium niobate. *Nuclear Instruments and Methods in Physics Research Section B: Beam Interactions with Materials and Atoms*, 113(1):293–295, 1996.

[153] T. Fujiwara, M. Takahashi, M. Ohama, {A. J.} Ikushima, Y. Furukawa, and K. Kitamura. Comparison of electro-optic effect between stoichiometric and congruent $LiNbO_3$. *Electronics Letters*, 35(6):499–501, 1999.

[154] K. Kitamura, Y. Furukawa, Y. Ji, M. Zgonik, C. Medrano, G. Montemezzani, and P. Günter. Photorefractive effect in $LiNbO_3$ crystals enhanced by stoichiometry control. *Journal of Applied Physics*, 82(3):1006–1009, 1997.

[155] Y. Furukawa, K. Kitamura, S. Takekawa, A. Miyamoto, M. Terao, and N. Suda. Photorefraction in $LiNbO_3$ as a function of [Li]/[Nb] and MgO concentrations. *Applied Physics Letters*, 77(16):2494–2496, 2000.

[156] Masaru Nakamura, Shinji Higuchi, Shunji Takekawa, Kazuya Terabe, Yasunori Furukawa, and Kenji Kitamura. Optical damage resistance and refractive indices in near-stoichiometric MgO-doped $LiNbO_3$. *Japanese Journal of Applied Physics*, 41, 2002.

[157] D. A. Bryan, Robert Gerson, and H. E. Tomaschke. Increased optical damage resistance in lithium niobate. *Applied Physics Letters*, 44(9):847–849, 1984.

[158] L. Pálfalvi, Janos Hebling, J. Kuhl, A. Peter, and Katalin Polgár. Temperature dependence of the absorption and refraction of Mg-doped congruent and stoichiometric $LiNbO_3$ in the THz range. *Journal of Applied Physics*, 97:123505–123505, 2005.

[159] Dieter H. Jundt. Temperature-dependent sellmeier equation for the index of refraction, n_e, in congruent lithium niobate. *Opt. Lett.*, 22(20):1553–1555, 1997.

[160] O. Gayer, Z. Sacks, E. Galun, and Ady Arie. Temperature and wavelength dependent refractive index equations for MgO-doped congruent and stoichiometric $LiNbO_3$. *Applied Physics B: Lasers and Optics*, 91:343–348, 2008.

[161] B. Bartal, I.Z. Kozma, A.G. Stepanov, Gabor Almasi, J. Kuhl, Eberhard Riedle, and Janos Hebling. Toward generation of μJ range sub-ps THz pulses by optical rectification. *Applied Physics B*, 86:419–423, 2007.

[162] K. H. Yang, P. L. Richards, and Y. R. Shen. Generation of far-infrared radiation by picosecond light pulses in $LiNbO_3$. *Applied Physics Letters*, 19(9):320–323, 1971.

[163] Xiaojun Wu, Chun Zhou, Wenqian Ronny Huang, Frederike Ahr, and Franz X. Kärtner. Temperature dependent refractive index and absorption coefficient of congruent lithium niobate crystals in the terahertz range. *Opt. Express*, 23(23):29729–29737, 2015.

[164] L. Pálfalvi, J. Hebling, G. Almási, Á. Péter, K. Polgár, K. Lengyel, and R. Szipöcs. Nonlinear refraction and absorption of Mg doped stoichiometric and congruent $LiNbO_3$. *Journal of Applied Physics*, 95(3):902–908, 2004.

[165] József András Fülöp, László Pálfalvi, Matthias C. Hoffmann, and János Hebling. Towards generation of mJ-level ultrashort THz pulses by optical rectification. *Opt. Express*, 19(16):15090–15097, 2011.

[166] Maksim Kunitski, Martin Richter, Mark Thomson, Arno Vredenborg, Jian Wu, Till Jahnke, Markus Schöffler, Horst Schmidt-Böcking, Hartmut Roskos, and Reinhard Dörner. Optimization of single-cycle terahertz generation in $LiNbO_3$ for sub-50 femtosecond pump pulses. *Optics Express*, 21:6826–6836, 2013.

[167] Zoltán Ollmann, Janos Hebling, and Gabor Almasi. Design of a contact grating setup for mJ-energy THz pulse generation by optical rectification. *Applied Physics B*, 108, 2012.

[168] Masaaki Tsubouchi, Keisuke Nagashima, Fumiko Yoshida, Yoshihiro Ochi, and Momoko Maruyama. Contact grating device with fabry-perot resonator for effective terahertz light generation. *Opt. Lett.*, 39(18):5439–5442, 2014.

[169] Michael I. Bakunov and Sergey B. Bodrov. Terahertz generation with tilted-front laser pulses in a contact-grating scheme. *J. Opt. Soc. Am. B*, 31(11):2549–2557, 2014.

[170] L. Pálfalvi, Z. Ollmann, L. Tokodi, and J. Hebling. Hybrid tilted-pulse-front excitation scheme for efficient generation of high-energy terahertz pulses. *Opt. Express*, 24(8):8156–8169, 2016.

[171] László Pálfalvi, György Tóth, Levente Tokodi, Zsuzsanna Márton, József András Fülöp, Gábor Almási, and János Hebling. Numerical investigation of a scalable setup for efficient terahertz generation using a segmented tilted-pulse-front excitation. *Opt. Express*, 25(24):29560–29573, 2017.

[172] Priyo Syamsul Nugraha, Gergő Krizsán, Csaba Lombosi, László Pálfalvi, György Tóth, Gábor Almási, József András Fülöp, and János Hebling. Demonstration of a tilted-pulse-front pumped plane-parallel slab terahertz source. *Opt. Lett.*, 44:1023–1026, 2019.

[173] Fangjie Li, Kai Zhong, Yiwen Zhang, Tong Wu, Yuxin Liu, Hongzhan Qiao, Jining Li, Degang Xu, and Jianquan Yao. Optical rectification in 4H-SiC: paving the way to generate strong terahertz fields with ultra-wide bandwidth. *High Power Laser Science and Engineering*, 11, 2023.

[174] Gilles Dalla-Barba, Gaëtan Jargot, Philippe Lassonde, Szabolcs Tóth, Elissa Haddad, Fabio Boschini, Jean-Christophe Delagnes, Adrien Leblanc, Heide Ibrahim, Eric Cormier, and François Légaré. Mid-infrared frequency domain optical parametric amplifier. *Opt. Express*, 31(9):14954–14964, 2023.

[175] David Heydari, Mircea Cătuneanu, Edwin Ng, Dodd J. Gray, Ryan Hamerly, Jatadhari Mishra, Marc Jankowski, M. M. Fejer, Kambiz Jamshidi, and Hideo Mabuchi. Degenerate optical parametric amplification in CMOS silicon. *Optica*, 10(4):430–437, 2023.

[176] M. Missous. 16 - semiconductor material development for terahertz applications. In Daryoosh Saeedkia, editor, *Handbook of Terahertz Technology for Imaging, Sensing and Communications*, Woodhead Publishing Series in Electronic and Optical Materials, pages 464–489. Woodhead Publishing, 2013.

[177] Mohammad Javad Mohammad-Zamani. THz power optimization and analysis of plasmonic unbiased photoconductive THz emitters coupled to a spiral-like dipole antenna. *J. Opt. Soc. Am. B*, 37(11):3213–3221, 2020.

[178] Mohammad Bashirpour, Saeed Khankalantary, and Mohsen Hajizadeh. A new hybrid metasurface design for performance improvement of thin film unbiased terahertz photoconductive source. *Optik*, 246:167817, 2021.

[179] Shyamal Mondal, Nisha Flora Boby Edwin, and Vaisshale Rathinasamy. Interdigitated photoconductive antenna for efficient terahertz generation and detection. In Borwen You and Ja-Yu Lu, editors, *Terahertz Technology*, chapter 9. IntechOpen, London, 2022.

[180] Salman Alfihed and Abdullah Alharbi. Broadband terahertz emission from photoconductive devices. In Mingbo Niu, editor, *Intelligent Electronics and Circuits - Terahertz, ITS, and Beyond*, chapter 1. IntechOpen, London, 2022.

[181] Vitali V. Kononenko, Vladimir V. Bukin, Maxim S. Komlenok, Evgeny V. Zavedeev, Taras V. Kononenko, Margarita A. Dezhkina, Pavel P. Ratnikov, Timophey V. Dolmatov, Pavel A. Chizhov, Alexander A. Ushakov, Vitaly I. Konov, and Sergey V. Garnov. A diamond terahertz large aperture photoconductive antenna biased by a longitudinal field. *Photonics*, 10(10), 2023.

[182] Ruobin Han, Abdoalbaset Abohmra, Tomas Pires, Joao Ponciano, Hasan Abbas, Akram Alomainy, Farooq Ahmad Tahir, Muhammad Imran, and Qammer Abbasi. Advancements in terahertz-enabled photoconductive antenna design: a review. *International Journal of Microwave and Wireless Technologies*, 17(6):977–993, 2025.

[183] D. You, R. R. Jones, P. H. Bucksbaum, and D. R. Dykaar. Generation of high-power sub-single-cycle 500-fs electromagnetic pulses. *Opt. Lett.*, 18(4):290–292, 1993.

[184] R. R. Jones, D. You, and P. H. Bucksbaum. Ionization of rydberg atoms by subpicosecond half-cycle electromagnetic pulses. *Phys. Rev. Lett.*, 70:1236–1239, 1993.

[185] X. Ropagnol, F. Blanchard, T. Ozaki, and M. Reid. Intense terahertz generation at low frequencies using an interdigitated ZnSe large aperture photoconductive antenna. *Applied Physics Letters*, 103(16):161108, 2013.

[186] A. Leitenstorfer, S. Hunsche, J. Shah, M. C. Nuss, and W. H. Knox. Detectors and sources for ultrabroadband electro-optic sampling: Experiment and theory. *Applied Physics Letters*, 74(11):1516–1518, 1999.

[187] Yaojun Du, Sung Sakong, and Peter Kratzer. As vacancies, ga antisites, and au impurities in zinc blende and wurtzite gaas nanowire segments from first principles. *Physical Review B*, 87:75308, 2013.

[188] F. Blanchard, L. Razzari, H.-C. Bandulet, G. Sharma, R. Morandotti, J.-C. Kieffer, T. Ozaki, M. Reid, H. F. Tiedje, H. K. Haugen, and F. A. Hegmann. Generation of 1.5 μJ single-cycle terahertz pulses by optical rectification from a large aperture ZnTe crystal. *Opt. Express*, 15(20):13212–13220, 2007.

[189] Shayne M. Harrel, Rebecca L. Milot, James M. Schleicher, and Charles A. Schmuttenmaer. Influence of free-carrier absorption on terahertz generation from ZnTe(110). *Journal of Applied Physics*, 107(3):033526, 2010.

[190] S. Vidal, J. Degert, M. Tondusson, J. Oberlé, and E. Freysz. Impact of dispersion, free carriers, and two-photon absorption on the generation of intense terahertz pulses in ZnTe crystals. *Applied Physics Letters*, 98(19):191103, 2011.

[191] W. L. Bond. Measurement of the refractive indices of several crystals. *Journal of Applied Physics*, 36(5):1674–1677, 1965.

[192] Qi Wu and Xi-Cheng Zhang. Design and characterization of traveling-wave electrooptic terahertz sensors. *IEEE Journal of Selected Topics in Quantum Electronics*, 2(3):693–700, 1996.

[193] Jia Xu, Björn Globisch, Christina Hofer, Nikolai Lilienfein, Thomas Butler, Nicholas Karpowicz, and Ioachim Pupeza. Three-octave terahertz pulses from optical rectification of 20 fs, 1 μm, 78 MHz pulses in GaP. *Journal of Physics B Atomic Molecular Physics*, 51(15):154002, 2018.

[194] Guoqing Chang, Charles J. Divin, Chi-Hung Liu, Steven L. Williamson, Almantas Galvanauskas, and Theodore B. Norris. Power scalable compact THz system based on an ultrafast Yb-doped fiber amplifier. *Opt. Express*, 14(17):7909–7913, 2006.

[195] Jiang Li, Lu Chai, Junkai Shi, Bowen Liu, Baozhong Xu, Minglie Hu, Yanfeng Li, Qirong Xing, Chingyue Wang, Andrey B. Fedotov, and Aleksei M. Zheltikov. Efficient terahertz wave generation from GaP crystals pumped by chirp-controlled pulses from femtosecond photonic crystal fiber amplifier. *Applied Physics Letters*, 104(3):031117, 2014.

[196] Anatoly R. Melnikov, Evgeny V. Kalneus, Yaroslav V. Getmanov, Darya A. Shevchenko, Vasily V. Gerasimov, Oleg A. Anisimov, Matvey V. Fedin, and Sergey L. Veber. Comparative study of single crystal and polymeric pyroelectric detectors in the 0.9–2.0 THz range using monochromatic laser radiation of the novofel. *Polymers*, 15(20), 2023.

[197] M. Hemmer, D. Sánchez, M. Jelínek, Vadim Smirnov, H. Jelinkova, V. Kubeček, and J. Biegert. 2-μm wavelength, high-energy ho:ylf chirped-pulse amplifier for mid-infrared opcpa. *Opt. Lett.*, 40(4):451–454, 2015.

[198] Konstantin Vodopyanov. Terahertz-wave generation with periodically inverted gallium arsenide. *Laser Physics*, 19:305–321, 2009.

[199] Wei Cui, Kashif Masud Awan, Rupert Huber, Ksenia Dolgaleva, and Jean-Michel Ménard. Broadband and high-sensitivity time-resolved THz system using grating-assisted tilted-pulse-front phase matching. *Advanced Optical Materials*, 10(1):2101136, 2022.

[200] W. Cui, E. K. Yalavarthi, A. V. Radhan, M. Bashirpour, A. Gamouras, and J. M. Ménard. High-field THz source centered at 2.6 THz. *Opt. Express*, 31(20):32468–32477, 2023.

[201] Timothy J. Carrig, G. Rodriguez, Tracy Sharp Clement, A. J. Taylor, and Kevin R. Stewart. Generation of terahertz radiation using electro-optic crystal mosaics. *Applied Physics Letters*, 66(1):10–12, 1995.

[202] John J. Carey, Ray T. Bailey, D. Pugh, J. N. Sherwood, F. R. Cruickshank, and Klaas Wynne. Terahertz pulse generation in an organic crystal by optical rectification and resonant excitation of molecular charge transfer. *Applied Physics Letters*, 81(23):4335, 2002.

[203] T. Taniuchi, S. Okada, and H. Nakanishi. Widely tunable terahertz-wave generation in an organic crystal and its spectroscopic application. *Journal of Applied Physics*, 95:5984, 2004.

[204] Arno Schneider, Max Neis, Marcel Stillhart, Blanca Ruiz, Rizwan UA Khan, and Peter Günter. Generation of terahertz pulses through optical rectification in organic DAST crystals: theory and experiment. *Journal of the Optical Society of America B*, 23:1822, 2006.

[205] Kazuyoshi Kuroyanagi, Masazumi Fujiwara, Hideki Hashimoto, Hironori Takahashi, Shin ichiro Aoshima, and Yutaka Tsuchiya. All organic terahertz electromagnetic wave emission and detection using highly purified N-benzyl-2-methyl-4-nitroaniline crystals. *Japanese Journal of Applied Physics*, 45:4068, 2006.

[206] Christoph P. Hauri, Clemens Ruchert, Carlo Vicario, and Fernando Ardana. Strong-field single-cycle THz pulses generated in an organic crystal. *Applied Physics Letters*, 99(16):161116, 2011.

[207] Clemens Ruchert, Carlo Vicario, and Christoph P. Hauri. Scaling submillimeter single-cycle transients toward megavolts per centimeter field strength via optical rectification in the organic crystal OH1. *Opt. Lett.*, 37(5):899–901, 2012.

[208] C. Vicario, B. Monoszlai, M. Jazbinsek, S.-H. Lee, O.-P. Kwon, and C. P. Hauri. Intense, carrier frequency and bandwidth tunable quasi single-cycle pulses from an organic emitter covering the terahertz frequency GaP. *Scientific Reports*, 5:14394, 2015.

[209] C Vicario, B Monoszlai, G Arisholm, and C P Hauri. Generation of 1.5-octave intense infrared pulses by nonlinear interactions in DAST crystal. *Journal of Optics*, 17(9):094005, 2015.

[210] Zhongyang Li, Pibin Bing, and Sheng Yuan. Terahertz generation by DSTMS based on cascaded difference frequency generation. *Optik*, 127(7):3552–3555, 2016.

[211] Andrea Rovere, Young-Gyun Jeong, Riccardo Piccoli, Seung-Heon Lee, Seung-Chul Lee, O-Pil Kwon, Mojca Jazbinsek, Roberto Morandotti, and Luca Razzari. Generation of high-field terahertz pulses in an HMQ-TMS organic crystal pumped by an ytterbium laser at 1030 nm. *Opt. Express*, 26(3):2509–2516, 2018.

[212] F. Meyer, N. Hekmat, T. Vogel, A. Omar, S. Mansourzadeh, F. Fobbe, M. Hoffmann, Y. Wang, and C. J. Saraceno. Milliwatt-class broadband THz source driven by a 112 W, sub-100 fs thin-disk laser. *Optics Express*, 27:30340, 2019.

[213] Carlo Vicario, Balazs Monoszlai, and Christoph P. Hauri. GV /m Single-Cycle Terahertz Fields from a Laser-Driven Large-Size Partitioned Organic Crystal. *Physical Review Letters*, 112(21):213901, 2014.

[214] K.L. Vodopyanov. Optical THz-wave generation with periodically-inverted GaAs. *Laser & Photonics Reviews*, 2(1-2):11–25, 2008.

[215] Samira Mansourzadeh, Tim Vogel, Mostafa Shalaby, Frank Wulf, and Clara J. Saraceno. Milliwatt average power, mHz-repetition rate, broadband THz generation in organic crystal BNA with diamond substrate. *Opt. Express*, 29(24):38946–38957, 2021.

[216] Peter H. Siegel. Terahertz technology. *IEEE Transactions on Microwave Theory and Techniques*, 50(3):910–928, 2002.

[217] Erich Bründermann, Heinz-Wilhelm Hübers, and Martin F. Kimmitt. *Terahertz Techniques*. Springer, 2012.

[218] B. Ferguson and X.-C. Zhang. Materials for terahertz science and technology. *Nature Materials*, 1:26–33, 2002.

[219] David M. Pozar. *Microwave Engineering*. Wiley, 4 edition, 2011.

[220] Antoni Rogalski and Fedor Sizov. Terahertz detectors and focal plane arrays. *Opto-Electronics Review*, 19(3):346–404, 2011.

[221] J. M. Chamberlain. Terahertz spectroscopy of solids. *Philosophical Transactions of the Royal Society A*, 362:199–213, 2004.

[222] Sidney B. Lang. *Sourcebook of Pyroelectricity*. Gordon and Breach, 1974.

[223] Roger W. Whatmore. Pyroelectric devices and materials. *Reports on Progress in Physics*, 49(12):1335–1386, 1986.

[224] A. M. Glass. Pyroelectricity and related properties of single crystals. *Journal of Applied Physics*, 40(12):4699–4713, 1969.

[225] R. H. McFee. Theory of the pyroelectric detector. *Journal of Applied Physics*, 31(6):1113–1120, 1960.

[226] D. Berlincourt and H. Jaffe. Pyroelectricity in polycrystalline ceramics. *Physical Review*, 135(6A):A1384–A1387, 1964.

[227] K. Hofmann and H. F. Schlaak. Pyroelectric infrared detectors: materials and applications. *Infrared Physics & Technology*, 36(3):707–718, 1995.

[228] G. F. Hawkins and R. W. Whatmore. Triglycine sulfate (TGS) and related materials for pyroelectric applications. *Ferroelectrics*, 44:15–28, 1982.

[229] M. J. Weber. Lithium tantalate and lithium niobate: materials for pyroelectric and electro-optic devices. *Journal of Applied Physics*, 68(2):487–503, 1990.

[230] T. Furukawa. Ferroelectric properties of vinylidene fluoride copolymers. *Phase Transitions*, 18:143–211, 1983.

[231] Zbigniew Bielecki, Janusz Mikolajczyk, and Jacek Wojtas. A review of thermal detectors of THz radiation operated at room temperature. *Sensors*, 24(21), 2024.

[232] Enrique Castro-Camus, Martin Koch, and Daniel M. Mittleman. Recent advances in terahertz imaging: 1999 to 2021. *Applied Physics B*, 128(1), 2022.

[233] B. B. Hu, J. T. Darrow, X.-C. Zhang, D. H. Auston, and P. R. Smith. Optically steerable photoconducting antennas. *Applied Physics Letters*, 56(10):886–888, 1990.

[234] J. Valdmanis and G. Mourou. Subpicosecond electrooptic sampling: Principles and applications. *IEEE Journal of Quantum Electronics*, 22(1):69–78, 1986.

[235] Q. Wu and X.-C. Zhang. Free-space electro-optic sampling of terahertz beams. *Applied Physics Letters*, 67(24):3523–3525, 1995.

[236] Paul C. M. Planken, Han-Kwang Nienhuys, Huib J. Bakker, and Tom Wenckebach. Measurement and calculation of the orientation dependence of terahertz pulse detection in ZnTe. *J. Opt. Soc. Am. B*, 18(3):313–317, 2001.

[237] Gargi Sharma, Kanwarpal Singh, Ibraheem Al-Naib, Roberto Morandotti, and Tsuneyuki Ozaki. Terahertz detection using spectral domain interferometry. *Opt. Lett.*, 37(20):4338–4340, 2012.

[238] Akram Ibrahim, Gargi Sharma, Kanwarpal Singh, and Tsuneyuki Ozaki. Terahertz Detection Based on Spectral-Domain Interferometry Using Mach-Zehnder Interferometer. *Journal of Infrared, Millimeter, and Terahertz Waves*, 37(9):837–845, 2016.

[239] Xing Zhu, David R. Bacon, Julien Madéo, and Keshav M. Dani. High field single- to few-cycle THz generation with lithium niobate. *Photonics*, 8(6), 2021.

[240] A.L. Chekhov, Y. Behovits, U. Martens, B.R. Serrano, M. Wolf, T.S. Seifert, M. Münzenberg, and T. Kampfrath. Broadband spintronic detection of the absolute field strength of terahertz electromagnetic pulses. *Phys. Rev. Appl.*, 20:034037, 2023.

[241] Sang-Hee Lee, Jae-Hee Lee, Chul Kang, and Ki-Yong Kim. Ionizing terahertz waves with 260 MV/cm from scalable optical rectification. *Light: Science & Applications*, 13(1):118, 2024.

[242] Matthias C. Hoffmann, János Hebling, Harold Y. Hwang, Ka-Lo Yeh, and Keith A. Nelson. Impact ionization in insb probed by terahertz pump—terahertz probe spectroscopy. *Phys. Rev. B*, 79:161201, 2009.

[243] Daichi Yoshioka, Fumiya Sekiguchi, Naotaka Yoshikawa, and Ryo Shimano. On-chip terahertz pump–probe spectroscopy revealing ultrafast current-induced breakdown dynamics in a superconducting nb microstrip. *Nano Letters*, 25(37):13764–13771, 2025.

[244] Tobias Kampfrath, Alexander Sell, Gregor Klatt, Alexej Pashkin, Sebastian Mährlein, Thomas Dekorsy, Martin Wolf, Manfred Fiebig, Alfred Leitenstorfer, and Rupert Huber. Coherent terahertz control of antiferromagnetic spin waves. *Nature Photonics*, 5:31–34, 2011.

[245] P. Gaal, K. Reimann, M. Woerner, T. Elsaesser, R. Hey, and K. H. Ploog. Nonlinear terahertz response of n-type GaAs. *Phys. Rev. Lett.*, 96:187402, 2006.

[246] Tobias Kampfrath, Koichiro Tanaka, and Keith Nelson. Resonant and nonresonant control over matter and light by intense terahertz transients. *Nature Photonics*, 7:680–690, 2013.

[247] Daniele Nicoletti and Andrea Cavalleri. Nonlinear light–matter interaction at terahertz frequencies. *Adv. Opt. Photon.*, 8(3):401–464, 2016.

[248] Chen Zhi-Wen, She Zhen-Yue, Liao Kai-Yu, Huang Wei, Yan Hui, and Zhu Shi-Liang. Terahertz measurement based on rydberg atomic antenna. *Acta Physica Sinica*, 70(6):060702–1–060702–11, 2021.

[249] Dinelka Somaweera, Amer Abdulghani, Ambali Alade Odebowale, Andergachew Mekonnen Berhe, Muthugalage I. U. Weerasinghe, Khalil As'ham, Ibrahim A. M. Al Ani, Morphy C. Dumlao, Andrey E. Miroshnichenko, and Haroldo T. Hattori. Rydberg atom-based sensors: Principles, recent advances, and applications. *Photonics*, 12(12), 2025.

[250] Hideki Hirori, Masaya Nagai, and Koichiro Tanaka. Excitonic interactions with intense terahertz pulses in ZnSe/ZnMgSSe multiple quantum wells. *Phys. Rev. B*, 81:081305, 2010.

[251] L. Razzari, F. H. Su, G. Sharma, F. Blanchard, A. Ayesheshim, H.-C. Bandulet, R. Morandotti, J.-C. Kieffer, T. Ozaki, M. Reid, and F. A. Hegmann. Nonlinear ultrafast modulation of the optical absorption of intense few-cycle terahertz pulses in n-doped semiconductors. *Phys. Rev. B*, 79:193204, 2009.

[252] János Hebling, Matthias C. Hoffmann, Harold Y. Hwang, Ka-Lo Yeh, and Keith A. Nelson. Observation of nonequilibrium carrier distribution in Ge, Si, and GaAs by terahertz pump–terahertz probe measurements. *Phys. Rev. B*, 81:035201, 2010.

[253] A. V. Ovchinnikov, O. V. Chefonov, M. B. Agranat, A. V. Kudryavtsev, E. D. Mishina, and A. A. Yurkevich. Free-carrier generation dynamics induced by ultrashort intense terahertz pulses in silicon. *Opt. Express*, 29(16):26093–26102, 2021.

[254] Simone Biasco, Florence Burri, Sarah Houver, Elsa Abreu, Matteo Savoini, and Steven L. Johnson. Impact ionization in low-band-gap semiconductors driven by ultrafast terahertz excitation: Beyond the ballistic regime. *Phys. Rev. B*, 106:235201, 2022.

[255] A. Dienst, M. C. Hoffmann, D. Fausti, J. C. Petersen, S. Pyon, T. Takayama, H. Takagi, and A. Cavalleri. Bi-directional ultrafast electric-field gating of interlayer charge transport in a cuprate superconductor. *Nature Photonics*, 5(8):485–488, 2011.

[256] Alessandra Milloch, Francesco Proietto, Naman Agarwal, Laura Foglia, Riccardo Mincigrucci, Genda Gu, Claudio Giannetti, Federico Cilento, Filippo Bencivenga, and Fulvio Parmigiani. Energy density driven ultrafast electronic excitations in a cuprate superconductor. *Phys. Rev. B*, 113:024507, 2026.

[257] Shinichi Watanabe, Nobutsugu Minami, and Ryo Shimano. Intense terahertz pulse induced exciton generation in carbon nanotubes. *Opt. Express*, 19(2):1528–1538, 2011.

[258] Blake S. Dastrup, Jacob R. Hall, and Jeremy A. Johnson. Experimental determination of the interatomic potential in linbo3 via ultrafast lattice control. *Applied Physics Letters*, 110(16):162901, 2017.

[259] Vladislav Bilyk, Nikita Ilyin, Elena Mishina, Andrey Ovchinnikov, Oleg Chefonov, and Vladimir Mukhortov. Nonlinear terahertz pulse induced polarization dynamics in ferroelectric ba0.8sr0.2tio3 thin film. *Scripta Materialia*, 214:114687, 2022.

[260] H. Handa, Y. Okamura, R. Yoshimi, A. Tsukazaki, K. S. Takahashi, Y. Tokura, and Y. Takahashi. Terahertz field driven giant nonlinear phonon response in ferroelectric semiconductor in-doped (sn,pb)te. *Phys. Rev. B*, 109:L081102, 2024.

[261] C L Korpa, Gy Tóth, and J Hebling. Interplay of diffraction and nonlinear effects in the propagation of ultrashort pulses. *Journal of Physics B: Atomic, Molecular and Optical Physics*, 49(3):035401, 2016.

[262] I. Katayama, H. Aoki, J. Takeda, H. Shimosato, M. Ashida, R. Kinjo, I. Kawayama, M. Tonouchi, M. Nagai, and K. Tanaka. Ferroelectric soft mode in a $\mathrm{srtio_3}$ thin film impulsively driven to the anharmonic regime using intense picosecond terahertz pulses. *Phys. Rev. Lett.*, 108:097401, 2012.

[263] Weiyi Hong, Peixiang Lu, Pengfei Lan, Qingbin Zhang, and Xinbing Wang. Few-cycle attosecond pulses with stabilized-carrier-envelope phase in the presence of a strong terahertz field. *Opt. Express*, 17(7):5139–5146, 2009.

[264] Emeric Balogh, Katalin Kovacs, Peter Dombi, Jozsef A. Fulop, Gyozo Farkas, Janos Hebling, Valer Tosa, and Katalin Varju. Single attosecond pulse from terahertz-assisted high-order harmonic generation. *Phys. Rev. A*, 84:023806, 2011.

[265] Katalin Kovács, Emeric Balogh, János Hebling, Valer Toşa, and Katalin Varjú. Quasi-phase-matching high-harmonic radiation using chirped THz pulses. *Phys. Rev. Lett.*, 108:193903, 2012.

[266] Emeric Balogh, József Fülöp, Janos Hebling, Péter Dombi, Gyozo Farkas, and Katalin Varjú. Application of high intensity THz pulses for gas high harmonic generation. *Central European Journal of Physics*, 11, 2013.

[267] B. V. Rumiantsev, E. A. Migal, A. V. Pushkin, and F. V. Potemkin. Observation of terahertz-field-induced coherent control of high-order harmonic generation in a noble gas. *Phys. Rev. A*, 111:023117, 2025.

[268] Peter Baum and Ahmed H. Zewail. Breaking resolution limits in ultrafast electron diffraction and microscopy. *Proceedings of the National Academy of Sciences*, 103(44):16105–16110, 2006.

[269] W. Ronny Huang, Shu-Wei Huang, Eduardo Granados, Koustuban Ravi, Kyung-Han Hong, Luis E. Zapata, and Franz X. Kärtner and. Highly efficient terahertz pulse generation by optical rectification in stoichiometric and cryo-cooled congruent lithium niobate. *Journal of Modern Optics*, 62(18):1486–1493, 2015.

[270] W. Ronny Huang, Arya Fallahi, Xiaojun Wu, Huseyin Cankaya, Anne-Laure Calendron, Koustuban Ravi, Dongfang Zhang, Emilio A. Nanni, Kyung-Han Hong, and Franz X. Kärtner. Terahertz-driven, all-optical electron gun. *Optica*, 3(11):1209–1212, 2016.

[271] P S Nugraha, G Krizsán, Gy Polónyi, M I Mechler, J Hebling, Gy Tóth, and J A Fülöp. Efficient semiconductor multicycle terahertz pulse source. *Journal of Physics B: Atomic, Molecular and Optical Physics*, 51(9):094007, 2018.

[272] Gupta Abhishek, Jutas Rokas, Gollner Claudia, Andrius Baltuš, Audrius Pugžlys, and Fulop Jozsef. Broadband gap contact-grating terahertz source pumped at 3.9 μm. *Optics Express*, 34(6), 2026. Accepted for publication.

[273] Jean Wei, Joel M. Murray, Jacob O. Barnes, Douglas M. Krein, Peter G. Schunemann, and Shekhar Guha. Temperature dependent sellmeier equation for the refractive index of GaP. *Opt. Mater. Express*, 8(2):485–490, 2018.

[274] Z. Ollmann, J. A. Fülöp, J. Hebling, and G. Almási. Design of a high-energy terahertz pulse source based on ZnTe contact grating. *Optics Communications*, 315:159–163, 2014.

[275] Gyula Polónyi, Mátyás I. Mechler, János Hebling, and József A. Fülöp. Prospects of semiconductor terahertz pulse sources. *IEEE Journal of Selected Topics in Quantum Electronics*, 23(4):8501508, 2017.

[276] Zoltán Tibai, Nelson M. Mbithi, Gábor Almási, József A. Fülöp, and János Hebling. Design of semiconductor contact grating terahertz source with enhanced diffraction efficiency. *Crystals*, 12(8), 2022.

[277] Anthony E. Siegman. *Lasers*, chapter 13: Laser Oscillation, pages 491–555. University Science Books, Mill Valley, CA, 1986.

[278] József András Fülöp and János Hebling. Applications of tilted-pulse-front excitation. In Ki Young Kim, editor, *Recent Optical and Photonic Technologies*, pages 207–230. InTech, Rijeka, 2010.

[279] Maria Göppert-Mayer. Über Elementarakte mit zwei Quantensprüngen. *Annalen der Physik*, 401(3):273–294, 1931.

[280] Jia-Ming Liu. *Multiphoton Absorption*. Cambridge University Press, 2022.

[281] Vaidya Nathan, A. H. Guenther, and S. S. Mitra. Review of multiphoton absorption in crystalline solids. *J. Opt. Soc. Am. B*, 2(2):294–316, 1985.

[282] T. Kawamori, P.G. Schunemann, V. Gruzdev, and K.L. Vodopyanov. High-order (n = 4–6) multiphoton absorption and mid-infrared kerr nonlinearity in GaP, ZnSe, GaSe, and ZGP crystals. *APL photonics*, 7(8):3563—-3568, 2022.

[283] Bob D. Guenther and Duncan G. Steel, editors. *Encyclopedia of Modern Optics*. Elsevier Science, second edition edition, 2018.

[284] L. V. Keldysh. Ionization in the field of a strong electromagnetic wave. *J. Exp. Theor. Phys.*, 20(5):1307–1314, 1965.

[285] Jeremy R. Gulley. Modeling free-carrier absorption and avalanching by ultrashort laser pulses. In Gregory J. Exarhos, Vitaly E. Gruzdev, Joseph A. Menapace, Detlev Ristau, and M. J. Soileau, editors, *Laser-Induced Damage in Optical Materials: 2011*, volume 8190, page 819022. International Society for Optics and Photonics, SPIE, 2011.

[286] Vitaly E. Gruzdev. Fundamental mechanisms of laser damage of dielectric crystals by ultrashort pulse: ionization dynamics for the Keldysh model. *Optical Engineering*, 53(12):122515, 2014.

[287] Ferris Chris. *Theoretical Modeling of Laser-Induced Absorption Phenomena in Optical Materials*. Phd, University of Nebraska, 2014.

[288] R. Hollinger, P. Malevich, V. Shumakova, S. Ališauskas, M. Zapf, R. Roder, A. Pugžlys, A. Baltuška, C. Ronning, C. Spielmann, and D. Kartashov. Strong light-field driven nanolasers. *Nano letters*, 19(6):3563–3568, 2019.

[289] MATLAB Help Center. ellipke - complete elliptic integrals of first and second kind. `www.mathworks.com/help/matlab/ref/ellipke.html`, 2025. Accessed: 2026-02-21.

[290] P. Yu and M. Cardona. *Fundamentals of Semiconductors: Physics and Materials Properties*. Graduate Texts in Physics. Springer Berlin Heidelberg, 2010.

[291] Mid-infrared (MIR) laser system, the eli user portal. `https://up.eli-laser.eu/laser/1723138152/`. Accessed: 2025-12-15.

[292] M.V. Fischetti and S.E. Laux. Monte carlo simulation of transport in technologically significant semiconductors of the diamond and zinc-blende structures. ii. submicrometer mosfet's. *IEEE Transactions on Electron Devices*, 38(3):650–660, 1991.

[293] Sergey B. Mirov, Igor S. Moskalev, Sergey Vasilyev, Viktor Smolski, Vladimir V. Fedorov, Dmitry Martyshkin, Jeremy Peppers, Mike Mirov, Alex Dergachev, and Valentin GaPontsev. Frontiers of mid-IR lasers based on transition metal doped chalcogenides. *IEEE Journal of Selected Topics in Quantum Electronics*, 24(5), 2018.

[294] Ekaterina Migal, Andrey Pushkin, Boris Bravy, Vyacheslav Gordienko, Nikita Minaev, Anatoly Sirotkin, and Fedor Potemkin. 3.5-mJ 150-fs Fe:ZnSe hybrid mid-IR femtosecond laser at 4.4 μm for driving extreme nonlinear optics. *Opt. Lett.*, 44(10):2550–2553, 2019.

[295] Vyacheslav E. Leshchenko, Bradford K. Talbert, Yu Hang Lai, Sha Li, Yaguo Tang, Stephen J. Hageman, Greg Smith, Pierre Agostini, Louis F. DiMauro, and Cosmin I. Blaga. High-power few-cycle Cr:ZnSe mid-infrared source for attosecond soft x-ray physics. *Optica*, 7(8):981–988, 2020.

[296] Anton Sinko, Ilya Ozheredov, Elena Rudneva, Vera Manomenova, Natalia Kozlova, Natalia Lobova, Alexey Voloshin, Jean-Louis Coutaz, and Alexander Shkurinov. Perspective on terahertz applications of molecular crystals. *Electronics*, 11:2731, 2022.

[297] J. Tauc. Optical properties and electronic structure of amorphous Ge and Si. *Materials Research Bulletin*, 3:37, 1968.

[298] Gang Wang, Si Xiao, Yuhui Peng, Yingwei Wang, Cailei Yuan, and Jun He. Two-photon and three-photon absorption in ZnO nanocrystals embedded in Al_2O_3 matrix influenced by defect states. *Optics Letters*, 44:179, 2019.

[299] Pedro H.M. Andrade, Christophe Volkringer, Thierry Loiseau, Antonio Tejeda, Matthieu Hureau, and Alain Moissette. Band GaP analysis in MOF materials: Distinguishing direct and indirect transitions using UV–Vis spectroscopy. *Applied Materials Today*, 37:102094, 2024.

[300] K. Srinivasan, R. Biravaganesh, R. Gandhimathi, and P. Ramasamy. Growth and characterization of NMBA (4-nitro-4'-methyl benzylidene aniline) single crystals. *Journal of Crystal Growth*, 236(1):381–392, 2002.

[301] Guang S He, Przemyslaw P Markowicz, Tzu-Chau Lin, and Paras N Prasad. Observation of stimulated emission by direct three-photon excitation. *Nature*, 415:767, 2002.

[302] Jun He, Yingli Qu, Heping Li, Jun Mi, and Wei Ji. Three-photon absorption in ZnO and ZnS crystals. *Optics Express*, 13:9235, 2005.

[303] Guang S. He, Loon-Seng Tan, Qingdong Zheng, and Paras N. Prasad. Multiphoton absorbing materials: Molecular designs, characterizations, and applications. *Chemical Reviews*, 108:1245, 2008.

[304] Yu O Yakovlev and V M Poezzhalov. Optical characteristics and prospects for the use of p-nitro-p'-methylbenzalaniline crystals in nonlinear optics. *Soviet Journal of Quantum Electronics*, 20(11):1431, 1990.

[305] Tomasz Seidler, Katarzyna Stadnicka, and Benoît Champagne. Investigation of the linear and second-order nonlinear optical properties of molecular crystals within the local field theory. *The Journal of Chemical Physics*, 139:114105, 2013.

[306] Mohammad Allaham, Rashid Dallaev, Daniel Burda, Dinara Sobola, Alois Nebojsa, Alexandr Knápek, Marwan S Mousa, and Vladimír Kolařík. Energy GaP measurements based on enhanced absorption coefficient calculation from transmittance and reflectance raw data. *Physica Scripta*, 99:025952, 2024.

[307] Isaac C. Tangen, Gabriel A. Valdivia-Berroeta, Larry K. Heki, Zachary B. Zaccardi, Erika W. Jackson, Charles B. Bahr, (Enoch) Sin-Hang Ho, David J. Michaelis, and Jeremy A. Johnson. Comprehensive characterization of terahertz generation with the organic crystal BNA. *Journal of the Optical Society of America B*, 38:2780, 2021.

[308] Lee W. Tutt and Thomas F. Boggess. A review of optical limiting mechanisms and devices using organics, fullerenes, semiconductors and other materials. *Progress in Quantum Electronics*, 17:299, 1993.

[309] Guang S. He, Jayant D. Bhawalkar, Chan F. Zhao, and Paras N. Prasad. Optical limiting effect in a two-photon absorption dye doped solid matrix. *Applied Physics Letters*, 67:2433, 1995.

[310] J.-F. Lami, P. Gilliot, and C. Hirlimann. Observation of interband two-photon absorption saturation in CdS. *Physical Review Letters*, 77:1632, 1996.

[311] R. Schroeder and B. Ullrich. Absorption and subsequent emission saturation of two-photon excited materials: theory and experiment. *Optics Letters*, 27:1285, 2002.

[312] B. Monoszlai, P. S. Nugraha, Gy. Tóth, Gy. Polónyi, L. Pálfalvi, L. Nasi, Z. Ollmann, E. J. Rohwer, G. Gäumann, J. Hebling, T. Feurer, and J. A. Fülöp. Measurement of four-photon absorption in GaP and ZnTe semiconductors. *Optics Express*, 28:12352, 2020.

[313] Sean M. Kirkpatrick, Rajesh R. Naik, and Morley O. Stone. Nonlinear saturation and determination of the two-photon absorption cross section of green fluorescent protein. *The Journal of Physical Chemistry B*, 105:2867, 2001.

[314] Guang S. He, Qingdong Zheng, Alexander Baev, and Paras N. Prasad. Saturation of multiphoton absorption upon strong and ultrafast infrared laser excitation. *Journal of Applied Physics*, 101:083108, 2007.

[315] Anthony E Siegman. *Lasers*. University Science Books, 1986.

[316] Liu Yu, Liu Hao, Meiqiong Tang, Huang Jiaoqi, Liu Wei, Dong Jinying, Chen Xueping, Fu Weiling, and Zhang Yang. The medical application of terahertz technology in non-invasive detection of cells and tissues: opportunities and challenges. *RSC Advances*, 9:9354–9363, 2019.

[317] Zhiyao Yan, Li-Guo Zhu, Kun Meng, Wanxia Huang, and Qiwu Shi. THz medical imaging: from in vitro to in vivo. *Trends in Biotechnology*, 40(7):816–830, 2022.

[318] Samira Mansourzadeh, Tim Vogel, Alan Omar, Tobias O. Buchmann, Edmund J. R. Kelleher, Peter U. Jepsen, and Clara J. Saraceno. Towards intense ultra-broadband high repetition rate terahertz sources based on organic crystals. *Opt. Mater. Express*, 13(11):3287–3308, 2023.

[319] F. Roeder, M. Shalaby, B. Beleites, F. Ronneberger, and A. Gopal. THz generation by optical rectification of intense near-infrared pulses in organic crystal BNA. *Opt. Express*, 28(24):36274–36285, 2020.